Parametrically Forced Rotating and/or Stratified Confined Flows

by

Ke Wu

A Dissertation Presented in Partial Fulfillment
of the Requirements for the Degree
Doctor of Philosophy

Approved April 2019 by the
Graduate Supervisory Committee:

Juan Lopez, Co-Chair
Bruno Welfert, Co-Chair
Rodrigo Platte
Wenbo Tang
Marcus Herrmann

ARIZONA STATE UNIVERSITY

May 2019

ABSTRACT

The dynamics of a fluid flow inside 2D square and 3D cubic cavities under various configurations were simulated and analyzed using a spectral code I developed.

This code was validated against known studies in the 3D lid-driven cavity. It was then used to explore the various dynamical behaviors close to the onset of instability of the steady-state flow, and explain in the process the mechanism underlying an intermittent bursting previously observed. A fairly complete bifurcation picture emerged, using a combination of computational tools such as selective frequency damping, edge-state tracking and subspace restriction.

The code was then used to investigate the flow in a 2D square cavity under stable temperature stratification, an idealized version of a lake with warmer water at the surface compared to the bottom. The governing equations are the Navier-Stokes equations under the Boussinesq approximation. Simulations were done over a wide range of parameters of the problem quantifying the driving velocity at the top (e.g. wind) and the strength of the stratification. Particular attention was paid to the mechanisms associated with the onset of instability of the base steady state, and the complex nontrivial dynamics occurring beyond onset, where the presence of multiple states leads to a rich spectrum of states, including homoclinic and heteroclinic chaos.

A third configuration investigates the flow dynamics of a fluid in a rapidly rotating cube subjected to small amplitude modulations. The responses were quantified by the global helicity and energy measures, and various peak responses associated to resonances with intrinsic eigenmodes of the cavity and/or internal retracing beams were clearly identified for the first time. A novel approach to compute the eigenmodes is also described, making accessible a whole catalog of these with various properties and dynamics. When the small amplitude modulation does not align with the rotation axis (precession) we show that a new set of eigenmodes are primarily excited as the

angular velocity increases, while triadic resonances may occur once the nonlinear regime kicks in.

DEDICATION

To my parents.

TABLE OF CONTENTS

Page

CHAPTER Page

CHAPTER Page

LIST OF TABLES

LIST OF FIGURES

Figure Page

Figure Page

Figure Page

Figure Page

Chapter 1

OVERVIEW

1.1 Introduction

Computational fluid dynamics simulations have been an important tool for scholars, researchers, and scientists to study the flow dynamics at different scales and in different configurations. The development of efficient and accurate numerical methods, along with the improvement of the computing capability of supercomputers, has enabled the investigation of many difficult or infeasible physical experiments via numerical simulations. For instance, measuring the entire velocity, constraining the unstable flows to certain subspaces and computing unstable solutions. These difficulties can be resolved using numerical simulations, which can provide a deeper and more complete understanding of flow dynamics.

This work deals with the identification and analysis phenomena observed in nature, such as internal waves and inertial waves, which are ubiquitous in the atmosphere, oceans and lakes, as well as in laboratory experiments. It is significant to understand the generation and propagation of these waves in order to determine the energy carried by them. This is carried out on model physical problems of flows in square and cubic cavities under various configurations, aiming to isolate particular processes. The governing equations are Navier-Stokes equations with no-slip boundary conditions for incompressible fluids, which are solved by a pseudospectral collocation method. The tools I have incorporated in order to tackle these problems include dynamical system theory (bifurcation theory), numerical methods (spectral methods), computer programming (Fortran, Python, Matlab), and theory of rotat-

ing and stratified fluids. The results are obtained by synergistic use of these four components.

This dissertation starts with building an accurate and efficient numerical solver. The three dimensional lid-driven cavity is a benchmark problem and used for testing the code, thanks to many numerical results available in the literature for this problem. In addition, the flow dynamics and multiple states were investigated by Feldman and Gelfgat [19], Kuhlmann and Albensoeder [37], Loiseau *et al.* [44], but none of them were able to explain the observed intermittent bursting phenomena. Based on the numerical method proposed by Hugues and Randriamampianina [27], I wrote a three dimensional pseudospectral code in Fortran for solving the Navier-Stokes equations. I also built code for computing unstable basic states using selective frequency damping technique as proposed by Jordi *et al.* [32] , as well as computing flows in a symmetric subspace. The fast and accurate spectral solver was built, the bursting phenomena was demonstrated and its occurrence explained in terms of bifurcation theory.

After building the numerical solver, I turned my attention to a broader range of topics, such as stratified flows and rotating flows. Stratified flows are very common, such as in the Earth's oceans and its atmosphere. The interesting phenomena in stratified flows is the energy transport from well-mixed unstable regions to stably stratified regions through internal wave propagation. Cohen *et al.* [15] conducted the three dimensional stratified lid-driven cavity experiment and claimed that the flow is not strongly three dimensional, which motivated me to use the two-dimensional stratified lid-driven cavity to study the flow dynamics, and allowed me to perform a study over a wide range of parameters (Reynolds number and Richardson number) simulations. Different types of bifurcations were classified and multiple flow states were identified. Moreover, the internal waves were also observed at high Richardson numbers. The study enlighted rich dynamics occurring in the flow due to competition

between the driving and buoyancy forces.

Another direction of this work is rotating fluids. Greenspan [24] did a comprehensive study of theories in rotating fluids. The prominent phenomena in rotating fluids is inertial waves, which unlike the surface gravity waves, exist in the interior of the fluid. The generation of inertial waves is due to the restoring nature of the Coriolis force. In the current literature, multiple geometries under rotation have been intensively studied via both numerical simulations and physical experiments, such as cylinders, spheres and ellipsoids. The dynamics inside a rotating cube had not been extensively studied.

Boisson *et al.* [10] did a physical experiment of a librating cube. A librating cube is a rapidly rotating cube, on which is imposed a small amplitude modulation. It is interesting to note that at a particular modulation frequency, even with a very small modulation amplitude, the response of the system can be very large in terms of a specific measurement, for instance, the global kinetic energy or the global helicity inside the cube. In a librating cube, theoretically, when the libration frequency is less than twice the background rotating frequency, the system supports inertial wave beams, and the angle formed by the inertial wave beams with respect to the rotating axis is governed by the dispersion relation. At a certain angle, these wave beams can form retracing rays, which are able to cause a large response. In another aspect, the intrinsic eigenmodes of the cube can be excited via resonance when the forcing frequency is close to the frequency of a particular eigenmode of the cube, which also causes a large response. Maas [58] computed eigenmodes and eigenfrequencies of the cube numerically, but certain symmetries of these modes could not be determined other than by plotting them, and numerically stability issues such as the Gibbs phenomenon emerged in their numerical solutions. Boisson *et al.* [10] did the librating cube experiment at relatively large Ekman number and modulation amplitudes, which

renders large nonlinear and viscous effects. In addition, the parameter range of the modulation frequencies they used was also quite narrow. These limitations might result in ill-formed retracing rays and excessive viscous damping of the eigenmodes. Finally, they concluded that only a subset of the eigenmodes could be excited, those whose symmetry was consistent with the symmetry of the forcing. The question still remains as how to excite other modes of the cube. Another way to force the cube is precession. Goepfert and Tilgner [22] performed a numerical simulation of a precessing cube and claimed that instability in the form of triadic resonance is observed. However, But in their simulations, slip boundary conditions were imposed, which are not physical; second, the specific eigenmodes of the cube which are involved in the triadic resonance were not identified. The question we added here is whether if the same dynamics would be obtained if the no slip boundary conditions were imposed. These unsolved questions from the three papers mentioned motivated me to compute the eigenmodes of the cube and to do simulations of the librating cube with smaller Ekman numbers and smaller modulation amplitudes, as well as simulations of the precessing cube with physical no-slip boundary conditions.

In order to better understand the physical mechanism of the librating cube, I did the simulations at four different Ekman numbers over a wide range of selected modulation frequencies over the whole range from 0 to 1, where inertial waves are observed. The responses were quantified by the global helicity and energy inside the cube excluding the boundaries. The response diagrams were investigated, and the eigenmodes of cube were also computed in certain symmetry subspaces. The vorticity fields were visualized on different vertical and horizontal cuts of the cube. It turns out that the physical mechanism of the peak responses are either due to retracing inertial wave beams or excitation of the intrinsic eigenmodes of the cube, or both. The inertial wave beams always exit over the chosen frequency range and

can interfere with the natural rotation of eigenmodes.

I also conducted the simulations of the precession cube. The precession angle was fixed at one degree, with four different background rotation rates selected. For each rotation rate, I did the simulation over a wide range of Poincaré numbers, from -1 to 1. The response was quantified by the total kinetic energy inside the cube. The response diagrams were also investigated, and multiple peaks appear in the response diagram. The vorticity fields were also visualized on different horizontal and vertical cuts of the cube. It turns out that another subset of the eigenmodes of the cube are excited by the precessional forcing, those is the complementary symmetry subspace to these forced by libration. Moreover, the quasi periodic flows were also obtained by the direct numerical simulations, and the instability seems due to the triadic resonance, and the specific eigenmodes that cause the resonance is still currently under investigation.

1.2 Dissertation Plan

This dissertation develops numerical solvers for two and three dimensional Navier-Stokes equations. The computer codes are used to study flow dynamics in two-dimensional square and three-dimensional cubic cavities under multiple configurations. The Navier-Stokes equations are solved via pseudospectral methods proposed by Hugues and Randriamampianina [27]. The numerical solver is applied to investigate flows in different configurations. In each configuration, either the forcing term or boundary conditions need to be modified.

Chapter 2 describes the numerical method used, including implementation details. Chapter 3 studies the three-dimensional lid-driven cavity problem, which was published in Lopez *et al.* [57]. Chapter 4 focuses on the two-dimensional stratified lid-driven cavity problem, where the driving force and buoyancy force compete and

lead to various flow states. The details of this work were published in Wu *et al.* [95]. Chapter 5 studies the flow inside a rapidly rotating cube subjected to small amplitude modulations. This work was published in Wu *et al.* [94]. Conclusions and future work are presented in chapter 6.

Chapter 2

NUMERICAL METHOD

2.1 Governing Equations in General

The geometry considered in this body of work is either a square or a cubic cavity under various configurations associated to different boundary conditions and forcing terms. The equations governing the flow are the Navier-Stokes (NS) equations. In the non-isothermal stratified case, the NS equations are modified according to the Boussinesq approximation and complemented with a temperature evolution equation (NSB). The NSB equations:

$$\begin{aligned} \frac{\partial \boldsymbol{u}}{\partial t} + \boldsymbol{u} \cdot \nabla \boldsymbol{u} &= -\nabla p + \nabla^2 \boldsymbol{u} + \boldsymbol{F} \quad \text{in } \boldsymbol{\Omega}, \\ \frac{\partial T}{\partial t} + \boldsymbol{u} \cdot \nabla T &= \frac{1}{Pr} \nabla^2 T \qquad \text{in } \boldsymbol{\Omega}, \\ \nabla \cdot \boldsymbol{u} &= 0 \qquad \text{in } \boldsymbol{\Omega}. \end{aligned} \tag{2.1}$$

The boundary and initial conditions are:

$$\boldsymbol{u} = \boldsymbol{u}_b, \quad T = T_b \quad \text{on } \boldsymbol{\partial\Omega}, \tag{2.2}$$

$$\boldsymbol{u} = \boldsymbol{u}_0, \quad T = T_0 \quad \text{at } t = 0. \tag{2.3}$$

The vector $\boldsymbol{u}$ represents the velocity field, p is the static pressure, T represents the temperature field, and Pr represent the Prandtl number. $\boldsymbol{F}$ represents the forcing term, which depends on the specific configuration, and depends on T in the stratified case. $\boldsymbol{\Omega}$ represents the interior of the computational domain, $\boldsymbol{\partial\Omega}$ represents its boundary. For isothermal flows, the temperature equation can be ignored.

2.2 Spatial Discretization

The velocity, pressure, and temperature variables are approximated by Chebyshev polynomials of the first kind with degree less than or equal to M, N and R in the x, y, z directions respectively :

$$\boldsymbol{u} = \sum_{r=0}^{R}\sum_{n=0}^{N}\sum_{m=0}^{M} \hat{\boldsymbol{u}}_{mnr} f_m(x) f_n(y) f_r(z), \tag{2.4}$$

$$T = \sum_{r=0}^{R}\sum_{n=0}^{N}\sum_{m=0}^{M} \hat{T}_{mnr} f_m(x) f_n(y) f_r(z), \tag{2.5}$$

$$p = \sum_{r=0}^{R}\sum_{n=0}^{N}\sum_{m=0}^{M} \hat{p}_{mnr} f_m(x) f_n(y) f_r(z), \tag{2.6}$$

where $f_m(x), f_n(y), f_r(z)$ are Chebyshev polynomials with degree less or equal to M, N and R respectively. The associated Chebyshev-Gauss-Lobatto collocation grids are defined as:

$$x_i = \cos(i\pi/N) \quad i \in \{0, 1, 2, ..., M\} \tag{2.7}$$

$$y_j = \cos(j\pi/N) \quad j \in \{0, 1, 2, ..., N\} \tag{2.8}$$

$$z_k = \cos(k\pi/N) \quad k \in \{0, 1, 2, ..., R\} \tag{2.9}$$

2.3 Time Integration

The numerical scheme for solving the NS equations used here initially was introduced by Hugues and Randriamampianina [27]. Mercader *et al.* [67] adapted the method to include temperature dependence. Let $NL(\boldsymbol{u})$ and $NL(\boldsymbol{u}, T)$ represent the nonlinear terms, in the governing equations (2.1). The time integration scheme for both velocity and temperature equations is a second-order accurate scheme based on a combination of Adams-Bashforth and backward differentiation formulae (AB/BDF2):

$$\frac{3\boldsymbol{u}^{n+1} - 4\boldsymbol{u}^{n} + \boldsymbol{u}^{n-1}}{2\delta t} + 2NL(\boldsymbol{u}^{n}) - NL(\boldsymbol{u}^{n-1}) = -\nabla p^{n+1} + \nabla^2 \boldsymbol{u}^{n+1} + \boldsymbol{F}^{n+1}. \tag{2.10}$$

$$\frac{3T^{n+1}-4T^n+T^{n-1}}{2\delta t}+2NL(\boldsymbol{u}^n,T^n)-NL(\boldsymbol{u}^{n-1},T^{n-1})=\frac{1}{Pr}\nabla^2T^{n+1}. \quad (2.11)$$

The explicit time evolution is described in more detail by the following steps:

- Step 1: compute the temperature T^{n+1} from the temperature equation

$$(\nabla^2-\frac{3Pr}{2\delta t})T^{n+1}=Pr\{2NL(\boldsymbol{u}^n,T^n)-NL(\boldsymbol{u}^{n-1},T^{n-1})-\frac{4T^n-T^{n-1}}{2\delta t}\}, \quad (2.12)$$

  with given boundary conditions. In this dissertation, the boundary conditions of temperature are either constant(dirichlet) or no heat flux (homogeneous Neumann).

- Step 2: compute the predictor pressure p^*

$$\nabla^2p^*=\nabla\cdot\{-2NL(\boldsymbol{u}^n)+NL(\boldsymbol{u}^{n-1})+\boldsymbol{F}^{n+1}\}, \quad (2.13)$$

  the boundary conditions for p^* are derived directly from equation (2.10) by taking the normal derivative of the pressure on the boundaries:

$$\frac{\partial p^*}{\partial \boldsymbol{n}}=\boldsymbol{n}\cdot\{\frac{-3\boldsymbol{u}_b^{n+1}+4\boldsymbol{u}^n-\boldsymbol{u}^{n-1}}{2\delta t}-2NL(\boldsymbol{u}^n)+NL(\boldsymbol{u}^{n-1})+ (2L(\boldsymbol{u}^n)-L(\boldsymbol{u}^{n-1})+\boldsymbol{F}^{n+1}\}, \quad (2.14)$$

  where $L(\boldsymbol{u})=-\nabla\times(\nabla\times\boldsymbol{u})$ represents the viscous term, written in solenoidal form in order to improve the stability, as suggested by Karniadakis [33].

- Step 3: compute the predictor velocity field $\boldsymbol{u}^*$ from the momentum equation

$$\frac{3\boldsymbol{u}^*-4\boldsymbol{u}^n+\boldsymbol{u}^{n-1}}{2\delta t}+2NL(\boldsymbol{u}^n)-NL(\boldsymbol{u}^{n-1})=-\nabla p^*+\nabla^2\boldsymbol{u}^*+\boldsymbol{F}^{n+1} \quad (2.15)$$

  with given boundary conditions. At this step, the exact boundary value $\boldsymbol{u}_b$ is imposed for the predictor velocity field $\boldsymbol{u}^*$.

- Step 4: evaluate the intermediate variable ϕ. The equation for ϕ is derived from the difference between equation (2.10) and equation (2.15)

$$\frac{3\boldsymbol{u}^{n+1} - 3\boldsymbol{u}^*}{2\delta t} = -\nabla(p^{n+1} - p^*), \tag{2.16}$$

enforcing the incompressible condition $\nabla \cdot \boldsymbol{u} = 0$ and defining the intermediate variable $\phi = \frac{2\delta t}{3}(p^{n+1} - p^*)$, equation (2.16) can be further recast as:

$$\nabla^2 \phi = \nabla \cdot \boldsymbol{u}^*, \tag{2.17}$$

with homogeneous Neumann boundary conditions derived from

$$\nabla \phi = \boldsymbol{u}^{n+1} - \boldsymbol{u}^*. \tag{2.18}$$

- Step 5: finally correct the pressure and velocity fields on the entire domain $\boldsymbol{\Omega} \cup \boldsymbol{\partial\Omega}$,

$$\begin{aligned} p^{n+1} &= p^* + \frac{3}{2\delta t}\phi, \\ \boldsymbol{u}^{n+1} &= \boldsymbol{u}^* - \nabla\phi, \end{aligned} \tag{2.19}$$

because this step corrects the velocity field on the entire domain, so the boundary conditions for velocity field at $\boldsymbol{u}^{n+1}$ is slightly off.

At each step, the governing equation can be reduced to a Helmholtz equation of the form:

$$AX + BX + CX + \sigma X = H, \tag{2.20}$$

where A, B, C are matrices, σ is a constant, and H represents the forcing terms. This equation can be solved efficiently via matrix-diagonalization technique by Peyret [74]. Appendix B provides a detailed derivation of how to incorporate boundary conditions to formulate the linear system for governing equations in Chapter 5.

2.4 Coding Implementation

The computer code is written in Fortran 90. The entire code consists of two main parts: preprocessing steps and time iteration steps.

2.4.1 Generating the Differentiation Matrices

All the variables are evaluated directly on the Chebyshev collocation grids, so most of the computations are done via matrix multiplications. The Chebyshev differentiation matrix needs to be computed in the preprocessing steps. The formula for Chebyshev differentiation matrix is available in many textbooks, using the zero-sum trick and enforcing skew central symmetry.The second order Chebyshev differentiation matrix can be obtained by single squaring the first order Chebyshev differentiation matrix.

2.4.2 Helmholtz Solver

At each step of a single time iteration, an Helmholtz equation needs to be solved. Peyret [74, pp.88-98] explicitly explains how to use matrix-diagonalization technique to solve two-dimensional and three-dimensional Helmholtz equations. In the code, the implementation differs slightly, with improved stability properties. Here I present the implementation for the two-dimensional Helmholtz solver, and the implementation for three-dimensional Helmholtz solver follow a similar fashion. The two dimensional Helmholtz equation is:

$$AX + XB + \sigma X = H, \tag{2.21}$$

diagonalize the coefficient matrices A, B as :

$$A = P\Lambda_A P^{-1}, \qquad B = Q\Lambda_B Q^{-1}, \tag{2.22}$$

plug equation (2.22) into equation (2.21), which becomes

$$P\Lambda_A P^{-1}X + XQ\Lambda_B Q^{-1} + \sigma X = H. \tag{2.23}$$

The above equation can be further simplified by the following steps:

$$\begin{aligned}
\Lambda_A P^{-1}X + P^{-1}XQ\Lambda_B Q^{-1} + \sigma P^{-1}X = P^{-1}H, &\quad \text{multiply } P^{-1},\\
\Lambda_A \hat{X} + \hat{X}Q\Lambda_B Q^{-1} + \sigma \hat{X} = P^{-1}H, &\quad \text{let } \hat{X} = P^{-1}X,\\
\Lambda_A \hat{X}Q + \hat{X}Q\Lambda_B + \sigma \hat{X}Q = P^{-1}HQ, &\quad \text{multiply } Q,\\
\Lambda_A \bar{X} + \bar{X}\Lambda_B + \sigma \bar{X} = P^{-1}HQ, &\quad \text{let } \bar{X} = \hat{X}Q.
\end{aligned} \tag{2.24}$$

When the above equations implement into code, the matrices $P, Q, \Lambda_A, \Lambda_B$ are computed first using the intel *mkl* library subroutine *deggv*. Subsequently, X is obtained by following the steps in (2.24) in reverse order. In the code P^{-1}, Q^{-1} are not computed explicitly, which are suggested by Hugues and Randriamampianina [27] and Peyret [74]. Instead, an LU factorization of P, Q with pivoting is used to replace the matrix multiplications with P^{-1}, Q^{-1} by triangular solver using *mkl* subroutine *dgetrf*. After $P^{-1}H$ is computed, a double loop can be coded to compute $\bar{X}$, but due to the eigenvalues and σ do not change for each time iteration, therefore, the reciprocal of $(\Lambda_A + \Lambda_B + \sigma)$ can be pre-computed and saved as a matrix in the pre-processing steps. $\bar{X}$ can be computed directly by the saved reciprocal matrix and the right hand side matrix via the subroutine *degmm*.

2.4.3 Code Structure

At each time iteration, there are five steps. Also, nonlinear terms appear in (2.13) and (2.15), so a subroutine was built to compute the nonlinear terms at the beginning of each time iteration. In addition, a subroutine was built for each step during a single time iteration.

```
!-compute Chebyshev differentiation matrix
subroutine compute_Cheby_diff_matrix
!-compute eigenvalues and eigenvectors
subroutine compute_eigens
!-compute LU factorization of eigenvectors
subroutine compute_LU
!-build up Helmholtz solver
subroutine Helmholtz_solver
!-compute nonlinear terms
subroutine compute_nonlinear_terms
subroutine compute_temperature
subroutine compute_predictor_pressure
subroutine compute_predictor_velocity
subroutine correct_pressure_velocity
!-preprocessing steps
call compute_Cheby_diff_matrix
call compute_eigens
call compute_LU
! time iteration steps
do j = 1, num_steps
  call compute_nonlinear_terms
  call compute_temperatue
  call compute_predictor_pressure
  call compute_predictor_velocity
  call correct_pressure_velocity
end do
```

Chapter 3

TRANSITION TO COMPLEX DYNAMICS IN THE CUBIC LID-DRIVEN CAVITY

3.1 Abstract

The onset of time dependence in the cubic lid-driven cavity is surprisingly complicated, given the simplicity of the geometry and the modest value of the Reynolds number at which it occurs. The onset is characterized by finite amplitude oscillations which appear to be stable for long times, but are subjected to intermittent bursts at irregular times during which the reflection symmetry about the spanwise midplane is broken. The complex dynamics are shown to be intimately related to the subcritical nature of the instability of the steady basic state. We use a spectral collocation numerical technique, solving both in the full three-dimensional space as well as in the symmetric subspace, and use selective frequency damping and Arnoldi iterations about the unstable basic state to determine its bifurcations. Edge tracking is also used to investigate a number of time-dependent saddle states. Putting all this together, we show that the complex dynamics are organized by two successive Hopf bifurcations, the first of which is shown to be subcritical. All local states are unstable in the full space at higher Reynolds numbers, leading to the intermittent bursting behavior.

3.2 Introduction

The lid-driven cavity flow, consisting of the flow in a rectangular cavity driven by the steady translation of one of the cavity walls, is a canonical flow for the study of

the stability of separated shear layers. The idealized situation where the cavity is of infinite spanwise extent and the flow is assumed to be invariant in the spanwise direction has been studied extensively; see the review article by Shankar and Deshpande [81]. In the cubic cavity, the spanwise confinement effects are pronounced, and for Reynolds numbers $Re \sim 10^3$, the flow is steady with a single pair of streamwise vortices centered about the spanwise midplane, together with vortical structures along the edges where the spanwise walls meet the other walls. When the Reynolds number is increased beyond approximately 1910, the flow becomes unsteady, manifesting long periods of essentially periodic flow with intermittent bursts, and for slightly larger Re, the flow is persistently chaotic. A number of numerical investigations have contributed to the details of the flow dynamics in this regime where the flow in the cubic lid-driven cavity becomes unsteady. In the earliest such study, Feldman and Gelfgat [19] report that the steady flow loses stability at a subcritical Hopf bifurcation, with unsteady flow appearing for $Re \gtrsim 1914$. The more recent studies of Kuhlmann and Albensoeder [37], Loiseau [43], and Loiseau *et al.* [44] reproduce some aspects of the flows reported by Feldman and Gelfgat [19], but note that the periodic state of Feldman and Gelfgat [19] is not stable beyond the Hopf bifurcation, and that it undergoes sudden bursts at random times. They conclude that the simulations of Feldman and Gelfgat [19] were not run long enough for the intermittent bursts to manifest; near onset, it takes several viscous times for this to happen. Also, near onset the intervals between bursts can be very long (several viscous times). Following a burst, another essentially periodic state with larger amplitude and smaller frequency that persists for a relatively short time is observed before another burst occurs. The dynamics involved remain unclear; Loiseau [43] suggests that it is some type of intermittency that requires further investigation to unravel, Kuhlmann and Albensoeder [37] calls for further investigations to clarify the situation, and Loiseau *et al.* [44] concludes that

the origin of the intermittent events is still unknown. The numerical studies each use very different methods with a wide range of spatial and temporal resolutions; Feldman and Gelfgat [19] uses finite differences, Kuhlmann and Albensoeder [37] uses Chebyshev spectral collocation, and Loiseau [43], Loiseau *et al.* [44] use spectral elements. The results from the spectral collocation and the spectral elements methods, which were run for sufficiently long times, are in agreement. There are minor variations in the precise value of Re at which things happen, but this is readily accounted for by differences in resolution and the treatment of the discontinuous boundary condition at the edges where the moving lid meets the stationary walls. Thus, the transition from steady flow to intermittent bursting when Re is increased beyond a critical value is consistently observed by the various computations. The only experiment specifically designed to address this onset of unsteady flow in the lid-driven cube Liberzon *et al.* [42] is broadly consistent with the numerical results, but the resolution in Re available in the experiment was insufficient to resolve the details. Linear stability analysis of the types so far employed have been incapable of capturing the nature of the onset of the intermittent bursting reported from nonlinear simulations in the cubic cavity. In part, the problem is that linear stability analysis only gives the eigenstructure near instability, and for the cubic lid-driven cavity, the studies all agree that instability is via a subcritical Hopf bifurcation. Since the bifurcation is subcritical, the subsequent flow evolution is not well described by the bifurcating eigenmode. The previous nonlinear studies of the cubic cavity flow all report that the reflection symmetry about the spanwise midplane is broken to some degree in the unsteady nonlinear states, but they do not provide details about the nature of this symmetry breaking nor how it is related to the onset of unsteadiness.

Here, we use a Chebyshev spectral collocation method, similar in many ways to that used in Kuhlmann and Albensoeder [37] but with a different treatment of

the boundary condition discontinuity, and our nonlinear results are in very close agreement with Kuhlmann and Albensoeder [37], Loiseau [43], Loiseau *et al.* [44]. By computing in both the full three-dimensional space as well as in the reflection-symmetric subspace, we are able to show that the second periodic oscillations that are observed briefly following the bursts in fact correspond to a limit cycle that is unstable to symmetry breaking, and exists for much lower Re than that at which the basic state first loses stability. As was done in Loiseau [43], Loiseau *et al.* [44] we also compute the unstable basic state via selective frequency damping (SFD) Åkervik *et al.* [3] and then use Arnoldi iterations Saad [78] to study its linear stability. In agreement with Loiseau [43], Loiseau *et al.* [44], the limit cycle reported by Feldman and Gelfgat [19] corresponds to the first pair of complex-conjugate eigenvalues to acquire positive real part as Re is increased. As noted by Feldman and Gelfgat [19], Kuhlmann and Albensoeder [37], this Hopf bifurcation is subcritical, and we re-confirm this by computing the lower branch down to the cyclic-fold bifurcation at lower $Re \approx 1872$ using an edge state technique (EST) Itano and Toh [28], Schneider *et al.* [80]. We have also located a second Hopf bifurcation at $Re \approx 2089$ whose eigenfrequency is very close to that of the intermittent large-amplitude oscillations that are observed following a burst in the nonlinear simulations. This was also noted by Loiseau [43], Loiseau *et al.* [44], but they did not study the linear stability of the basic state beyond $Re = 2000$, and so missed this second bifurcation. By monitoring the symmetry of the nonlinear solutions, it is clear that the large-amplitude oscillations immediately following a burst are unstable to symmetry breaking. So, we have also computed the nonlinear solutions in the symmetry subspace and indeed find that these large-amplitude oscillations correspond to a limit cycle solution. We have continued this limit cycle down to much lower $Re \approx 1872$ where it undergoes a cyclic-fold bifurcation. Then, using EST in the symmetric subspace with combinations of the limit cycle and

the basic state as initial conditions, we have been able to capture the details of the lower-branch saddle limit cycle for a small range in Re. The lower-branch limit cycle undergoes a Neimark–Sacker bifurcation and acquires two unstable directions, thus compromising the effectiveness of EST to track it. However, at the Neimark–Sacker bifurcation, a quasiperiodic state is spawned, that has one unstable direction in the symmetry subspace. We have tracked this state using EST to slightly higher Re where it is absorbed in a subcritical Neimark–Sacker bifurcation of the upper branch of the other (low-amplitude) limit cycle, rendering that limit cycle unstable. By taking the various edge states computed in the symmetry subspace as initial conditions for nonlinear simulations in the full space, we have also been able to extract crucial information about which states are unstable to symmetry breaking. By piecing all this information together, we are able to provide a fairly complete and consistent picture of what is responsible for the bursting behavior.

3.3 Governing Equations and Numerical Techniques

Consider the flow in a cube of sides of length L, completely filled with an incompressible fluid of kinematic viscosity ν, driven by the motion of one wall at constant velocity U. Using L as the length scale and L/U as the time scale, the non-dimensional governing equations are

$$\partial \boldsymbol{u}/\partial t + \boldsymbol{u}\cdot\boldsymbol{\nabla}\boldsymbol{u} = -\boldsymbol{\nabla}p + Re^{-1}\,\nabla^2\boldsymbol{u}, \quad \boldsymbol{\nabla}\cdot\boldsymbol{u} = 0, \tag{3.1}$$

where the Reynolds number

$$Re = UL/\nu, \tag{3.2}$$

is a ratio of two time scales: the viscous time scale L^2/ν and the convective time scale L/U. For the most part, we will present results using the convective time scale, but the time series of flow quantities will be shown in terms of the viscous time scale. As

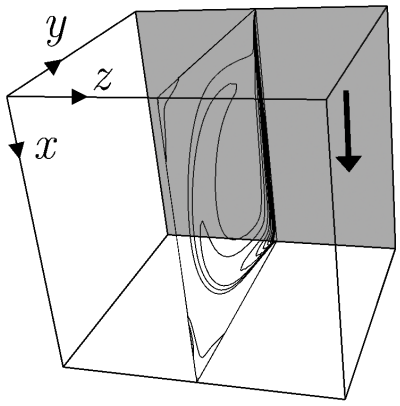

Figure 3.1: Schematic of the cubic lid-driven cavity. The perspective shown, with the back wall (at $y = 0.5$, shaded gray) moving downwards ($+x$-direction), is that used in all subsequent three-dimensional renderings of the results. In the spanwise midplane (at $z = 0$), typical streamlines of a low-Re steady-state flow are shown.

such, we introduce $\tau = t/Re$, where one time unit in τ is a viscous time.

The Cartesian coordinate system, $\boldsymbol{x} = (x, y, z)$, with the origin at the center of the cube is used; x is the direction in which the wall at $y = 0.5$ is moving, z is the spanwise direction, and the velocity field is $\boldsymbol{u} = (u, v, w)$. See Fig. 5.1 for a schematic.

The boundary conditions on the stationary walls at $x = \pm 0.5$, $y = -0.5$, and $z = \pm 0.5$ are no-slip, i.e. $\boldsymbol{u} = \boldsymbol{0}$ on these walls. Nominally, on the moving wall $(u, v, w) = (1, 0, 0)$, resulting in a jump discontinuity along the four edges, $(x, y, z) = (\pm 0.5, 0.5, z)$ and $(x, 0.5, \pm 0.5)$, where the moving wall meets the streamwise and spanwise walls.

The system (6.5), together with the boundary conditions, is equivariant with respect to a reflection symmetry $\mathcal{K}$ about the spanwise midplane $z = 0$. The action of this Z_2 symmetry on the velocity, vorticity $\nabla \times \boldsymbol{u} = (\xi, \eta, \zeta)$, and helicity $H =$

$\boldsymbol{u} \cdot (\nabla \times \boldsymbol{u})$ is

$$\mathcal{A}(\mathcal{K})(u, v, w)(x, y, z) = (u, v, -w)(x, y, -z), \tag{3.3a}$$

$$\mathcal{A}(\mathcal{K})(\xi, \eta, \zeta)(x, y, z) = (-\xi, -\eta, \zeta)(x, y, -z), \tag{3.3b}$$

$$\mathcal{A}(\mathcal{K})H(x, y, z) = -H(x, y, -z). \tag{3.3c}$$

The flow in the cubic lid-driven cavity is inherently three dimensional for all $Re \neq 0$. It is interesting to visualize the flow in terms of the helicity, which for the idealized spanwise invariant case is identically zero since the velocity and vorticity vectors are orthogonal.

A convenient global measure of the flow is the kinetic energy

$$E = \frac{1}{2} \int_{\mathcal{C}} |\boldsymbol{u}|^2 \, d\boldsymbol{x} \,, \tag{3.4}$$

where $\mathcal{C}$ is $\boldsymbol{x} \in [-0.5, 0.5] \times [-0.5, 0.5] \times [-0.5, 0.5]$. It is also convenient to introduce a symmetry parameter in order to measure the relative departure from symmetry of a solution:

$$S = \frac{1}{2E} \int_{\mathcal{C}} |\boldsymbol{u} - \mathcal{A}(\mathcal{K})\boldsymbol{u}|^2 \, d\boldsymbol{x} \,. \tag{3.5}$$

This symmetry parameter is proportional to the kinetic energy in the skew-symmetric component of the flow relative to the total kinetic energy of the flow.

3.3.1 Numerics

The Navier–Stokes system (6.5) is discretized using a spectral-collocation method in all spatial directions. Both velocity and pressure are approximated by polynomials of degree N $(\mathcal{P}_N, \mathcal{P}_N)$, written in barycentric form with weights $w_0 = 0.5$, $w_n = (-1)^n$ for $n \in [1, N-1]$, and $w_N = 0.5(-1)^N$, associated to the Chebyshev–Gauss–Lobatto grid. Spatial differentiation is performed via direct matrix-vector multiplication by the pseudospectral differentiation matrix (common to all three directions).

The time integration scheme used is the fractional-step improved projection method of Hugues and Randriamampianina [27], based on a linearly implicit and stiffly stable, second-order accurate scheme combining a backward differentiation formula for the linear terms and an explicit mix, equivalent to linear extrapolation, of Adams–Moulton and Adams–Bashforth steps for the nonlinear convective terms Vanel *et al.* [88]. The predictor stage of the fractional step method solves a Helmholtz equation for a pressure field, for which Neumann conditions consistent with (6.5) are applied at the walls. The corrector stage then projects the resulting predicted velocity field onto the space of (discretely) divergence-free polynomials via a Stokes problem, which is also handled by solving a Helmholtz equation for the corrected pressure, albeit with homogeneous Neumann boundary conditions. Further details can be found in Hugues and Randriamampianina [27].

The boundary condition for the streamwise component of velocity for the moving wall, $u = 1$, is discontinuous where it meets the four stationary walls. Discontinuous boundary conditions can lead to numerical problems when using spectral methods, and so we regularized it by using

$$u(x, 0.5, z) = \left[1 - 2\exp\left(\frac{-1}{\epsilon}\right)\cosh\left(\frac{2x}{\epsilon}\right)\right] \times \left[1 - 2\exp\left(\frac{-1}{\epsilon}\right)\cosh\left(\frac{2z}{\epsilon}\right)\right]. \tag{3.6}$$

The small positive number ϵ controls the distance over which the discontinuity is smoothed. This is a standard technique used in spectral methods Lopez and Shen [50]. As ϵ is decreased for a given Re, the accuracy of the spectral method becomes dominated by the need to resolve the steep variation in (3.6) rather than the flow. For the results presented here, with $Re \leq 2100$, we have used $\epsilon = 0.01$, for which $N = 48$ is sufficient to resolve (3.6), having 5 collocation points in the gap. When using local methods, such as finite differences and finite volume techniques, the gap is

the grid spacing at the edge, so that the gap decreases as the resolution is increased. An alternative treatment for global spectral methods is to try to account for the discontinuity asymptotically Boyd [11]. Kuhlmann and Albensoeder [37] implement such an approach, but were unable to account for the discontinuity at the four corners where the edges meet, $(x, y, z) = (\pm 0.5, 0.5, \pm 0.5)$. They noted that their spectral accuracy was considerably reduced as a consequence. The size of the gap has a direct impact on, for example, the critical Re for the onset of instability; a smaller gap results in a smaller critical $\mathrm{Re}_{\mathrm{H1}}$. In their finite volume study, Feldman and Gelfgat [19] found by direct simulation that for their highest resolution (and hence their smallest gap), the basic state loses stability via a subcritical Hopf bifurcation H_1 at $Re = \mathrm{Re}_{\mathrm{H1}} \approx 1927$. This compares very well with $\mathrm{Re}_{\mathrm{H1}} \approx 1929$ that we find using $\epsilon = 0.01$ and $N = 48$. They then used Richardson extrapolation to estimate $\mathrm{Re}_{\mathrm{H1}} = 1914$. Kuhlmann and Albensoeder [37] report $\mathrm{Re}_{\mathrm{H1}} \approx 1920$ using $N = 72$, although their $N = 48$ result is very close (≈ 1918). With all of this under consideration, our choice of ϵ represents a 1% gap along the edges and about a 0.5% increase in $\mathrm{Re}_{\mathrm{H1}}$ over what it would be with a zero gap. This allows us to have good spectral resolution with a relatively modest $N = 48$. In the following sections, we demonstrate excellent agreement with the previous numerical studies of the cubic lid-driven cavity. Small quantitative differences correspond to small shifts in the given Re due to the gap size differences. Most importantly, the details of the intermittent bursts for $Re > \mathrm{Re}_{\mathrm{H1}}$ that we find are in agreement with those reported in Kuhlmann and Albensoeder [37], Loiseau [43], Loiseau *et al.* [44].

For $Re < \mathrm{Re}_{\mathrm{H1}} \approx 1929$ the stable basic state BS can be determined via direct numerical simulation (DNS). At $Re = \mathrm{Re}_{\mathrm{H1}}$, BS loses stability via a (subcritical) Hopf bifurcation and cannot be computed via DNS. However, it can be computed by introducing a feedback control $\boldsymbol{v}$ into (6.5) and using the selective frequency damping

(SFD) technique described in Åkervik *et al.* [3]. Specifically, we solve the augmented system

$$\partial \boldsymbol{u}/\partial t + \boldsymbol{u}\cdot\boldsymbol{\nabla}\boldsymbol{u} = -\boldsymbol{\nabla}p + Re^{-1}\nabla^2\boldsymbol{u} + \omega_c(\boldsymbol{v}-\boldsymbol{u}), \tag{3.7a}$$

$$\partial \boldsymbol{v}/\partial t = \omega_c(\boldsymbol{u}-\boldsymbol{v}), \quad \boldsymbol{\nabla}\cdot\boldsymbol{u} = 0, \quad \boldsymbol{\nabla}\cdot\boldsymbol{v} = 0, \tag{3.7b}$$

with $\boldsymbol{v} = \boldsymbol{u}$ on all boundaries. Equation (3.7b) represents a low-pass filter applied to $\boldsymbol{u}$, with cut-off frequency ω_c. The selection $\omega_c = \omega/2$ optimizes damping of unstable modes of (3.7) oscillating at a target frequency ω close to the Hopf frequency associated to H_1. The velocity and feedback control fields, $\boldsymbol{u}$ and $\boldsymbol{v}$, are (pseudo) spectrally collocated and (3.7) is solved using the same technique as that used for (6.5). In the time-splitting scheme, the high-frequency term $\omega_c(\boldsymbol{v}-\boldsymbol{u})$ in (3.7a) is treated implicitly, while $\omega_c(\boldsymbol{u}-\boldsymbol{v})$ in (3.7b) is treated as a nonlinear term, using linear extrapolation.

The linear stability of the unstable BS found via SFD is analyzed using a standard Arnoldi iteration Saad [78] applied in two different ways. In one, the Navier–Stokes equations are linearized around BS and subjected to a small perturbation Tuckerman and Barkley [86]. In the other implementation, the action of the Jacobian is approximated with a divided difference constructed from the full nonlinear flow (6.5), evaluated at BS in the direction of the small perturbation, as described in Gómez *et al.* [23]. In both implementations, the corresponding Krylov subspaces consisted of $m = 96$ modes. Each mode was obtained using 1000 time steps in a time window of 2×10^{-3} viscous times, guaranteeing a sufficiently high Nyquist frequency to accurately resolve the frequencies of interest while avoiding aliasing effects for this choice of m. The nonlinear implementation has an additional time window constraint due to nonlinear growth effects, but allows the original DNS solver to be used with only minor modifications. With the time window and m used, both implementations gave

comparable results.

3.4 Results

3.4.1 Onset of Unsteadiness

The flow in the cubic lid-driven cavity for sufficiently small Re is steady and symmetric. This basic state, BS, has been shown to be stable for $Re \lesssim 1900$ [19, 37, 43, 44]. We find that for $Re \lesssim 1929$, static continuation converges to stable BS. However, for $Re = 1930$, using BS at $Re = 1929$ as initial condition, the evolution does not converge to a steady state. There is an initial adjustment to a state that is very similar to BS, and then over a long time (several viscous time units) there are small oscillations about BS that are slowly amplified. These oscillations are damped for $Re \lesssim 1929 \approx \mathrm{Re}_{\mathrm{H1}}$. Similar behavior was reported in Feldman and Gelfgat [19], who found $\mathrm{Re}_{\mathrm{H1}} = 1927$ from direct simulations.

Figure 3.2(a) shows the temporal evolution of both the kinetic energy E and the symmetry parameter S in the $Re = 1930$ case, using BS at $Re = 1929$ as initial condition. Note that we plot all time series with respect to the viscous time τ. During the early evolution ($\tau \lesssim 4$), the flow consists of very slowly amplified oscillations about the unstable BS, during which time the flow is symmetric, as indicated by $S \sim 10^{-24}$, which is essentially machine epsilon squared. Then for $\tau \in (4, 4.5)$, there is a rapid evolution away from the unstable BS, and by $\tau \approx 5$, the flow appears to have settled into a periodic limit cycle state, called LC1. There is a very slight increase in S from about 10^{-24} to 10^{-23}, but this level is still very close to being essentially zero. For a very long time (up to $\tau \sim 11$), it appears that LC1 is a stable symmetric limit cycle state. This behavior was also reported by Feldman and Gelfgat [19], but as pointed out by Kuhlmann and Albensoeder [37], LC1 is unstable for $Re > \mathrm{Re}_{\mathrm{H1}}$. By $\tau \approx 11$,

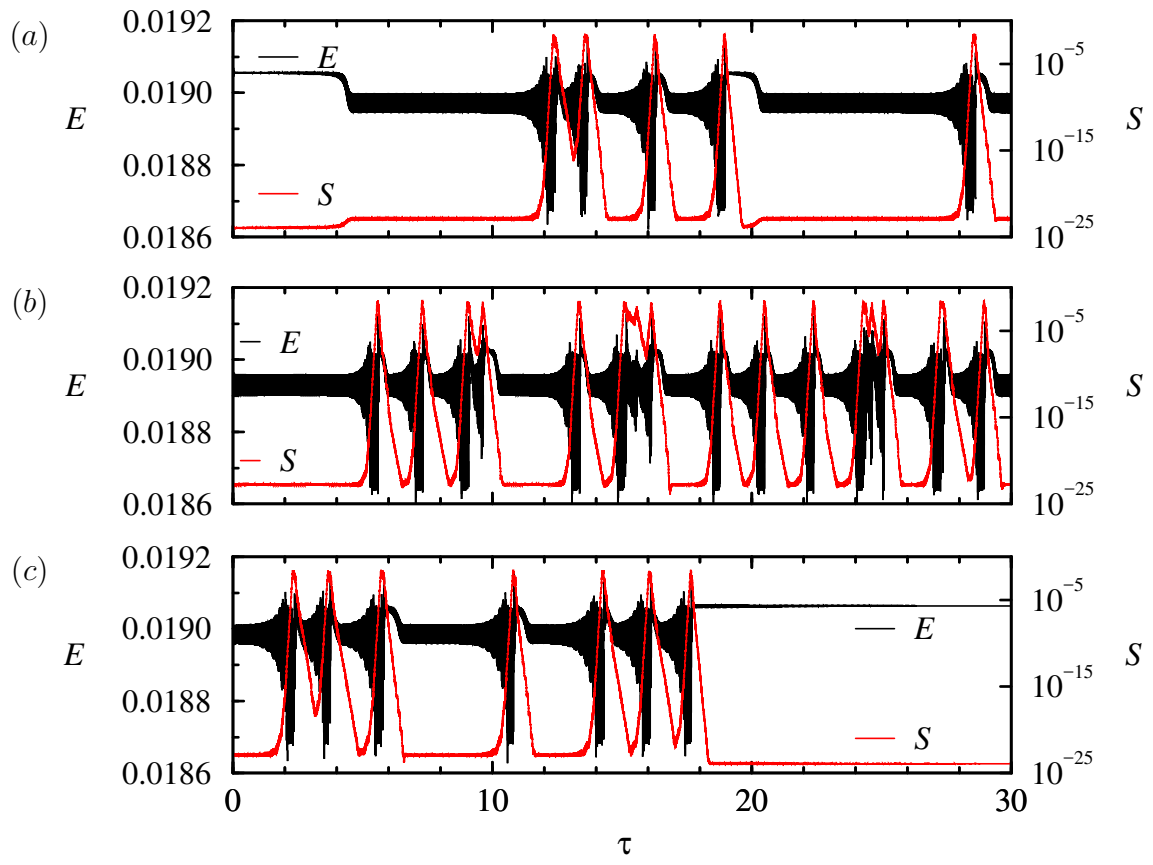

Figure 3.2: Time series of E (black) and S (red) for (a) $Re = 1930$, (b) $Re = 1940$ and (c) $Re = 1927$.

there is a rapid exponential growth in S, accompanied by rapidly growing oscillations in E which saturate at $\tau \approx 12$ to what appears to be another limit cycle LC2, and S has nonlinearly saturated to a level of order 0.01. The LC2 state persists for a very short time, about 10 oscillations or 0.2 viscous times, after which the flow evolves back toward LC1 with S decaying exponentially. A sequence of bursts, during which S grows exponentially again, then occurs. At about $\tau = 19$, Fig. 3.2(a) shows that following another burst, the flow evolves very close to BS, and then settles near LC1 for several viscous times before executing another burst visiting LC2 and BS.

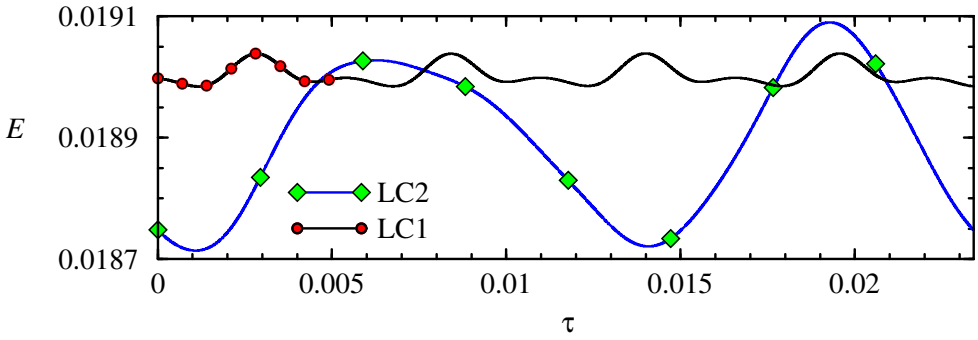

Figure 3.3: Time series of E for LC1 and LC2 at $Re = 1930$; the symbols correspond to the snap-shots over one period shown in Figs. 3.4 and 3.5.

The timing between the bursts is not uniform. This intermittent bursting behavior has been reported in Kuhlmann and Albensoeder [37], Loiseau [43], Loiseau *et al.* [44], and all studies note that the flow is essentially symmetric when near the unstable BS and LC1 states, and the broken symmetry is only strongly evident while it is near the LC2 state. None of the studies were able to determine the nature of the intermittency in the bursting behavior, but noted that the bursts become more frequent with increased Re, with the time intervals between bursts remaining irregular. Figure 3.2(b) shows a time series of E and S of the bursting state at $Re = 1940$, when started from the bursting state at $Re = 1930$.

For $Re < \mathrm{Re}_{\mathrm{H1}}$, evolutions starting from a bursting state at higher Re eventually tend to converge to BS. Figure 3.2(c) shows the evolution of E and S for $Re = 1927$ starting again from the bursting state at $Re = 1930$. The flow continues to burst for a long time (approximately 18 viscous times) before an excursion visiting the phase space neighborhood of BS. Since BS During the time that the flow is evolving close to LC1 or LC2, one is able to characterize these two unstable limit cycles. Figure 3.3 shows snippets of the times series of E at $Re = 1930$, taken from Fig. 3.2(a) at times when the flow is evolving close to either LC1 or LC2. The time origin in this figure

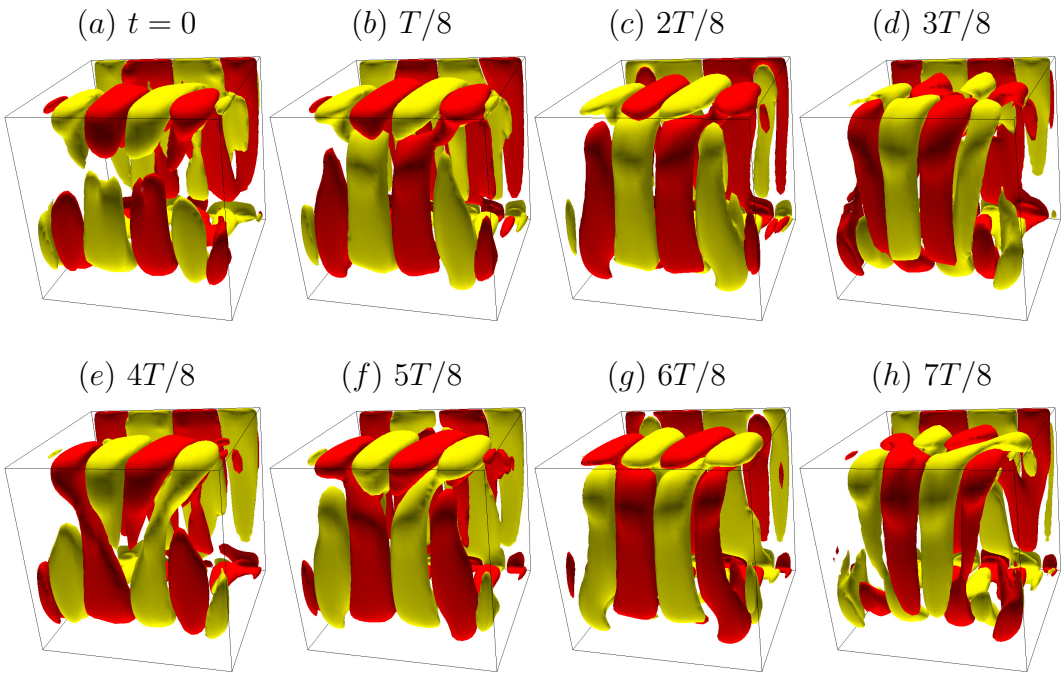

Figure 3.4: Isosurfaces of $H - \langle H \rangle$ at $\pm 10^5$ of LC1 at $Re = 1930$, over one period $T = 10.8$ (convective time units). See Supplemental Material Lopez *et al.* [51] for an animation.

has been shifted so as to directly compare the energy evolutions. The amplitude and period of the oscillation of LC2 are about four times those of LC1. Specifically, the period ratio of LC2 to LC1 at $Re = 1930$ is 4.18, which is very close to the values reported in Kuhlmann and Albensoeder [37], Loiseau [43], Loiseau *et al.* [44]. Also, the oscillations associated with LC1 and LC2 are very nonlinear, even though the value of Re is very close to $\mathrm{Re}_{\mathrm{H1}}$ where BS loses stability.

To better identify the flow features associated with the unsteadiness in LC1 and LC2, we consider the deviations away from their mean. Figures 3.4 and 3.5 show ten snap-shots over one period of the deviation in the helicity, $H - \langle H \rangle$, for LC1 and LC2, respectively, where $\langle \cdot \rangle$ denotes the time average over one period. The deviations are of comparable strength to the means; these are not small perturbations about the

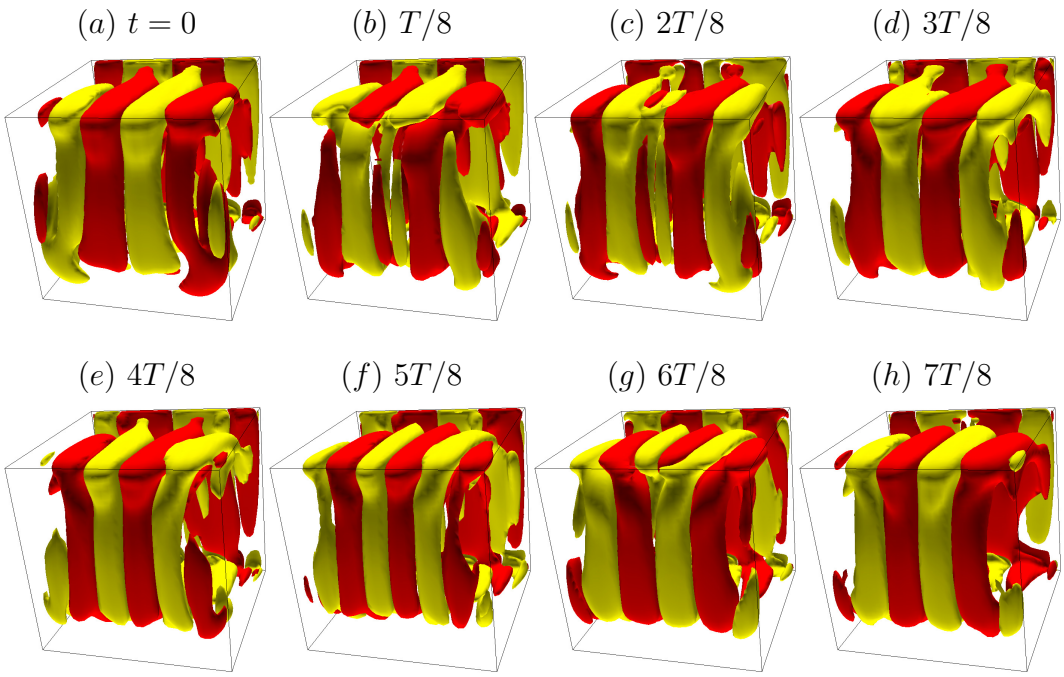

Figure 3.5: Isosurfaces of $H - \langle H \rangle$ at $\pm 10^5$ of LC2 at $Re = 1930$, over one period $T = 45.2$ (convective time units). See Supplemental Material Lopez *et al.* [52] for an animation.

mean. For both limit cycles, the deviation is associated with the streamwise vortices; the helicity associated with the spanwise endwall regions remains essentially steady throughout the oscillations. For both limit cycles, the deviations are $\mathcal{K}$-symmetric, but the details differ for the two. For LC1, the deviation rollers for the most part remain in their spanwise location, but progressively change their sign through the cycle. In contrast, the deviation rollers of LC2 travel in from the spanwise endwalls, and annihilate at the midplane $z = 0$ as new rollers are spawned at the spanwise endwalls, much like left- and right-traveling waves meeting at the $z = 0$ midplane. These flows are represented in the snap-shots shown in Figs. 3.4 and 3.5, but the associated online movies Lopez *et al.* [51, 52] provide a much clearer picture of their spatio-temporal features.

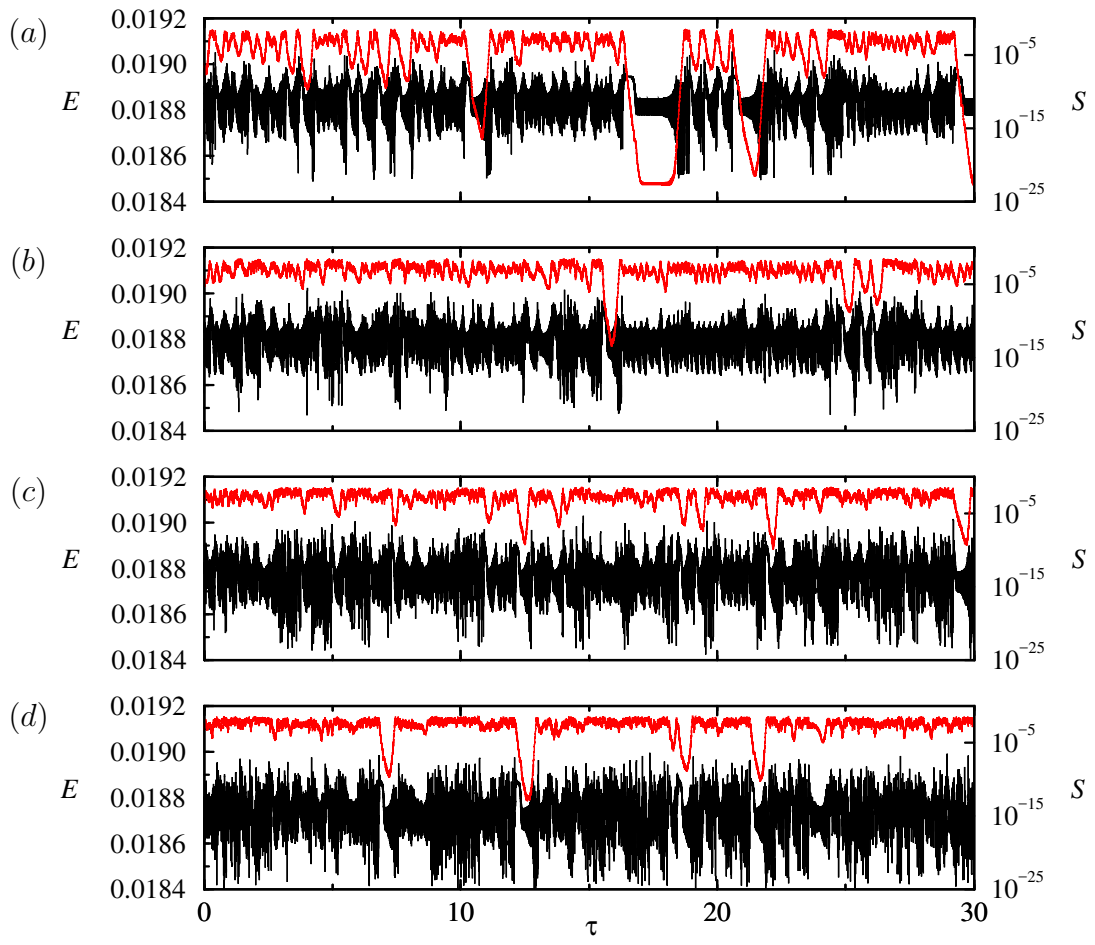

Figure 3.6: Time series of E (black) and S (red) at (a) $Re = 1970$, (b) $Re = 1980$, (c) $Re = 1990$ and (d) $Re = 2000$.

3.4.2 Intermittent Bursting

Figure 3.6 shows time series of E and S for a number of cases with $Re \geq 1970$, where the flow is much more irregular with many excursions away from and back toward the symmetry subspace (exponential decay and growth in S). The approaches to either BS or LC1 occur much less frequently than for the lower Re cases shown in Fig. 3.2. The bursts at these higher Re are occasionally into the symmetry subspace for a very brief period, rather than what was happening at lower Re, with the bursts

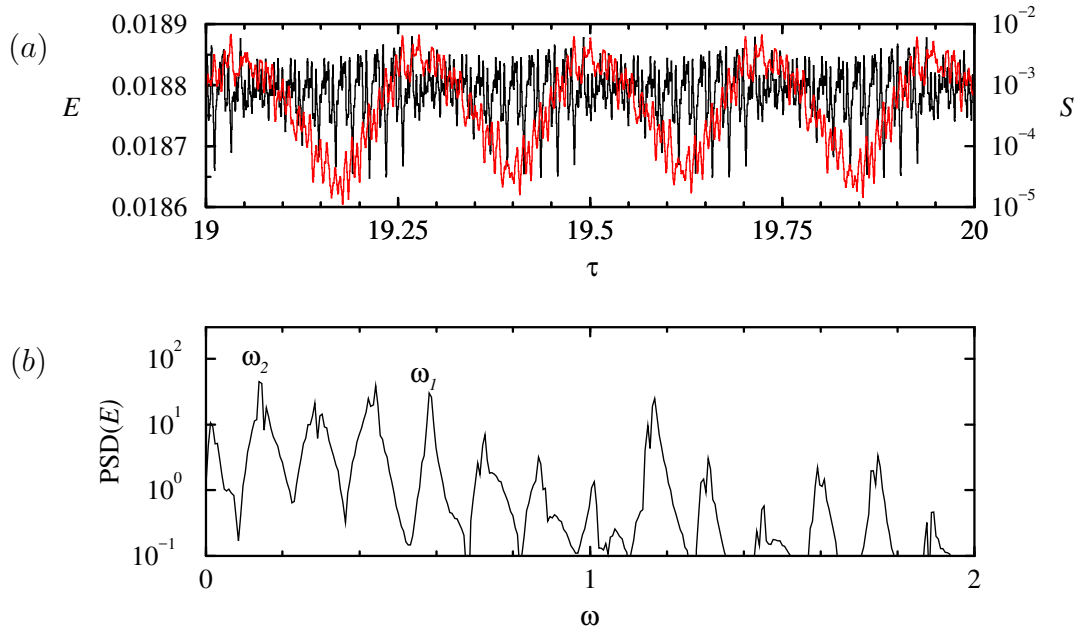

Figure 3.7: (a) Time series of E (black) and S (red) for $Re = 1980$, zoomed in for a time during which the evolution is close to the mixed mode QPa (with $\sigma(E) \approx 4 \times 10^{-5}$), and (b) power spectral density (PSD) of the time series of E shown in (a). The peaks corresponding to the frequencies of LC1 and LC2 are indicated.

providing short lived excursions out of the subspace. Also, the excursions are not visiting BS, LC1 or LC2 very often, but instead appear to be visiting quasi-periodic states and more complicated states, such as chaotic saddles.

The evolution at $Re = 1980$ shown in Fig. 3.6(b) has regular oscillations for $\tau \in (19, 20)$ which do not correspond to either LC1 or LC2. Figure 3.7(a) shows details of the E and S time series over this time. The quasi-periodic oscillation is close to being periodic; this is indicated by the low beat frequency modulating the signal. The power spectral density of the E time series over the time shown in Fig. 3.7(a) is presented in Fig. 3.7(b), which consists of peaks at the frequencies corresponding to the two limit cycles LC1 and LC2 (ω_1 and ω_2, respectively), plus

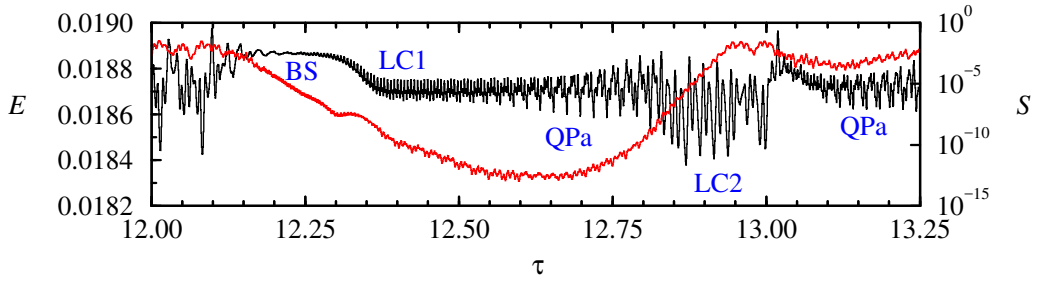

Figure 3.8: Time series of E (black) and S (red) for $Re = 2000$, zoomed in for a time during which there is a 'regular' burst event.

linear combinations of these. Also evident is a very low frequency peak corresponding to the beat frequency noticeable in the time series, which also shows up as sidebands to the main peaks. The frequencies ω_1 and ω_2 are close to a 4:1 ratio, and the beat frequency is a measure of how far the ratio is from being rational. In Fig. 3.6(a), the time series for $Re = 1970$ also shows that the flow is close to

At larger $Re = 2000$, the flow continues being spatio-temporally complicated. The chaotic behavior is similar to that reported in Loiseau [43]. However, careful inspection reveals episodes of 'orderly' bursts, as illustrated in Fig. 3.8, where at $\tau \approx 12.2$ the flow is very close to BS, then it evolves close to LC1, during which time S is decreasing exponentially to very small values. Then, at $\tau \approx 12.6$, the flow evolves away from LC1 to the mixed mode QPa with S increasing; QPa gives way to LC2 at $\tau \approx 12.9$ for 2 or 3 cycles by which time S has saturated. Then there is a another burst but the evolution does not make it to the neighborhood of BS this time and instead visits another quasi-periodic unstable state.

The limit cycle LC1 is symmetric, but is unstable to modulations, i.e. a Neimark–Sacker bifurcation, and the new frequency introduced is that of LC2. LC2 is unstable to symmetry breaking. For most of the time, the time series appears to be temporally chaotic, suggesting that the stable and unstable manifolds of the saddle states

(BS, LC1, LC2, and QPa) intersect transversely, leading to chaotic dynamics interspersed with regular episodes during which the flow approaches sufficiently close to one or other saddle state, but eventually the dynamics are directed by the unstable manifolds. The mixed mode QPa acts as a gateway in and out of the symmetric subspace and S grows and decays exponentially during the beat cycle. Further evidence supporting this is presented in the following sections where the flow is further analyzed.

3.4.3 Spectral Analysis of BS

Now that we have explored the dynamics as Re is increased beyond $\mathrm{Re}_{\mathrm{H1}}$ via DNS, and have reproduced the DNS results of previous investigations, we analyze the results. As was already done by Loiseau [43], we begin by using SFD to obtain the unstable BS for $Re > \mathrm{Re}_{\mathrm{H1}}$, and then we determine its leading eigenmodes using Arnoldi iterations.

Figure 3.9 shows the real and imaginary parts of the three leading eigenvalue pairs as functions of Re. The leading eigenvalue pair (which we simply refer to as λ_1) acquires positive real part at $Re \approx 1928.9$, which is consistent with the DNS results presented above. The imaginary part is approximately 0.5832 (using the convective time scale), which is very close to the oscillation frequency of LC1 and to the Hopf frequency reported by Loiseau [43], Loiseau *et al.* [44]. The second leading eigenpair, λ_2, has a real part that is growing faster with Re than that of λ_1, but starting from a much more negative value. The real part of λ_2 becomes positive via a second Hopf bifurcation, H_2, at $Re = \mathrm{Re}_{\mathrm{H2}} \approx 2089$. The imaginary part of λ_2 is approximately 0.1407, which is very close to the oscillation frequency of LC2. This value is also very close to the imaginary part of λ_2 reported by Loiseau [43], Loiseau *et al.* [44], however they did not consider the linear stability of BS beyond $Re = 2000$, and so they did not

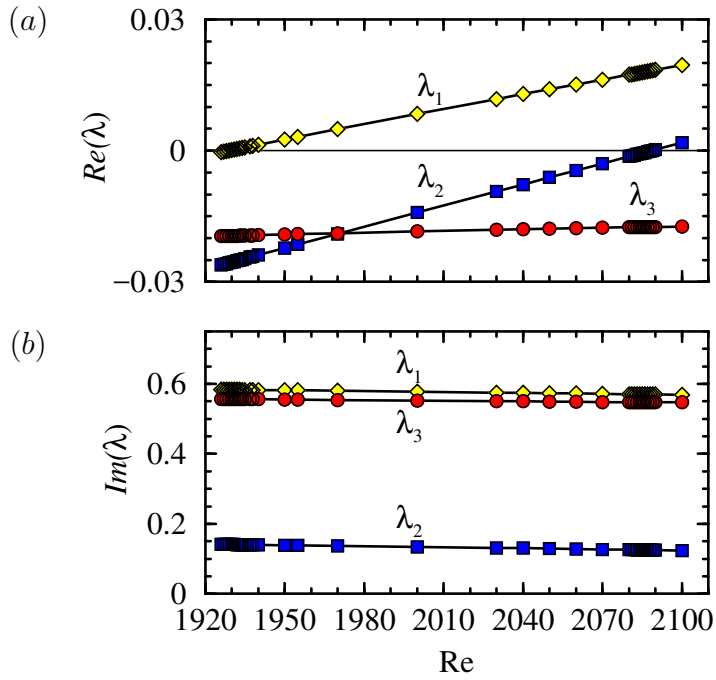

Figure 3.9: Real and Imaginary parts of the three leading eigenvalues of BS as functions of Re, using the convective time scale.

determine $\mathrm{Re}_{\mathrm{H2}}$. The eigenvectors associated with λ_1 and λ_2 are reflection symmetric. The third leading eigenvalue pair, λ_3, has a real part that remains negative over the Re range considered, and varies very slowly with Re, suggesting that if it is involved in a bifurcation of BS, it would be at a much larger Re and so is not likely to have an impact on the dynamics at the Re values under consideration. It has an imaginary part slightly smaller than λ_1, and the associated eigenvector is anti-symmetric. This is consistent with the findings of Loiseau [43], Loiseau *et al.* [44]. This is also consistent with the fact that this mode does not show up when the spectral analysis is done in the symmetric subspace.

3.4.4 Details of the Subcritical Hopf Bifurcation to LC1

Linear stability analysis identifies the onset of a bifurcation, but does not give information about whether it is super- or sub-critical; that requires nonlinear information for its determination. Both Feldman and Gelfgat [19] and Kuhlmann and Albensoeder [37] presented DNS evidence that the Hopf bifurcation H_1 at which BS first loses stability is subcritical. We now focus on the details of this subcritical Hopf bifurcation. The generic behavior in the neighborhood of a subcritical Hopf bifurcation is that the steady equilibrium (BS) loses stability at $Re = \mathrm{Re}_{\mathrm{H1}} \approx 1929 \pm 1$ and an unstable limit cycle (LC1) is spawned to lower Re. The next order nonlinear terms in the normal form give that the unstable limit cycle undergoes a cyclic-fold bifurcation (also known as a saddle-node bifurcation of limit cycles) at $Re = \mathrm{Re}_{\mathrm{CF1}} < \mathrm{Re}_{\mathrm{H1}}$. We have numerically determined (see below for details) $\mathrm{Re}_{\mathrm{CF1}} \approx 1913.5 \pm 0.5$. For $Re < \mathrm{Re}_{\mathrm{CF1}}$ there are no limit cycles locally in phase space, and for $Re > \mathrm{Re}_{\mathrm{CF1}}$ there are two limit cycles. One is the unstable lower-branch cycle that was spawned at the subcritical Hopf bifurcation, and the other is a stable upper-branch cycle that continues to exist to higher Re Strogatz [see 84, Ch. 8.2]. The DNS results presented in the previous section, as well as those of Kuhlmann and Albensoeder [37], Loiseau [43], Loiseau *et al.* [44], show that the upper-branch LC1 is unstable for $Re \gtrsim \mathrm{Re}_{\mathrm{H1}}$, but only very weakly so in the sense that there is a very long-lived transient that remains close to LC1 before bursting sets in.

The lower-branch LC1 is not directly accessible via DNS as it is unstable. However, by implementing EST Itano and Toh [28], Schneider *et al.* [80] using linear combinations of the upper-branch LC2 (which is stable in the symmetry subspace for $Re \in [\mathrm{Re}_{\mathrm{CF1}}, \mathrm{Re}_{\mathrm{H1}}]$, see Section 3.4.5) and BS as initial conditions, we have been able to obtain the unstable lower-branch LC1 as a long transient. A pair of tran-

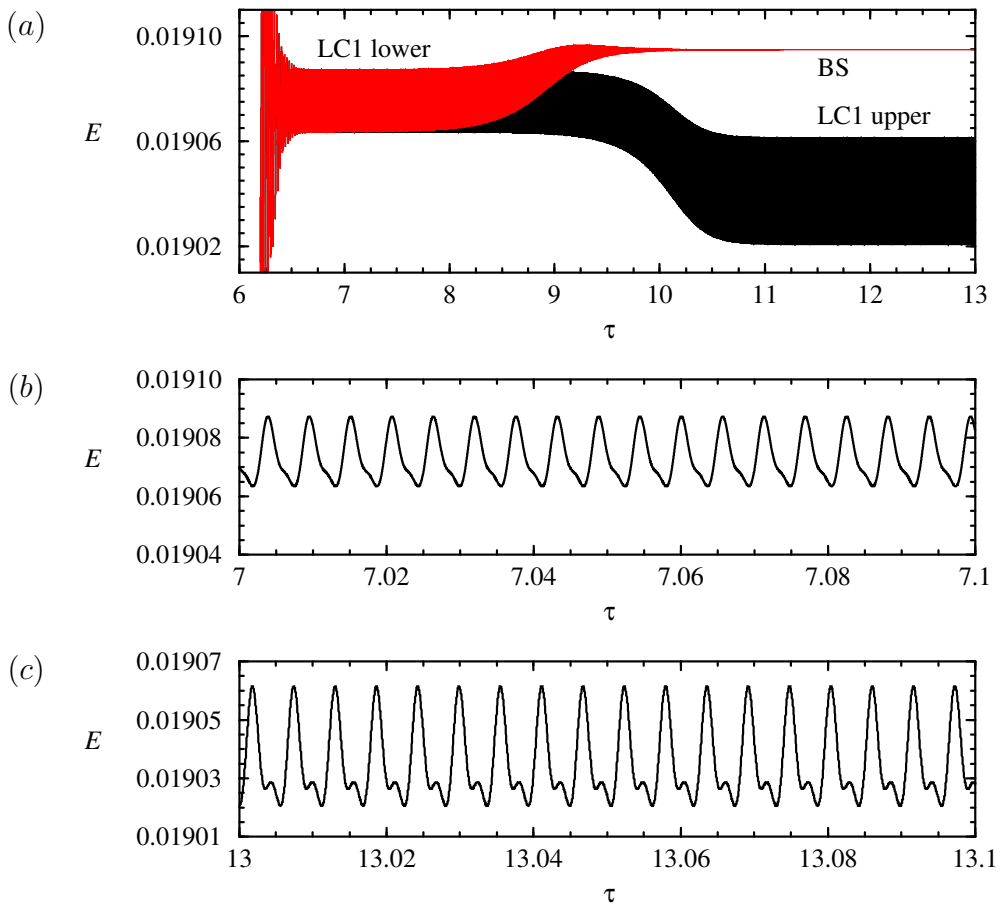

Figure 3.10: Time series of E for EST simulations between BS and upper-branch LC2 at $Re = 1916$, showing (a) two transients using αBS + $(1-\alpha)$(LC2 upper) as the initial condition, with $\alpha = 0.644442$ (black, evolving to upper-branch LC1) and $\alpha = 0.644443$ (red, evolving to BS); (b) shows a close-up of the time series for $\left[{}^{\tau\in[7.0,7.1}\right]$ during which the transients are very close to lower-branch LC1, and (c) shows the upper-branch LC1 oscillations for $\left[{}^{\tau\in}_{13.0,13.1]}\right]$.

sients at $Re = 1916$ using αBS $+ (1-\alpha)$(LC2 upper) as the initial condition, with $\alpha = 0.644442$ and $\alpha = 0.644443$ are shown in Fig. 3.10. With these two slightly different values of α, the transient remains close to the unstable lower-branch LC1 for about 1.5 viscous times, corresponding to about 270 oscillations, before the transient corresponding to the larger α evolves and converges to BS, while the other transient converges to the upper-branch LC1. Close-ups of the oscillations corresponding to lower- and upper-branch LC1 are shown over 0.1 viscous times in Fig. 3.10(b, c); they both have approximately the same period, and the upper-branch LC1 has larger amplitude and the form of its oscillation is more nonlinear. During the entire duration of these simulations, S remains at machine zero levels, indicating that the dynamics is occurring in the symmetry subspace.

By implementing EST for $Re \in [\mathrm{Re}_{\mathrm{CF1}}, \mathrm{Re}_{\mathrm{H1}}]$, we have been able to capture the lower-branch LC1. Figure 3.11 is a bifurcation diagram in the neighborhood of the subcritical Hopf bifurcation H_1, using the standard deviation in the energy oscillations $\sigma(E)$ as the state variable and Re as the bifurcation parameter. We use $\sigma(E)$ as a measure of the oscillation amplitude as the oscillations are far from harmonic, and so a peak-to-peak measure is not a good measure as it typically overestimates the average deviation away from the mean. Also shown is the cyclic-fold bifurcation CF_1 where the lower- and upper-branch LC1 meet at $\mathrm{Re}_{\mathrm{CF1}} \approx 1913.5 \pm 0.5$. For $Re < \mathrm{Re}_{\mathrm{H1}}$, BS is stable, and for $Re > \mathrm{Re}_{\mathrm{H1}}$, BS loses stability acquiring one unstable (eigen) direction. Since the bifurcation is subcritical, with LC1 being spawned to lower Re, LC1 also has one unstable direction. At CF_1, LC1 folds from the lower to the upper branch and becomes stable (no unstable direction). We verified the stability of LC1 via DNS at $Re = 1916$ over 120 viscous time units, corresponding to over 20000 oscillations. LC1 loses stability in a Neimark–Sacker bifurcation NS_1 (a Hopf bifurcation of limit cycles) at $Re = \mathrm{Re}_{\mathrm{NS1}} \approx 1919 \pm 1$. For $Re > \mathrm{Re}_{\mathrm{NS1}}$, LC1 has one unstable direction.

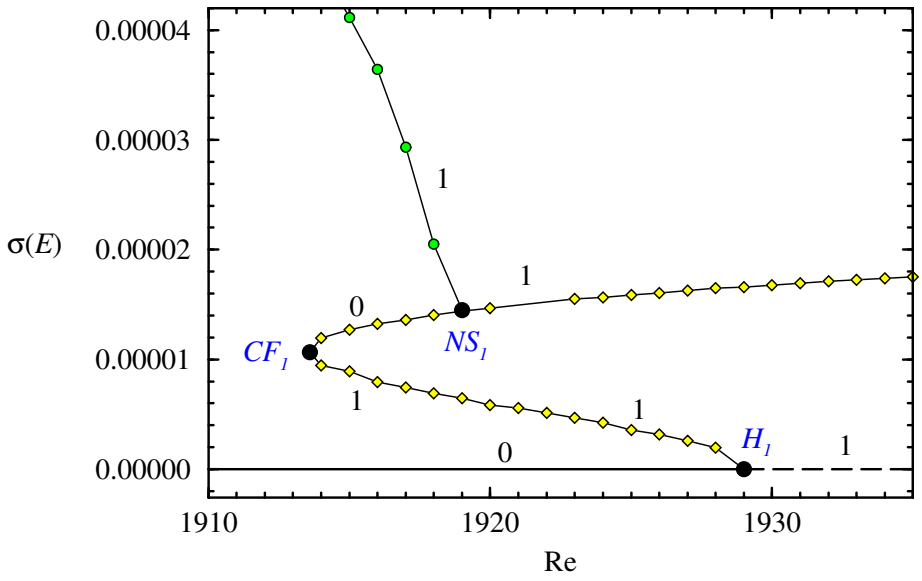

Figure 3.11: Bifurcation diagram in the neighborhood of the subcritical Hopf bifurcation. The solid and dashed lines with $\sigma(E) = 0$ correspond to BS, the curve with the yellow diamonds corresponds to LC1, and the curve with green circles corresponds to a mixed-mode between LC1 and LC2. The subcritical Hopf where BS loses stability is labeled H_1, the cyclic-fold bifurcation between the lower and upper branches of LC1 is labeled CF_1, and the Neimark–Sacker bifurcation on the upper branch of LC1 is labeled NS_1. Along each equilibrium solution branch segment, there is an integer indicating the number of unstable directions associated with the equilibrium.

The details of how NS_1 is determined will be given below in §3.4.5, but briefly it involved using EST with LC2 (stabilized in the symmetry subspace) and BS. For some combinations, we found a long-lived transient with a quasi-periodic signature, QPs. Figure 3.12 shows two such transients at $Re = 1916$ that both stay close to QPs for over three viscous times and then one evolves toward LC2 and the other toward LC1. Also shown in the figure are the time series and corresponding power spectral density (PSD) of E over a time interval when the flow is close to QPs. It is clear that QPs is a

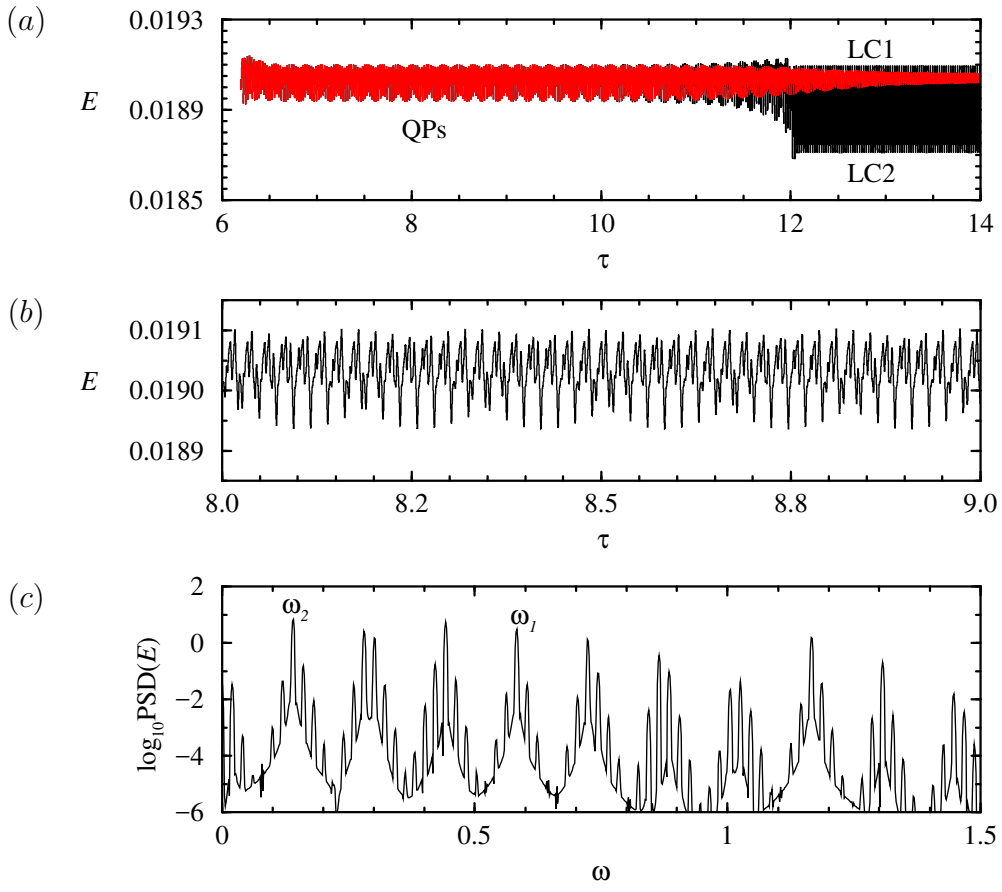

Figure 3.12: Time series of E for EST simulations in the symmetry subspace between BS and upper-branch LC2 at $Re = 1916$, showing (a) two transients using αBS + $(1 - \alpha)$(LC2 upper) as the initial condition, with $\alpha = 0.6294285$ (black, evolving to upper-branch LC2) and $\alpha = 0.6294286$ (red, evolving to upper-branch LC1), (b) shows a close-up of the time series for $\tau \in [8.0, 8.3]$ during which the transients are very close to QPs, and (c) is the power spectral density (PSD) of the time series of E over $\tau \in [7.0, 10.]$.

mixed-mode of LC1 and LC2. EST simulations show that QPs exists for $Re < \mathrm{Re}_{\mathrm{NS1}}$, i.e. the Neimark–Sacker bifurcation of LC1 is subcritical, and so QPs has one unstable direction. More details are presented in §3.4.5. The important point here is that the upper-branch LC1 had to lose stability for the DNS results showing bursting (as in Fig. 3.2) to make sense. Note that the upper-branch LC1 is only stable over the range $\mathrm{Re}_{\mathrm{CF1}} < Re < \mathrm{Re}_{\mathrm{NS1}}$, with $(\mathrm{Re}_{\mathrm{NS1}} - \mathrm{Re}_{\mathrm{CF1}})/(\mathrm{Re}_{\mathrm{NS1}} + \mathrm{Re}_{\mathrm{CF1}}) \approx 0.0014$, which is very small and easily missed; Kuhlmann and Albensoeder [37], Loiseau [43], Loiseau *et al.* [44] do not report LC1 as being stable for any Re.

3.4.5 Dynamics in the Symmetry Subspace

The intermittent bursting behavior for $Re \approx \mathrm{Re}_{\mathrm{H1}}$, with the bursts correlated with large increases in the flow asymmetry, is a poorly understood feature of the onset of unsteadiness in the cubic lid-driven cavity Kuhlmann and Albensoeder [37], Loiseau [43], Loiseau *et al.* [44]. In this section we explore the flow dynamics in the symmetry subspace in order to further investigate what dynamics are involved. Numerically, the flow is restricted to the subspace simply by setting $\boldsymbol{u} = 0.5(\boldsymbol{u} + \mathcal{A}(\mathcal{K})\boldsymbol{u})$ at every time step (and intermediate time step) in the simulation.

Figure 3.13 shows a typical evolution in the subspace and compares it to that in the full space. The figure includes the time series from Fig. 3.2(b), cropped to $\tau \in [4.5, 6.5]$ to focus on the first burst event. From Fig. 3.2(b), we saw that the flow stays very close to LC1 for over 4 viscous times before undergoing a burst. In Fig. 3.13, we now appreciate that the flow starts to depart from LC1 before there is any appreciable increase in its asymmetry, i.e. S does not start to grow until $\tau \approx 4.9$, but by $\tau = 4.6$ there is a significant departure from the periodic signal associated with LC1 due to a modulation. This modulation is due to the Neimark–Sacker bifurcation NS_1 at which QPs is spawned. By $\tau \approx 5.2$, QPs is large and becomes irregular while

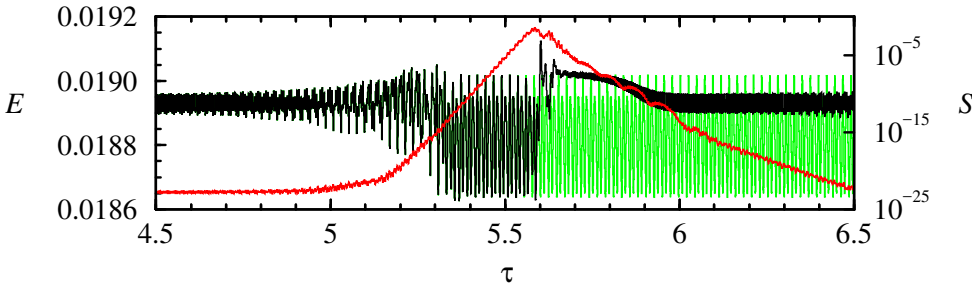

Figure 3.13: Time series of E and S at $Re = 1940$. Shown are the same time series from Fig. 3.2(b), but zoomed in for $\tau \in [4.5, 6.5]$ (black for E and red for S), as well as the time series starting with the same initial condition at $\tau = 0$, but computed in the symmetry subspace (only E is shown, in green, as $S = 0$ in the subspace).

S is growing exponentially. There is a rapid adjustment in the flow and by $\tau \approx 5.4$, the flow transient approaches close to LC2. During this time, S is still small, but continues to grow exponentially. Over this same period of time, the evolution in the symmetric subspace is virtually identical (except, of course, that $S = 0$). This is clear evidence that the transition from LC1 to LC2 via modulation is not due to symmetry breaking; LC1 is unstable in the subspace, as is BS at this Re, and there is an eventual evolution to LC2 which is virtually identical to that in the full space.

The evolution in the subspace converges onto LC2 at $\tau \approx 5.4$ and remains at LC2 indefinitely. In the full space, LC2 is unstable to symmetry breaking. By $\tau \approx 5.55$, there is an appreciable difference between the kinetic energy of LC2 in the full space and that in the subspace. As S saturates at $\tau \approx 5.6$, the evolution quickly evolves away from the unstable LC2, briefly approaches the unstable BS, which nevertheless is symmetric, and so during the approach to BS S decays exponentially. Since BS is unstable, the evolution ends up tracking an unstable manifold away from BS and approaches LC1. In the full space (at $Re = 1940$ under consideration) LC1 is unstable, and like BS it too is symmetric. Hence, while the evolution is in the neighborhood

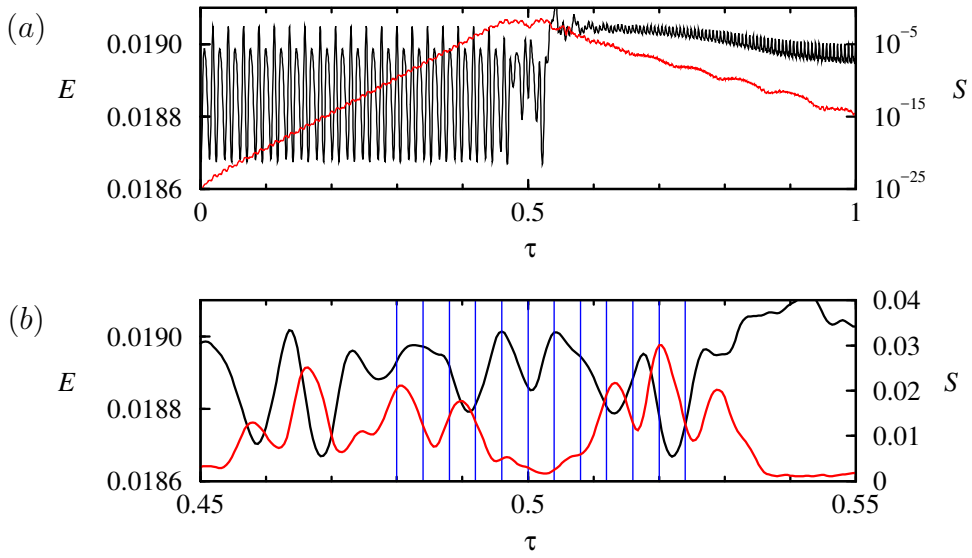

Figure 3.14: Time series of E (black) and S (red) for $Re = 1930$, (b) is a close-up of (a) near $\tau = 0.5$; the vertical blue lines correspond to the times of the snap-shots shown in Fig. 3.15.

of LC1, S continues to decay exponentially, albeit at a different rate. LC1 becomes modulated by $\tau \approx 6.2$, but this modulation is also symmetric and S continues to decay exponentially. As the modulation amplitude grows, another burst is initiated, as shown in Fig. 3.2(b). So, in summary, we have for $Re \gtrsim 1930$ that both BS and LC1 are unstable but symmetric, and LC2 is stable in the subspace, but unstable to symmetry breaking.

It is now interesting to examine the symmetry-breaking of LC2 in the full space. To do this, we have first computed LC2 in the subspace at $Re = 1930$, and used that solution as initial condition for a simulation in the full space at the same $Re = 1930$. Figure 3.14(a) shows the evolutions of E and S in this simulation. Initially, S is at machine epsilon squared and grows exponentially. During this early part of the evolution, the flow essentially corresponds to the LC2 state that is stable in the

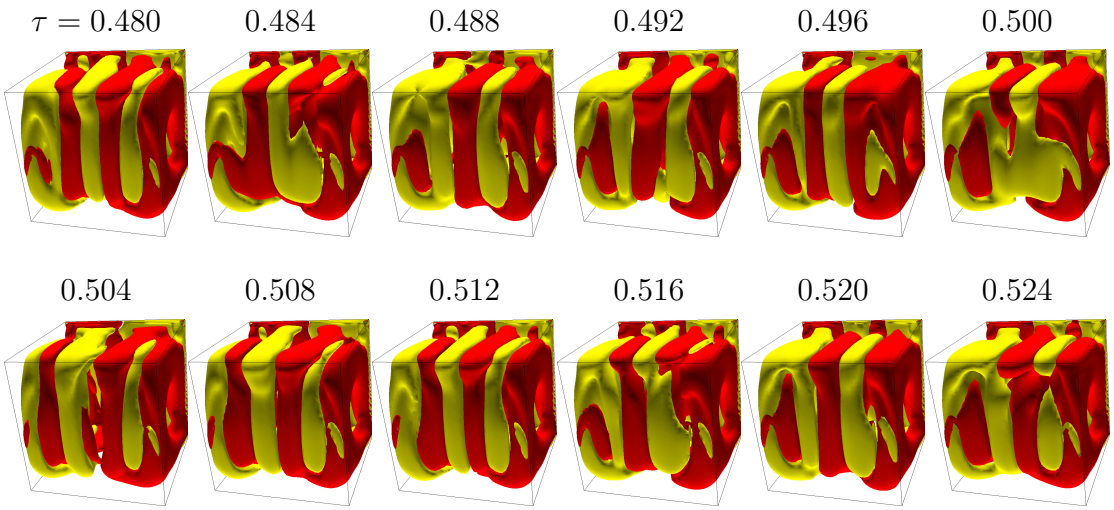

Figure 3.15: Helicity isosurfaces at $H = \pm 10^5$ for $Re = 1930$ during the transition from LC2 at times indicated by the blue vertical lines in Fig. 3.14(b). See Supplemental Material Lopez *et al.* [53] for an animation from $\tau = 0.344$ to 0.664.

subspace, until $\tau \approx 0.5$ by which time S has grown to $\sim 10^{-3}$ and a bursting event very similar to those shown in Fig. 3.2(a) is initiated. Figure 3.14(b) is a close-up of the evolution shown in Fig. 3.14(a), covering the duration of the burst when S is maximal and just as the flow transitions toward LC1 and S decays exponentially. The twelve vertical (blue) lines in the figure correspond to snap-shots of the helicity isosurfaces shown in Fig. 3.15. Note that these isosurfaces are of the full solution, in contrast to those shown in Figs. 3.4 and 3.5 which showed helicity isosurfaces of the deviation away from the mean; during the bursting event, there is no meaningful mean. As such, the isosurfaces include the contribution from the spanwise endwall regions. The nature of the flow is difficult to discern from the twelve snap-shots, but the corresponding online movie Lopez *et al.* [53] is very insightful. The movie starts at $\tau = 0.344$ when the flow is very near LC2 and consists of waves traveling symmetrically in from the two spanwise endwalls and annihilating at the midplane,

i.e. the typical LC2 behavior described earlier. Then, in the transitional stage with $\tau \in (4.8, 5.2)$, during which S has saturated, the flow consists of waves traveling from one spanwise endwall to the other. This traveling wave TW is very unstable and only lasts for about one and a half cycles, but it is clearly discernable in the movie. In principle, both left and right traveling waves are possible, and which is observed depends on the details of the symmetry-breaking perturbation at the time. The instability of TW is likely due to confinement effects in the cubic cavity. Such traveling waves states have been observed experimentally in an oscillatory lid-driven cavity of large spanwise extent Leung *et al.* [41], and are related to the symmetry breaking dynamics in the spanwise periodic idealization of that flow Blackburn and Lopez [7], Marques *et al.* [66], Blackburn *et al.* [8]. Following the instability of TW, the movie shows a rapid transition to oscillations that are converging toward LC1.

The differences between the evolutions in the full space and in the subspace for $Re < \mathrm{Re}_{\mathrm{H1}} \approx 1929$ also provide significant insight into the dynamics involved. As mentioned in the previous section, evolutions for $Re \lesssim 1930$ in the full space eventually converge onto the stable BS, independently of initial conditions, as BS is the only stable state at these Re, except for $\mathrm{Re}_{\mathrm{CF1}} < Re < \mathrm{Re}_{\mathrm{NS1}}$, an interval of only 6 units in Re ($[\mathrm{Re}_{\mathrm{NS1}} - \mathrm{Re}_{\mathrm{CF1}}]/[\mathrm{Re}_{\mathrm{NS1}} + \mathrm{Re}_{\mathrm{CF1}}] \approx 0.0014$), over which LC1 is also stable. In the subspace however, LC2 is stable down to $Re = \mathrm{Re}_{\mathrm{CF2}} \approx 1872$, where it undergoes a cyclic-fold bifurcation CF_2, and does not exist for lower Re, leaving BS as the only stable state for $Re < \mathrm{Re}_{\mathrm{CF2}} \approx 1871.5 \pm 0.5$.

For $Re \gtrsim \mathrm{Re}_{\mathrm{CF2}}$, we have implemented EST in the symmetry subspace, using linear combinations of BS and LC2 in order to localize the lower-branch LC2 involved in the cyclic-fold bifurcation CF_2. In the subspace, near the cyclic-fold bifurcation, the lower-branch LC2 is a saddle limit cycle with one unstable direction. Figure 3.16 shows time series of E for a pair of EST simulations in the subspace at $Re = 1883$,

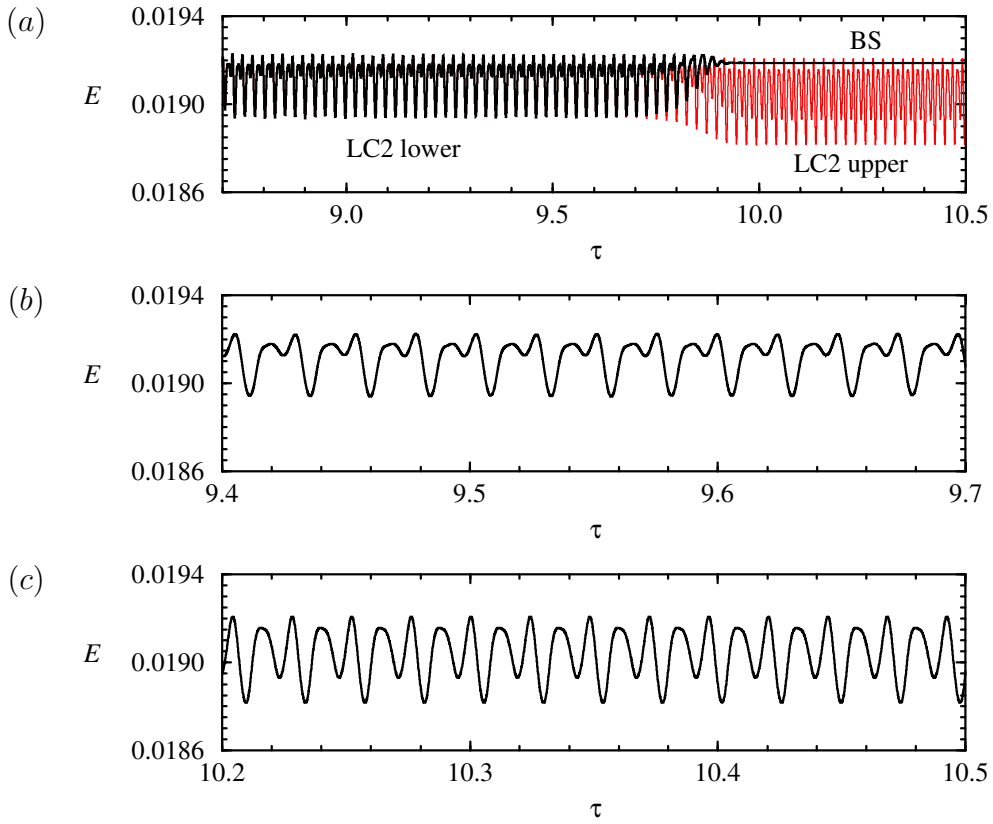

Figure 3.16: Time series of E for EST simulation in the symmetric subspace between BS and upper-branch LC2 at $Re = 1883$, showing (a) two transients using $\alpha\text{BS} + (1 - \alpha)(\text{LC2 upper})$ as the initial condition, with $\alpha = 0.39042645732$ (black, evolving to BS) and $\alpha = 0.39042645730$ (red, evolving to upper-branch LC2), (b) presents a zoom of the time series for $\left[{}^{\tau\in}_{9.4,9.7}\right]$ during which the transients are very close to lower-branch LC2, and (c) shows the upper-branch LC2 oscillations for $\tau \in [10.2, 10.5]$.

where the initial conditions were (α)BS$+(1-\alpha)$(LC2 upper) with $\alpha = 0.39042645732$ that ended up evolving to BS and $\alpha = 0.39042645730$ that ended up evolving to upper-branch LC2. With these choices of α, the evolutions remain very close to the saddle lower-branch LC2 for about one viscous time; Fig. 3.16(b) is a close-up of the E time series over $\tau \in [9.4, 9.7]$ to more clearly see the oscillations of lower-branch LC2. From this we have extracted the standard deviation of the oscillation, $\sigma(E)$, and the corresponding frequency. Figure 3.16(c) is a close-up over $\tau \in [10.2, 10.5]$ of the time series that evolves to LC2. We have made movies of these two oscillations (not shown) and they are essentially the same as the one associated with upper-branch LC2 in Fig. 3.5.

The identification of the unstable lower-branch LC2 emanating from CF_2 is relatively straight-forward because in the symmetry subspace its unstable manifold is only one-dimensional and can parameterized by α: lower-branch LC2 is the edge state between upper-branch LC2 and BS, corresponding to a single value of α. With deviations only in the 11th significant figure away from this value of α, we obtain transients that remain very close to lower-branch LC2 for more than one viscous time. Larger deviations in α reduce this time considerably. Repeating the EST simulations to higher Re also reduces the time spent near lower-branch LC2 for the same level of refinement in α. For $Re \gtrsim 1886$, EST simulations with refinements of α to different values lead to long transients close to either lower-branch LC2, much as been just described, or to QPs as illustrated in Fig. 3.12 for $Re = 1916$. This indicates that lower-branch LC2 undergoes a Neimark–Sacker bifurcation, NS_2 (by doing several EST simulations at many Re, we estimate this to occur at $Re = \mathrm{Re}_{\mathrm{NS2}} \approx 1886 \pm 3$), spawning the mixed-mode QPs supercritically (i.e. to larger Re). The supercriticality of NS_2 means that lower-branch LC2 acquires another unstable direction for $Re > \mathrm{Re}_{\mathrm{NS2}}$, totaling two in the symmetry subspace, and QPs has the same number

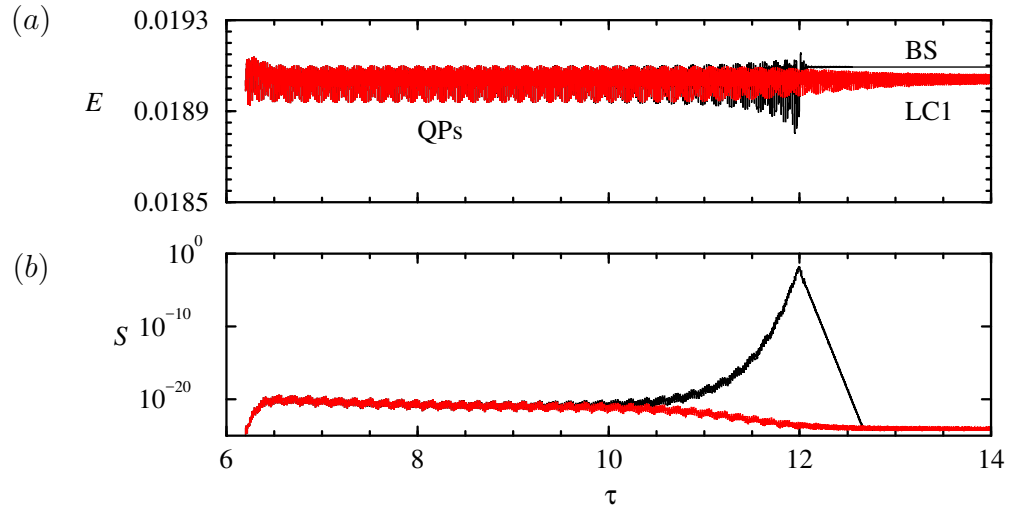

Figure 3.17: Time series of (a) E and (b) S for EST simulations at $Re = 1916$, showing two transients using $\alpha\text{BS} + (1-\alpha)$(LC2 upper) as the initial condition, with $\alpha = 0.6294285$ (black, evolving to BS) and $\alpha = 0.6294286$ (red, evolving to upper-branch LC1). These EST runs are the same as those shown in Fig. 3.12, but executed in the full space.

of unstable directions as the lower-branch LC2 from which it bifurcates, namely one. Having only one unstable direction, QPs was tracked via EST all the way to NS_1 where it is absorbed by upper-branch LC1 (see Fig. 3.11 and the accompanying text for details). For lower-branch LC2, having two unstable directions for $Re > \text{Re}_{\text{NS2}}$ means that localizing it using bisection in α is no longer possible. We have been able to localize lower-branch LC2 up to $Re = 1914$, but for larger Re a different strategy is needed.

The evolution of E and S in the full space at $Re = 1916$ when started from QPs, which is now unstable in at least two directions, shown in Fig. 3.17. In addition to the unstable direction in the symmetry subspace, QPs now has an additional unstable direction out of the subspace, illustrated by the growth of S associated to the smaller value of α. For that initial condition, QPs loses stability via symmetry breaking, and

Bifurcation	Re
H_1: first Hopf of BS	1929 ± 1
H_2: second Hopf of BS	2089 ± 1
CF_1: cyclic-fold of LC1	1913.5 ± 0.5
CF_2: cyclic-fold of LC2	1871.5 ± 0.5
NS_1: Neimark–Sacker of LC1 (upper branch)	1919 ± 1
NS_2: Neimark–Sacker of LC2 (lower branch)	1886 ± 3

Table 3.1: List of bifurcations encountered, and the critical Re at which they occur.

the dynamics eventually visits the basin of attraction of BS, while the state originating from an initial condition associated to the slightly larger α remains symmetric and evolves toward LC1, which is the only other stable state in the full space at this Re besides BS. The similarity in spectral signatures between QPs in Fig. 3.12 and QPa in Fig. 3.7 obtained at a slightly lower Re suggests that the symmetry breaking of QPs indeed results in QPa (a pair of them, related by the reflection).

3.4.6 Summary of Identified States

All the information acquired using the various numerical techniques is used to construct Fig. 3.18, showing the standard deviation in the kinetic energy $\sigma(E)$ and the oscillation frequency ω of the states found. A brief overview of the various states in Fig. 3.18, how they were found, and their stability properties that we have been able to educe, now follows:

- BS — the basic state, by definition is symmetric. It first loses stability at $Re = \mathrm{Re}_{\mathrm{H1}}$ in a subcritical Hopf bifurcation H_1, and then suffers a second Hopf bifurcation H_2 at $Re = \mathrm{Re}_{\mathrm{H2}}$. The unstable BS was computed via SFD and the

bifurcations were identified using Arnoldi iterations.

- LC1 — this limit cycle is spawned from BS at H_1 subcritically toward lower Re. At onset, it has one unstable direction. It undergoes a cyclic-fold bifurcation CF_1 at $Re = \mathrm{Re}_{\mathrm{CF1}}$, where it (the lower-branch) is folded to continue to higher Re (the upper-branch). The upper-branch is stable for $Re \in (\mathrm{Re}_{\mathrm{CF1}}, \mathrm{Re}_{\mathrm{NS1}})$; at $\mathrm{Re}_{\mathrm{NS1}}$ it undergoes a Neimark–Sacker bifurcation and for $Re > \mathrm{Re}_{\mathrm{NS1}}$, LC1 has one unstable direction. Even though it is unstable, the growth rate of small perturbations away from it is very slow, and its characteristics can be determined via DNS with initial conditions that are reasonably close to LC1. The lower branch LC1 was computed using EST with linear combinations of BS and upper-branch LC2 as well as linear combinations of BS and upper-branch LC1. LC1 (both lower and upper branches) are stable to symmetry breaking; this was determined by monitoring S during simulations.

- LC2 — this limit cycle was first found by restricting DNS to the symmetric subspace. For $Re > \mathrm{Re}_{\mathrm{H1}}$, there are no stable steady or time-periodic solutions in the full space, but in the subspace any initial condition evolves to LC2. LC2 was continued down to $Re = \mathrm{Re}_{\mathrm{CF2}}$ where it undergoes a cyclic-fold bifurcation CF_2, and is folded to form lower-branch LC2 which has one unstable direction in the subspace for $Re \in (\mathrm{Re}_{\mathrm{CF2}}, \mathrm{Re}_{\mathrm{NS2}})$. This lower-branch LC2 was computed using EST in the subspace with combinations of BS and upper-branch LC2 as initial conditions. DNS in the full space with LC2 (upper and lower) as initial conditions show that LC2 is unstable to symmetry breaking. An example of such a DNS at $Re = 1883$ is shown in Fig. 3.19. The initial condition used was close to lower-branch LC2. The figure shows exponential growth in S while the trajectory is near LC2. For $Re > \mathrm{Re}_{\mathrm{NS2}}$, lower-branch LC2 in the subspace has

two unstable directions, and we were not able to continue it very far using EST. However, it is a reasonable conjecture that it continues until it meets BS at H_2, given the similarities in the spatio-temporal structure of lower- and upper-branch LC2 and the eigenfunction that bifurcates at H_2 (see next subsection for supporting arguments).

- QPs — for $Re \in (\mathrm{Re}_{\mathrm{NS2}}, \mathrm{Re}_{\mathrm{NS1}})$ there is a symmetric quasiperiodic state that is a mixed mode of LC1 and LC2. It was found using EST using certain combinations of BS and LC2 as initial conditions in the symmetric subspace. As is typical of quasiperiodic mixed modes, it is spawned at a Neimark–Sacker bifurcation of one limit cycle (NS_2 on lower-branch LC2) and terminates at another Neimark–Sacker bifurcation of the other limit cycle (NS_1 on upper-branch LC1). QPs in the subspace has one unstable direction. DNS in the full space using QPs as initial conditions show that it also has an unstable direction out of the subspace. This indicates that a pitchfork bifurcation of QPs would spawn a pair of symmetry-related mixed modes in the full space, QPa. QPa would have (at least) two unstable directions. We have seen glimpses of QPa, for example at $Re = 1980$ (see Fig. 3.7) and $Re = 2000$ (see Fig. 3.8).

3.4.7 Connection between LC2 and H_2

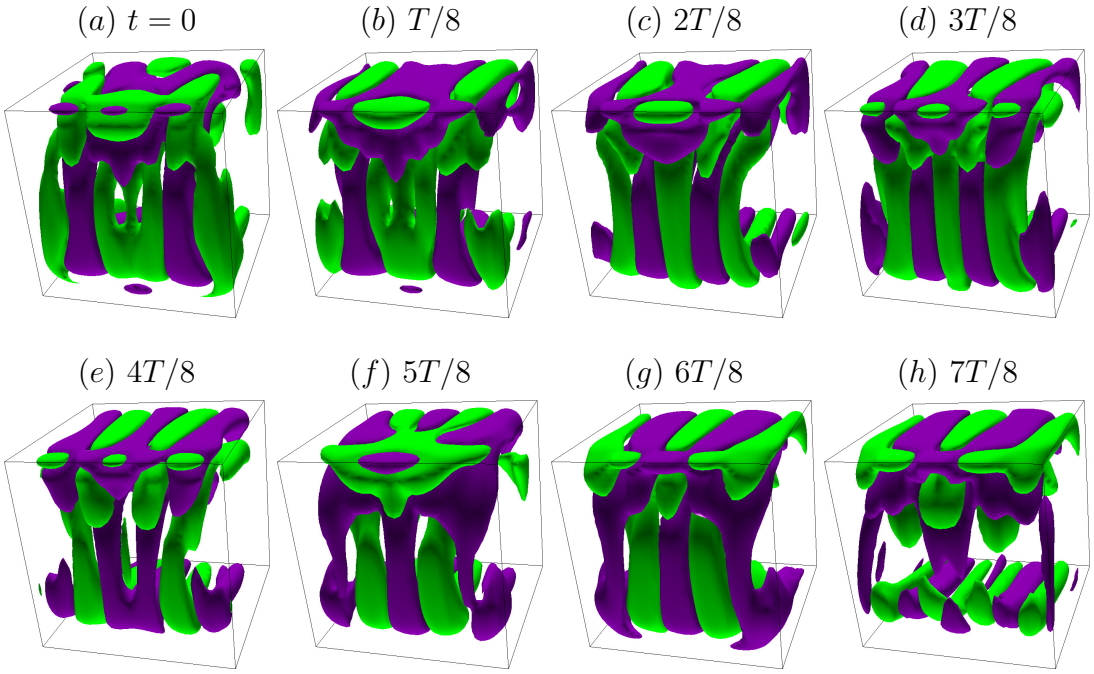

Figure 3.21: Isosurfaces of $v - \langle v \rangle$ at ± 30 at $Re = 2090$ (green is negative and purple is positive). See Supplemental Material Lopez *et al.* [55] for an animation.

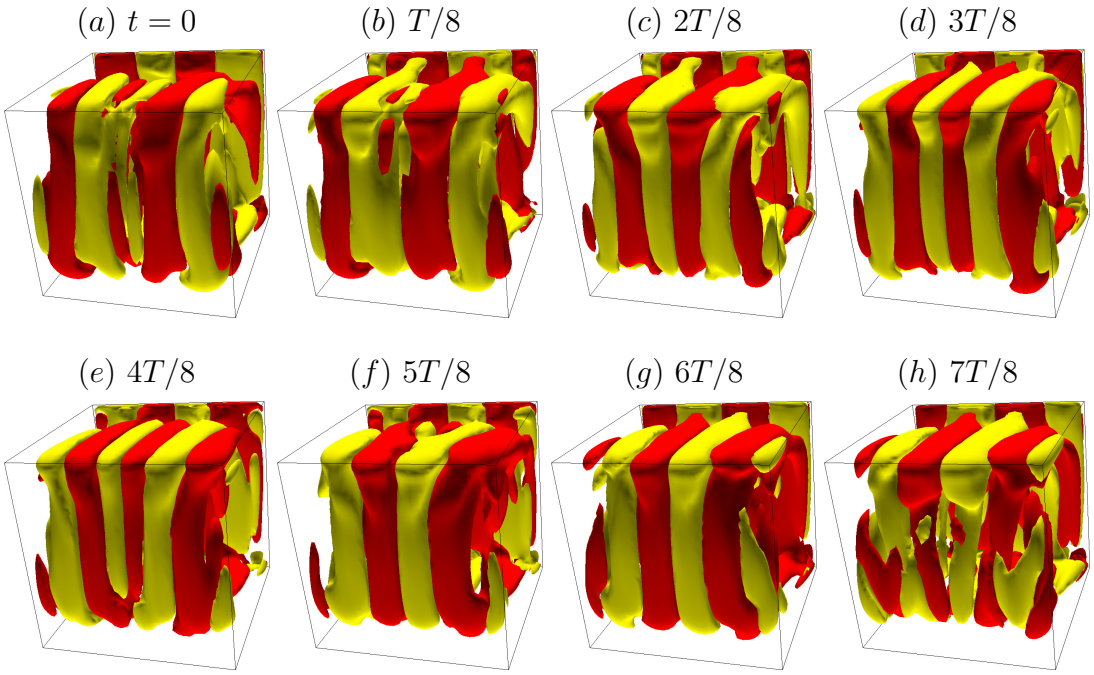

Figure 3.22: Isosurfaces of $H - \langle H \rangle$ at $\pm 10^5$ at $Re = 2090$ (yellow is negative and red is positive). See Supplemental Material Lopez *et al.* [56] for an animation.

The picture summarized in the previous subsection is fairly complete albeit missing some pieces, specifically the possible connection between the lower-branch LC2 and the second Hopf bifurcation H_2. As already noted by Loiseau [43], Loiseau *et al.* [44] and confirmed by our own analysis in § 3.4.3, the Hopf frequency is very close to the oscillation frequency of LC2, suggesting that LC2 is the limit cycle that bifurcates from BS at H_2. To further support this conjecture, we compare the spatio-temporal structure of LC2 with that of the eigenfunction corresponding to λ_2. Figure 3.20 shows the spatio-temporal dynamics of the y-component of the real part of the rotated eigenmode $\mathbf{\Phi_2}$ associated to $\lambda_2 = \rho + i\omega$,

$$\mathbf{\Phi}(x, y, z, t) = Re(\mathbf{\Phi_2}) \cos(\omega t) + Im(\mathbf{\Phi_2}) \sin(\omega t). \tag{3.8}$$

The resulting cycle consists of waves coming in symmetrically from lateral walls meeting at the midplane. For comparison purposes, isosurface of $v - \langle v \rangle$ of upper-branch LC2 at $Re = 2090$ is shown in Fig. 3.21 and exhibits the same type of spatio-temporal behavior. The comparison is even clear from the two corresponding online movies Lopez *et al.* [54, 55]. Figure. 3.22 shows the isosurfaces of $H - \langle H \rangle$ of upper-branch LC2 at $Re = 2090$, which are very similar to those at $Re = 1930$ shown in Fig. 3.5 and the accompanying online movies.

3.5 Discussion and Conclusions

Symmetries and symmetry-breaking bifurcations play an important role in canonical flows, often leading to spatio-temporal chaos in the neighborhood of primary instabilities, and may be intricately involved in the transition to turbulence. The lid-driven cavity is one such canonical flow, and recent explorations of the onset of unsteadiness in the cubic cavity have revealed that it comes in the form of bursts at irregular time intervals. With careful consideration of the symmetries of the problem and comparing the flows in the full space and in the symmetric subspace, we have shown that the bursts are excursions away from and back toward the symmetric subspace. These excursions are trajectories in phase space shadowing the stable and unstable manifolds of several saddle states that result following two successive Hopf bifurcations of the basic state as the Reynolds number is increased. Similar complicated dynamics associated with symmetry-breaking bifurcations in a very small neighborhood of parameter space, resulting in slow drifts from one saddle state to another, have been studied in other canonical flows, such as small aspect-ratio Taylor–Couette flow Lopez and Marques [45, 46], Abshagen *et al.* [1], Marques and Lopez [64], Abshagen *et al.* [2] and precessing cylinder flow Marques and Lopez [65], Lopez and Marques [49].

Our simulations, both in the full space and in the symmetric subspace, strongly indicate that the onset of unsteadiness in the cubic lid-driven cavity is organized by two successive subcritical Hopf bifurcations of the base state. The two Re at which these occur differ by about 8%. This can lead to the type of intermittency that has been reported; the other ingredient needed in order to rationalize the observation is the breaking of the spanwise reflection symmetry. The subcritical nature of the first Hopf bifurcation along with the symmetry breaking results in all steady, periodic, and quasi-periodic states being unstable local saddle states with a very small number of unstable manifolds in the full space for Re beyond the first bifurcation of the basic state. The lack of any local attractors often leads to intermittent chaotic behavior, with chaotic bursts resulting from repeated divergence away from the (weakly) repelling steady, periodic, or quasi periodic states, alternating with nearly-periodic phases as the trajectory is re-injected into the vicinity of the weakly unstable local states. However, in the symmetric subspace LC2 is stable, and the intermittent bursting is not present.

ACKNOWLEDGMENTS

This work was partially supported by National Science Foundation grant CBET-1336410. The computations were performed on the Saguaro Cluster of ASU Research Computing and School of Mathematical and Statistical Sciences computing facilities.

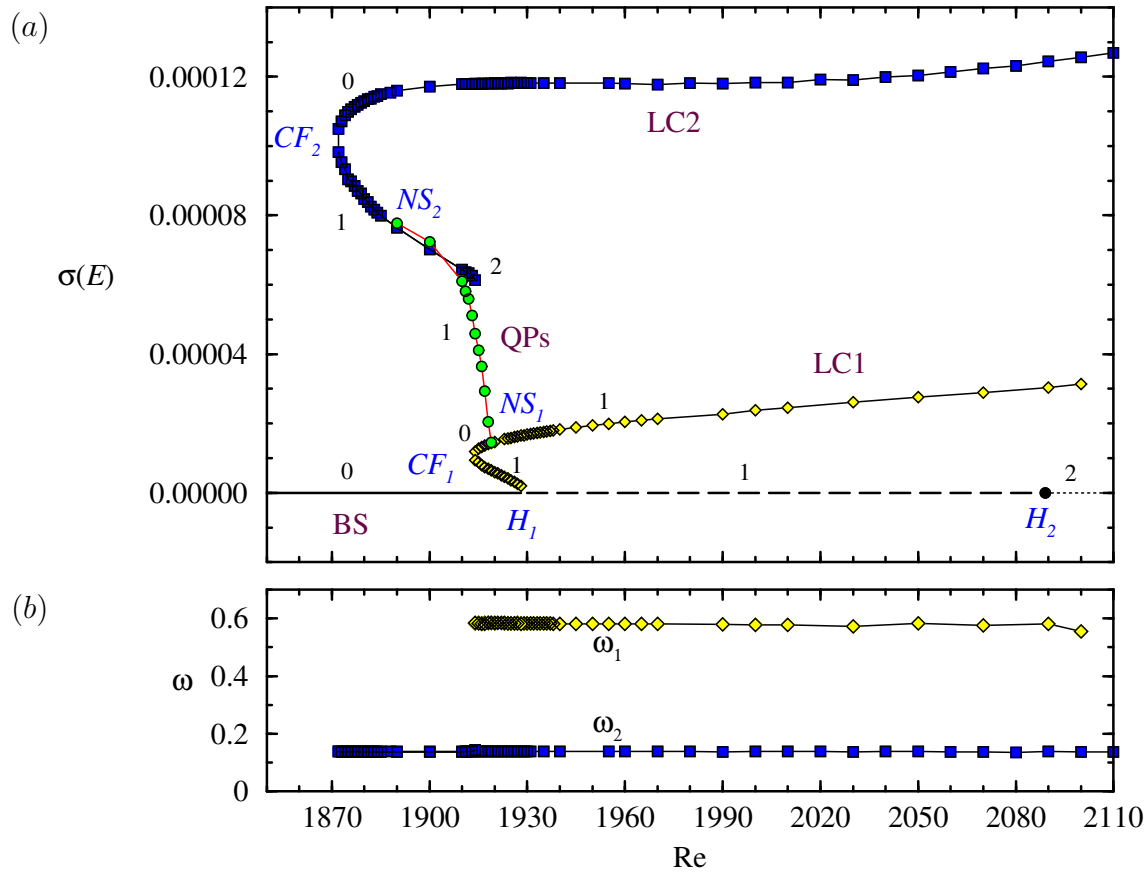

Figure 3.18: Variation with Re of (a) the oscillation amplitudes, $\sigma(E)$, of the various states as indicated, with integer indicating the number of unstable directions associated with each state (unstable states were found by restriction to the symmetry subspace, SFD or EST), and (b) the frequencies ω_1 and ω_2 of LC1 (diamonds) and LC2 (squares). Note that the frequencies of the upper and lower branches of each are virtually the same. The critical Re for the various bifurcations indicated are listed in Table 3.1.

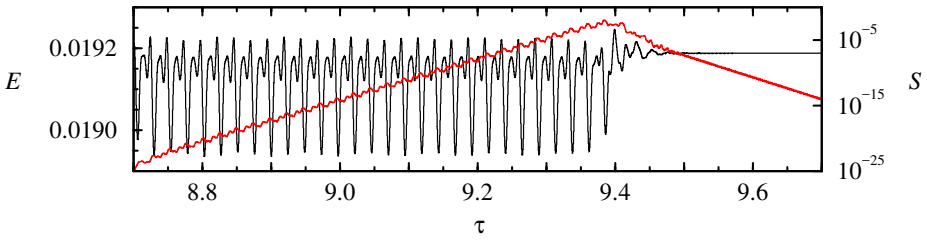

Figure 3.19: Time series of E (black) and S (red) starting from the EST-determined lower-branch LC2 (using αBS + $(1-\alpha)$(LC2 upper) as the initial condition, with $\alpha = 0.39042645730$), but evolving in the full space, at $Re = 1883$.

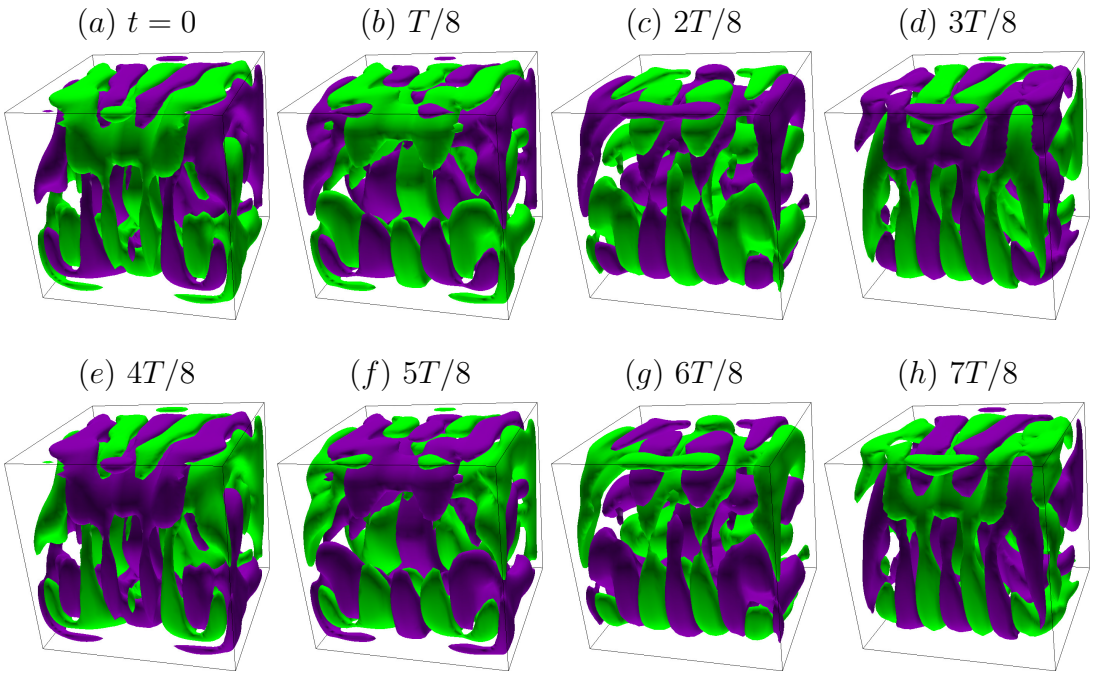

Figure 3.20: Isosurfaces of the y component of $\mathbf{\Phi}$ at $Re = 2090$. The isosurfaces (green is positive and purple is negative) are at $\pm 15\%$ of the maximum over one period. See Supplemental Material Lopez *et al.* [54] for an animation.

Chapter 4

COMPLEX DYNAMICS IN A STRATIFIED LID-DRIVEN CAVITY FLOW

4.1 Abstract

The dynamic response to shear of a fluid-filled square cavity with stable temperature stratification is investigated numerically. The shear is imposed by the constant translation of the top lid, and is quantified by the associated Reynolds number. The stratification, quantified by a Richardson number, is imposed by maintaining the temperature of the top lid at a higher constant temperature than that of the bottom, and the sidewalls are insulating. The Navier–Stokes equations under the Boussinesq approximation are solved, using a pseudospectral approximation, over a wide range of Reynolds and Richardson numbers. Particular attention is paid to the dynamical mechanisms associated with the onset of instability of steady state solutions, and to the complex and rich dynamics occurring beyond.

4.2 Introduction

The processes by which shear at the surface of a stably stratified body of fluid mixes and deepens the upper portions of the fluid body play an important role in the dynamics of many situations of interest, such as in lakes and oceans as well as in many industrial flows Turner [87], Fernando [20], Stevens and Imberger [83], Ivey *et al.* [29]. In general, mixing and turbulence tend to be suppressed when the fluid is sufficiently stably stratified, however when shear stress and buoyancy stratification are roughly in balance, the resultant dynamics can be quite complicated Sherman *et al.* [82], Majda and Shefter [61], Peltier and Caulfield [73].

The situation where an unsteady well-mixed region is separated from a stably stratified region is a common occurrence in many geophysical and astrophysical settings, and there continues to be intense interest in these flows, particularly in regards to the mechanisms by which energy and possibly momentum from the well-mixed region can be transported deep into the stratified region. Internal wave beams are a leading candidate and it is of much interest to understand how these are generated Michaelian *et al.* [68], Dohan and Sutherland [18], Pham *et al.* [75], Ansong and Sutherland [5], Munroe and Sutherland [69].

Our understanding of the processes involved is still quite limited. A useful analogue problem that is relatively straightforward to produce as a laboratory experiment and to simulate numerically is the lid-driven stratified cavity flow. Many studies exist in cavities with various aspect ratios or shapes, driven at one or more walls, with temperature gradient either in the direction opposite to gravity (stable stratification), or the perpendicular direction (horizontal convection), or in the same direction (Rayleigh–Bénard convection), in various media (air, water, oils, with different Prandtl numbers Pr), or in the presence of internal obstacles or fins. However, relatively few studies have explored the flow behaviour over a comprehensive range of the Reynolds and Richardson numbers, Re and Ri, characterising the shear and buoyancy of the flow regime. Such a comprehensive study is the goal of the present numerical investigation.

Most studies of the stably stratified configuration used here (where side walls are insulated and the top and bottom walls are kept at fixed temperatures) have been limited to relatively low Grashof numbers, $Gr = Ri\,Re^2 \lesssim \mathcal{O}(10^6)$, normally associated (for moderate Pr) with steady state responses Iwatsu *et al.* [30], Nicolás and Bermúdez [70], Cheng and Liu [14], in some cases as part of a more general investigation of doubly-diffusive (temperature and solute) systems Maiti *et al.* [59]. The

experimental study of Koseff and Street [36] in a three-dimensional cavity with aspect ratio 1:3:1 (square vertical cross-section) filled with water ($Pr \approx 7$) remains the quintessential reference for flows at large $Gr \sim \mathcal{O}(10^7 - 10^8)$. Their visualisations in the (vertical) symmetry plane provide some general understanding of the competition between shear and buoyancy forces in regimes where the flows are expected to be unsteady, but they only present transient dynamics (the longest experiment corresponds to $t \approx 0.3$ viscous time). Ji *et al.* [31] provide experimental and numerical evidence of oscillatory behaviour at large Re and moderate Ri in air ($Pr \approx 0.7$), but they only report on the vertical temperature distribution. Blanchette *et al.* [9] used salt stratification ($Pr \approx 600$) to investigate the relationship between the Péclet number $Pe = Re\,Pr$ and the Rayleigh number $Ra = Gr\,Pr$ at the onset of instability of the steady flow at large Ri (with $Gr \sim \mathcal{O}(10^{10} - 10^{12})$). Cohen *et al.* [15] investigated stably stratified air flow in experiments in a three-dimensional lid-driven cavity in the large Re and small Ri regime, presenting mean flow features and statistics of the turbulent flow. Consistent with the previous studies, they observed the buoyant confinement of the lid-driven roller to the upper downstream corner. They also presented some scaling analysis of the unsteady flow, but gave few details of the unsteadiness or how it comes about. They suggested that three-dimensional effects are secondary, and this motives us to do a detailed numerical investigation of the onset and the dynamics of the unsteady flow. Our results in the two-dimensional square cavity in the low-Re regime ($Re \lesssim 1000$) confirm previous results and observations of steady state solutions and validate our numerical approach. A detailed study of the instability of the steady state as Re is increased is carried out over a large range in Ri. Details of the bifurcating unsteady states are analysed using a bifurcation theoretic approach and frequency analyses of flow kinetic energy, revealing an intricate pattern of responses due to competition between buoyancy and inertial effects.

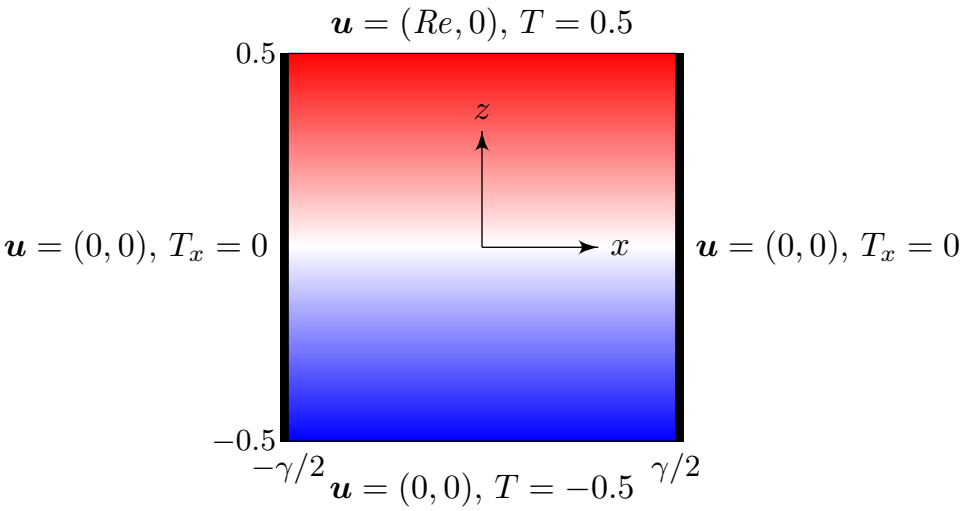

Figure 4.1: Schematic of the system, indicating the non-dimensional coordinate system and boundary conditions. The top boundary moves to the right (positive x direction) at constant speed Re. The colour map shows the linearly stratified temperature distribution (red is $T = 0.5$, blue is $T = -0.5$, and white is $T = 0$) when $Re = 0$.

4.3 Governing Equations and Time Scales

4.3.1 Governing Equations and Boundary Conditions

Consider the flow in a rectangular cavity of depth d and width l, filled with a fluid of kinematic viscosity ν, thermal diffusivity κ, and coefficient of volume expansion β. The top boundary of the cavity is driven horizontally at a constant speed U and is maintained at a fixed temperature T_{top}. The bottom boundary is maintained at a cooler fixed temperature T_{bot}, whilst the two sidewalls are insulated. Gravity g acts in the downward vertical direction. We consider the two-dimensional problem here as it allows for an extensive parameter study. This is also in part motivated by the observation that the dominant modes of linearized instability for stratified shear flows are two-dimensional Majda and Shefter [60]. The temperature deviation from the mean temperature, $(T_{\text{top}} + T_{\text{bot}})/2$, is non-dimensionalized with $\Delta T = T_{\text{top}} - T_{\text{bot}}$.

Figure 4.1 shows a schematic of the system. Using d as the length scale and the viscous time d^2/ν as the time scale, the non-dimensional governing equations, employing the Boussinesq approximation, are

$$\begin{aligned} &\boldsymbol{u}_t + \boldsymbol{u}\cdot\nabla\boldsymbol{u} = -\nabla p + \nabla^2\boldsymbol{u} + Gr\,T\boldsymbol{e}_z\,, \quad \nabla\cdot\boldsymbol{u} = 0\,, \\ &T_t + \boldsymbol{u}\cdot\nabla T = \frac{1}{Pr}\nabla^2 T\,. \end{aligned} \tag{4.1}$$

The boundary conditions are:

$$\begin{aligned} &\text{top, } (x,z) = (x, 0.5): && (u,w,T) = (Re, 0, 0.5), \\ &\text{bottom, } (x,z) = (x, -0.5): && (u,w,T) = (0, 0, -0.5), \\ &\text{sides, } (x,z) = (\pm 0.5\gamma, z): && (u,w,T_x) = (0,0,0), \end{aligned} \tag{4.2}$$

where $\gamma = l/d$ is the aspect ratio.

4.3.2 Time Scales

There are four time scales of relevance; these are

$$\begin{aligned} &\text{viscous time} && \tau_\nu = d^2/\nu, \\ &\text{thermal diffusion time} && \tau_\kappa = d^2/\kappa, \\ &\text{inertial time} && \tau_i = d/U, \\ &\text{buoyancy time} && \tau_b = \sqrt{d/g\beta\Delta T}. \end{aligned} \tag{4.3}$$

The governing parameters can be expressed as ratios of these time scales:

$$\begin{aligned} &\text{Prandtl number} && Pr = \tau_\kappa/\tau_\nu = \nu/\kappa, \\ &\text{Reynolds number} && Re = \tau_\nu/\tau_i = Ud/\nu, \\ &\text{Richardson number} && Ri = (\tau_i/\tau_b)^2 = g\beta\Delta T d/U^2, \\ &\text{Grashof number} && Gr = (\tau_\nu/\tau_b)^2 = RiRe^2 = \beta g d^3\Delta T/\nu^2. \end{aligned} \tag{4.4}$$

In this study $\gamma = 1$ and $Pr = 1$ are kept fixed, and we consider variations in the independent parameters Re and Ri.

The boundary condition for the x-velocity at the moving top wall, $u(x, 0.5) = Re$, is discontinuous where it meets the two vertical sidewalls, which can lead to Gibbs phenomena when using a global spectral method. In order to resolve this numerical issue, we regularise the top wall boundary condition by using:

$$u(x, 0.5) = Re \left[1 - \exp\left(-(1 - 4x^2)/\delta\right)\right]. \tag{4.5}$$

The small positive number δ controls the distance over which the discontinuity is regularised. For the results presented here, we have used $\delta = 0.03$. Smaller values of δ, corresponding to narrower gaps between the top lid and the vertical sides, lead to qualitatively similar results while significantly increasing the computational demand. For the smaller Re and Ri values considered, a collocation grid with $M = 128$ points in each direction provides sufficiently many points in the regularisation regions near the top corners to yield reliable results. For larger Re and Ri, finer grids were used, with $M = 196$ being used for the largest Re and Ri in order to resolve the flows.

4.3.3 Measurement

Depending on the values of Re and Ri, one or multiple solutions can be obtained from different initial conditions, such as steady state (S), limit cycles (L), or quasi-periodic states (QP) which are mixed modes of limit cycles whose frequencies may or may not be commensurate, and in some parameter regimes even more temporally complicated states exist. In general, the initial condition used is the static linearly stratified state, i.e., $u = w = 0$ and $T = z$. Other solutions can be obtained via continuation using solutions from nearby parameter values as initial conditions. To determine the type of solution, we monitor two global indicators of the flow: the non-dimensional heat flux through the bottom wall of the cavity (Nusselt number)

$$Nu = \int_{x=-0.5}^{x=0.5} T_z(x, -0.5) dx\,, \tag{4.6}$$

and the total kinetic energy

$$E = \frac{1}{Re^2} \int_{z=-0.5}^{z=0.5} \int_{x=-0.5}^{x=0.5} (u^2 + w^2) dx dz \,. \tag{4.7}$$

In general, $Nu \geq 1$ (with $Nu = 1$ for the static state, which only exists at $Re = 0$), and $E < 1$. Note that for steady states, Nu also corresponds to the heat flux through the top boundary, whereas for unsteady states, the heat flux through the top and the bottom are not necessarily the same at any instant in time, but their long-time averages converge to the same value. Unsteady flows are characterised by their temporal frequencies, f, obtained from the power spectral density (PSD) of the time series (which is first trimmed, de-trended, and Blackman filtered) of the kinetic energy E. Since the flows are computed using the viscous time scale, the frequencies can vary widely with Re and Ri. In order to compare values of f over a large range of Re and Ri,

we use the scaled angular frequency

$$F = \frac{f}{\sqrt{Re^2 + Gr}} = \frac{f}{Re\sqrt{1 + Ri}}. \tag{4.8}$$

This scaling reduces the measure f in the viscous time scale to the measure F of the frequency in the inertial time scale when $Gr = 0$ with $Re \neq 0$ fixed (i.e., $Ri = 0$) and to the measure F in the buoyancy time scale when $Re = 0$ with $Gr \neq 0$ fixed (i.e., $Ri \to \infty$), thus providing a smooth transition between these time scales for intermediate Ri values. Plots of the PSDs obtained for fixed Re but different Ri are normalised using the global peak power to reflect relative signal strengths, with the colour scale ranging from white ($-50dB$, corresponding to 10^{-5} power) to black $0dB$, associated with unit peak power).

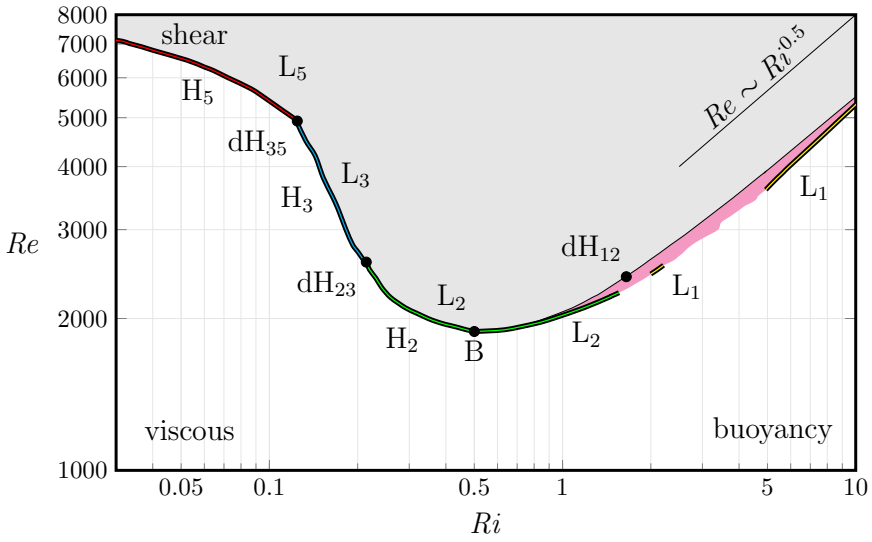

Figure 4.2: Phase diagram in the (Ri, Re) parameter space. Below the Hopf bifurcation curves, H_i with $i = 2$, 3 and 5, only the steady state S exists and is stable. Above the Hopf bifurcation curves, unsteady states including the limit cycles L_i with $i = 1$, 2, 3 and 5, exist in the grey shaded region. The dynamics in the magenta shaded region is hysteretic, with S and unsteady states attracting. Codimension-two points where two different Hopf bifurcation curves meet are indicated with bullets for the double-Hopf points dH_{35}, dH_{23} and dH_{12}, as well as the Bautin point B where the Hopf bifurcation H_2 changes from being supercritical to subcritical.

4.4 Results

Figure 4.2 provides a global overview of the regions in the (Ri, Re) parameter space where either the steady base state S is the only observed response (unshaded region), or sustained unsteady responses are observed (shaded regions). For fixed Ri, S is observed at low Re, for which viscous effects are dominant. At larger Re, competing shear and buoyancy effects destabilise S and lead to various time-dependent states. In the following subsections, we describe the bifurcations that result in these unsteady states and their nonlinear dynamics.

4.4.1 Steady State at Low Re Numbers

For small enough Re, the flow evolves to a steady state S for all values of Ri. Figure 4.3 show streamlines and temperature contours of S for $Ri = 0.05$, 0.5, and 5 at $Re = 1000$. The streamlines are the isocontours of the streamfunction ψ, where $(u, w) = (\psi_z, -\psi_x)$. The horizontal temperature gradient T_x, which is a source of vorticity, provides all the essential information on the dynamics of the flow and is also included in figure 4.3; it will be the main quantity of interest at higher Re values.

For $Ri \ll 0.5$, convective effects dominate over buoyancy effects, resulting in full vertical penetration of the lid-driven roller and temperature homogenisation throughout most of the cavity. This leads to a steep temperature gradient at the bottom of the cavity (see figure 4.3*a* for $Ri = 0.05$). The presence of two weak secondary recirculation zones at the bottom corners is consistent with the flow in the isothermal lid-driven cavity Koseff and Street [36], Iwatsu *et al.* [30], Nicolás and Bermúdez [70]. The impact of the non-isothermal conditions is that in the core of the main roller, the temperature is essentially uniformly hot and it is inside this roller where the streamfunction has non-zero gradients (i.e. there is a meridional circulation). The lid-driven roller is delineated by regions of large horizontal temperature gradients T_x separating the isothermal overturning flow in the roller from the temperature-stratified near-static fluid outside the roller.

For $Ri \approx 0.5$, buoyancy and convective effects are of comparable strength and their competition results in a smaller roller restricted toward the downstream top corner and a deeper stratification zone in the bottom of the cavity (see figure 4.3*b* for $Ri = 0.5$). Since advection brings the temperature at the top of the stratification zone in line with the temperature at the top of the cavity, the temperature gradient

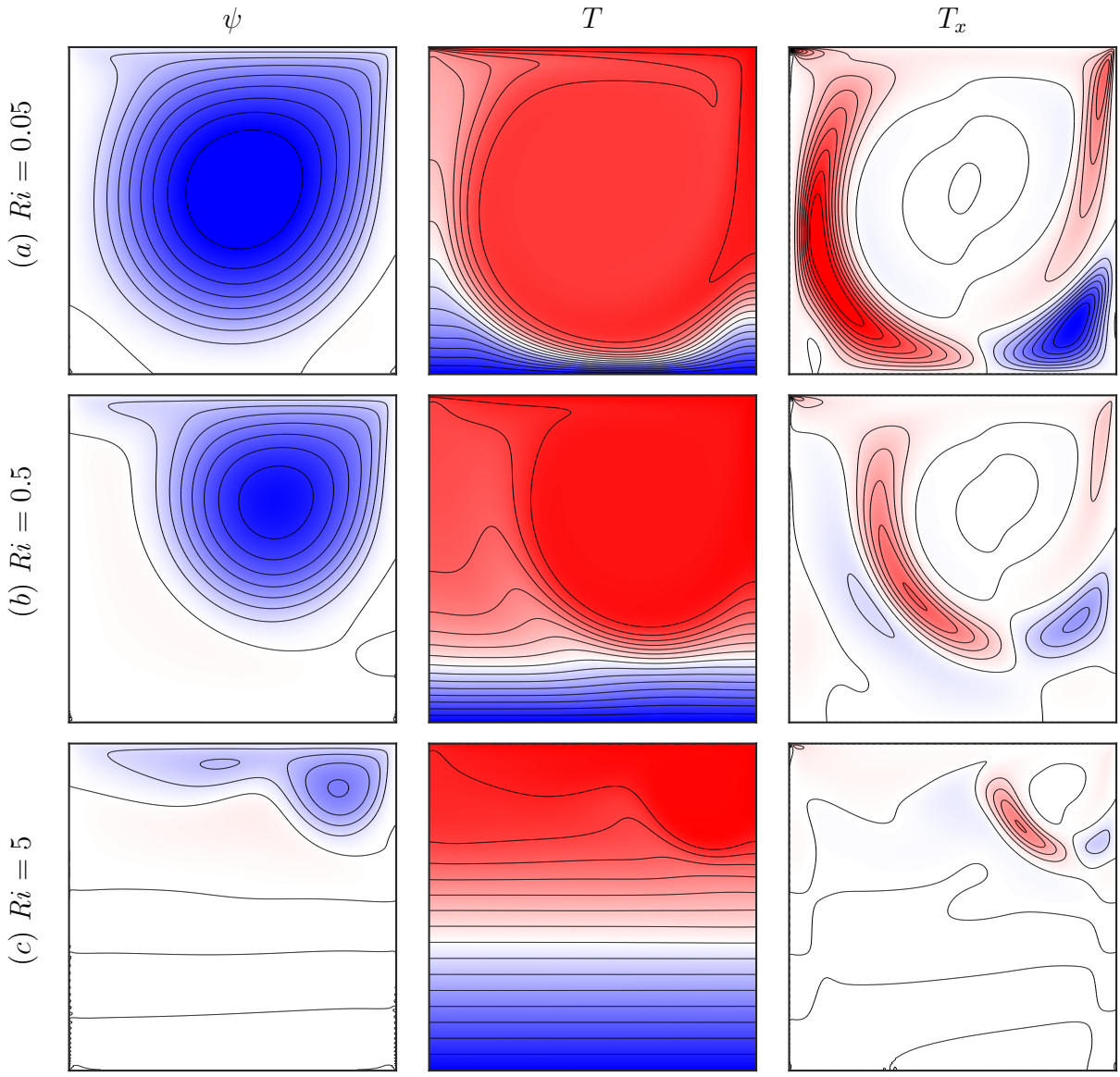

Figure 4.3: Streamlines ψ, isotherms T and horizontal temperature gradient T_x of S at $Re = 1000$ and Ri as indicated. The contour levels are equispaced in ranges $|\psi| \leq 100$, $|T| \leq 0.5$, and $|T_x| \leq 1.5$.

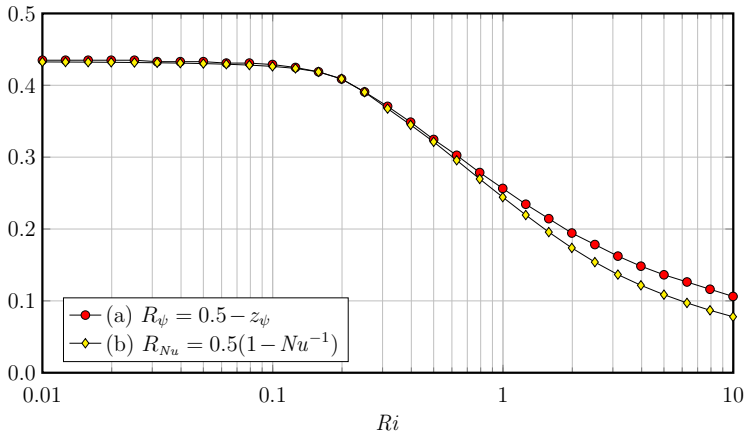

Figure 4.4: Radius of the primary roller as function of Ri at $Re = 1000$, estimated from (a) the vertical position z_ψ of the streamfunction minimum, and (b) the Nusselt number Nu.

through the bottom stratified region is lower than it is at smaller Ri. These features are consistent with the numerical results in Iwatsu *et al.* [30].

For $Ri \gg 0.5$, buoyancy confines the convective roller to the upper right corner of the cavity, and the flow is essentially unable to penetrate into the stratified zone. The streamlines indicate a number of very weak recirculation cells in the stratified zone. In the example shown in figure 4.3(c) for $Ri = 5$, there are four such secondary cells. For different Re and Ri, different numbers of similar secondary cells have been reported Koseff and Street [36], Nicolás and Bermúdez [70].

The radius of the lid-driven roller can be estimated from the vertical position z_ψ of the minimum of the streamfunction ψ, by assuming a perfectly circular roller, namely $R_\psi \approx 0.5 - z_\psi$. Alternately, the radius can be estimated from $Nu \approx 1/(1 - 2R_{Nu})$ by assuming a constant vertical temperature gradient below a roller of radius R_{Nu} and a uniform temperature within the roller. These assumptions are supported by figure 4.3(b). The two estimates of the radius, R_ψ and R_{Nu}, are shown in figure 4.4 for $Re = 1000$ and $Ri \in [0.01, 10]$. The two roller radii estimates are similar, especially

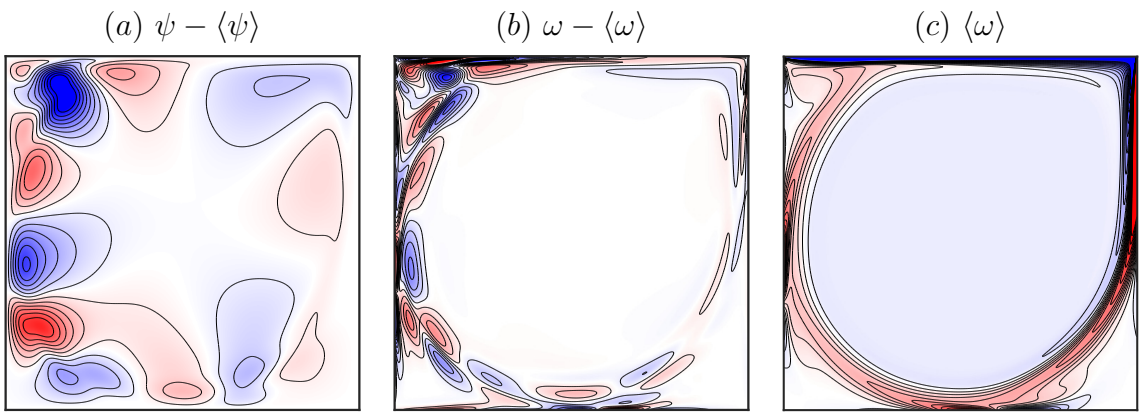

Figure 4.5: Snapshots of the deviations from the time averages of (a) the streamfunction and (b) vorticity, and (c) the time-averaged vorticity, for the limit cycle L_5 at $Re = 8016$ add $Ri = 0$.

for $Ri \lesssim 0.5$. Both estimates decrease with increasing Ri for $Ri \gtrsim 0.2$, with the roller depth $2R_\psi$ or $2R_{Nu}$ being about two thirds the depth of the cavity at $Ri = 0.5$, and one-half at $Ri = 1$. These results are also qualitatively similar to those measured experimentally by Cohen *et al.* [15, figure 6].

4.4.2 Instability of S for $Ri < 0.5$: Supercritical Hopf Bifurcations

For $Ri < 0.5$, the steady state S loses stability as Re is increased beyond a critical value via supercritical Hopf bifurcations, resulting in time periodic flows. At $Ri = 0$, oscillations appear at the critical $Re \approx 8016$ (using a 128×128 Chebyshev grid), which compares well with values in Brezillon *et al.* [13, table 3] obtained using various different numerical approaches and top-corner velocity regularisations. Figure 4.5 shows snapshots of the deviations from the time averages of the streamfunction and the vorticity, $\psi - \langle\psi\rangle$ and $\omega - \langle\omega\rangle$, as well as the time-averaged vorticity, $\langle\omega\rangle$. The deviation from the mean streamfunction is comprised of 5 negative cells interlaced with 5 positive cells which propagate around the periphery of the roller in the clock-

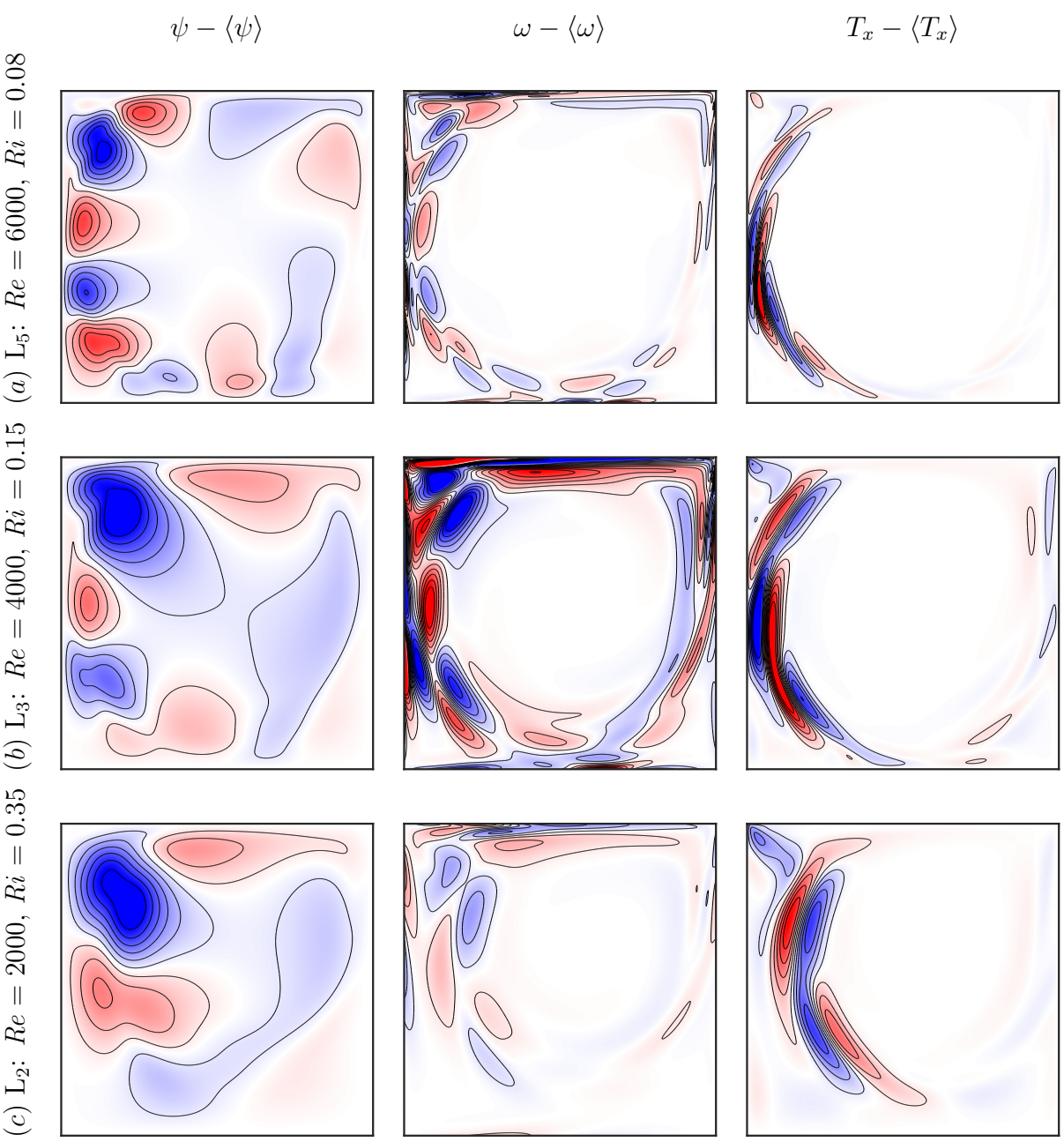

Figure 4.6: Snapshots of deviations from their time averages for streamfunction, vorticity, and horizontal temperature gradient, for the limit cycles at parameter points (Re, Ri) as indicated. The online Wu *et al.* [91], shows animations of each limit cycle over one period.

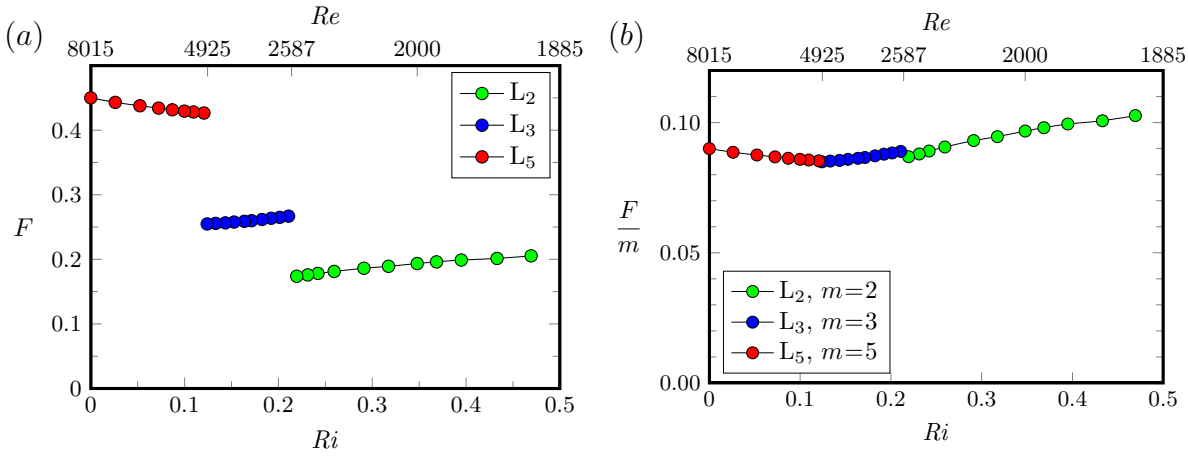

Figure 4.7: (a) Scaled frequencies F of the limit cycles L_2, L_3 and L_5 at Ri and Re slightly beyond the supercritical Hopf bifurcations shown in figure 4.2, and (b) the corresponding scaled frequencies F/m.

wise direction. This $m = 5$ cycle is denoted L_5. The structure of L_5 is similar to that of the real and imaginary parts of the critical Hopf eigenmode reported in Brezillon *et al.* [13, figure 8], Poliashenko and Aidun [76, figure 2], Fortin *et al.* [21, figure 5] and Auteri *et al.* [6, figure 14]. The scaled angular frequency of L_5 is $F \approx 0.45$, which matches the frequency values reported in Brezillon *et al.* [13, table 3]. This frequency corresponds to the rate at which a cell replaces the next cell of the same sign. Consequently, $F/m \approx 0.09$ is the fundamental frequency associated with a complete rotation of a given cell around the roller.

As Ri increases from 0, the critical Re decreases. The curve in (Ri, Re)-space along which S loses stability is made up of three distinct Hopf bifurcation curves H_m, with $m = 5$, 3 and 2 associated with three different limit cycles L_m. Figure 4.6 illustrates the streamfunction, vorticity, and horizontal temperature gradient deviations from their time averages for L_5, L_3 and L_2, computed at Re slightly above critical for $Ri = 0.08$, 0.15 and 0.35. Movies of the three limit cycles over one period are

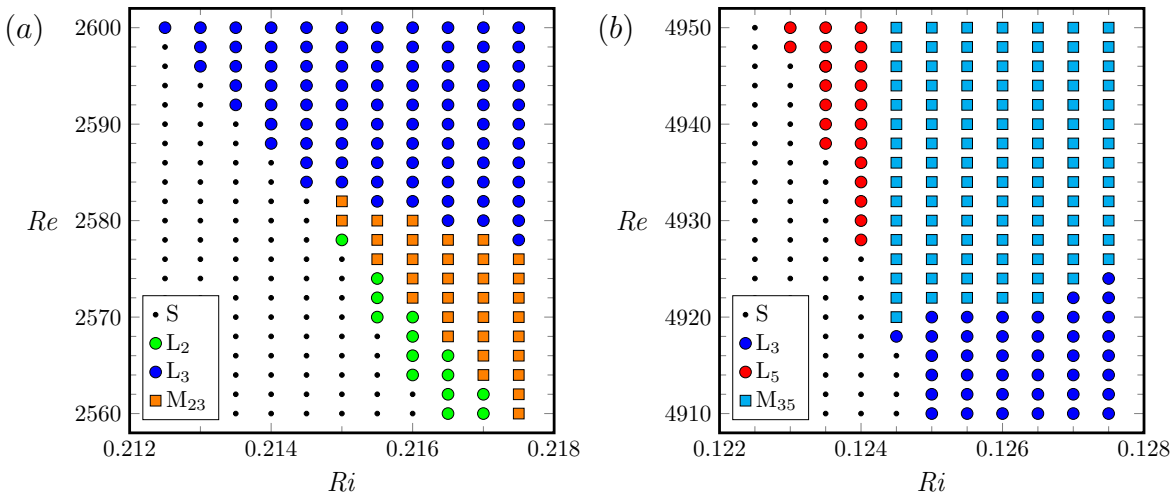

Figure 4.8: Stable States Observed via Continuation of the steady state by increasing Ri at fixed Re in the indicated parameter ranges. The presence of two stable limit cycle solutions and a stable (quasi-periodic) mixed state indicate the presence of two supercritical Hopf branches intersecting at double-Hopf points corresponding to (a) dH_{23} and (b) dH_{35}.

available online in Wu *et al.* [91]. The streamfunction deviations of L_m clearly show m pairs of interlacing negative and positive cells. The structure of L_5 at $Ri = 0.08$ is essentially the same as that of L_5 at $Ri = 0$ in figure 4.5. The cells thicken as their number $2m$ becomes smaller in different regions of (Ri, Re)-space. The frequencies of the limit cycles at the bifurcation are shown in figure 4.7. For smaller m, the larger cell size of L_m leads to a lower scaled angular frequency F, but the rotation number F/m exhibits little variation along the three Hopf bifurcation curves, and is almost continuous across modal transitions.

The Hopf curves intersect each other at double-Hopf bifurcation points. There are two of these for $Ri < 0.5$: dH_{23} at $(Ri, Re) \approx (0.214, 2587)$ and dH_{35} at $(Ri, Re) \approx (0.1245, 4925)$. Typically, in a neighbourhood of a double-Hopf point, a quasi-periodic mixed mode of the two limit cycles involved also exists, and in some cases the mixed modes is stable Kuznetsov [38]. This is the case here for the two double-Hopf bi-

furcations, as shown in figure 4.8. The mixed modes M_{23} and M_{35} are essentially superpositions of the limit cycles L_2 and L_3, and L_3 and L_5, respectively, and are stable in parameter regimes emerging from the double-Hopf points. In the regions where the mixed modes are stable, the limit cycles are not. The boundaries separating the parameter regions where the mixed mode is stable and the two regions where the limit cycles are stable are curves of Neimark–Sacker bifurcations. The slopes of these curves and of the Hopf bifurcations curves very close to the double-Hopf point provide estimates of the normal-form coefficients of the two double-Hopf bifurcations. From these, one can determine the nonlinear behaviour of the flow states. In the classification of Kuznetsov [38, §8.6], dH_{35} is simple type II, while the approximate alignment of the Hopf curve H_3 with a Neimark–Sacker curve prevents the distinction between simple type II or simple type III for dH_{23} Kuznetsov [38, figure 8.25]. Nevertheless, both simple type II and simple type III double-Hopf bifurcations are cases with the mixed mode being stable. The computation of the double-Hopf coefficients is in Appendix C.

4.4.3 Instability of S for $Ri > 0.5$: Subcritical Hopf Bifurcations

For $Ri \gtrsim 0.5$, the steady state S loses stability as Re increases via a subcritical Hopf bifurcation. The Bautin point B at which the Hopf bifurcation H_2 switches from being supercritical to subcritical is at $(Ri, Re) \approx (0.5, 1885)$. At this point a cyclic-fold (saddle-node bifurcation of limit cycles) bifurcation curve also emerges, along which the unstable limit cycle L_2 created at the subcritical H_2 bifurcation (the lower branch cycle) becomes stable (upper branch cycle) as it is folded back in parameter space Kuznetsov [38]. Both S and upper branch L_2 co-exist and are stable, and lower branch L_2 is unstable in the hysteresis region between the subcritical Hopf and cyclic-fold curves, the region shaded magenta in figure 4.2; also see the close-up version in

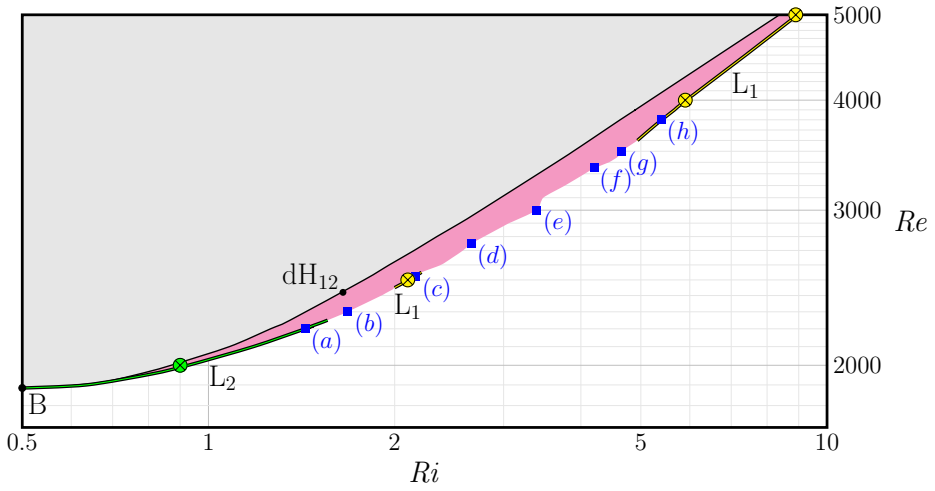

Figure 4.9: Close-up from figure 4.2 of the hysteresis region (shaded magenta) starting from the Bautin point B, between the subcritical Hopf curve where the steady state loses stability and the cyclic-fold curve. The $\otimes$ symbols indicate the locations in (Re, Ri) space where examples of limit cycles L_2 and L_1 are shown in figure 4.10 and figure 4.11. Time-series of E and phase-portraits of sample states at the edge of the hysteresis region indicated by the blue squares labelled $(a–h)$ are shown in figure 4.12.

figure 4.9 where the cyclic-fold curve of L_2 is drawn as a thick green curve on the high-Ri/low-Re edge of the hysteresis region. This cyclic-fold curve which starts at the Bautin point B ends at $(Ri, Re) \approx (1.56, 2250)$. Beyond this point, the upper branch state is a quasi-periodic state all the way to the edge of the hysteresis region. Then, at the edge of the hysteresis region at $(Ri, Re) \approx (2, 2450)$, the edge is once again a cyclic-fold bifurcation, but now involving a limit cycle L_1. The extent of this cyclic-fold curve is drawn as a thick yellow line in figure 4.9. The frequencies of L_1 and L_2 on the upper branches of the respective cyclic-fold bifurcations are very close to a 1:2 frequency ratio, and the spectral signature of the quasi-periodic state has all linear combinations of these two frequencies. This behaviour is indicative of an underlying double-Hopf bifurcation dH_{12}, where both Hopf bifurcations from

the steady state S are subcritical. This codimension-two point is estimated to be at $(Ri, Re) \approx (1.65, 2420)$, indicated in the phase diagram figure 4.2, as well as in figure 4.9. This type of double-Hopf bifurcation is strongly resonant and in its neighbourhood, homoclinic and heteroclinic dynamics and transverse intersections of stable and unstable manifolds are to be expected, leading to slow-fast dynamics and chaotic behaviour. This complex dynamics is associated with the phase of the limit cycles not decoupling from their amplitude, opening up the possibility for the phases of the two limit cycles to lock and unlock via heteroclinic bifurcations Knobloch and Proctor [35]. The cyclic-fold curve of L_1 is short, extending only to $(Ri, Re) \approx (2.2, 2550)$, beyond which the upper-branch states at the edge of the hysteresis region are quasi-periodic or more complex (some are described below). Further along the edge, from $(Ri, Re) \approx (5, 3600)$ to at least $(Ri, Re) \approx (9, 5000)$, the edge is once again demarcated by a cyclic-fold curve of L_1 (also drawn as a thick yellow line in figure 4.9).

Figure 4.10 and figure 4.11 shows shapshots of the streamfunction, vorticity and horizontal temperature gradient deviations from their time averages for the limit cycles L_1 and L_2 near the cyclic-fold bifurcation curves described above, at (Ri, Re) points indicated as $\otimes$ in figure 4.9. For L_2 at $(Ri, Re) = (0.9, 2000)$, the two cells of each sign in the streamfunction deviation (blue and red) are easily recognisable, and to a lesser extent in the vorticity and horizontal temperature gradient deviations. At this relatively small Ri, the lid-driven roller occupies most of the cavity. At larger Re and Ri, L_1 with a large single pair of cells in the streamfunction deviation is the state undergoing the cyclic-fold bifurcation. At these larger Ri, the roller is more confined to the downstream top corner region and the lower part of the cavity is nearly linearly stratified. The ratio of the L_1 frequency and the local buoyancy frequency in the lower part of the cavity is such that internal wave beams are emitted from the

oscillatory roller into the stratified region at an angle of approximately 45^{circ} such that they reflect back from lower left corner of the cavity. This retracing of the beam leads to enhanced phase coherence. The online Wu *et al.* [92] shows the four cases in figure 4.10 and figure 4.11, each animated over one period. In the movie, it is evident that, even for the L_2 case with the relatively small Ri, there is a hint of a wave beam also retracing off the lower left corner. The energy of the wave beams does not exceed a few percent of the total energy.

Between $(Ri, Re) \approx (2.2, 2550)$ and $(Ri, Re) \approx (5, 3600)$, the last state observed on the upper branch of the hysteresis region before falling back to the steady state as Ri is increased is a quasi-periodic QP state with strong L_1 content. A pure L_1 is also observed slightly below $(Ri, Re) \approx (5, 3600)$, suggesting a subcritical bifurcation along the fold between the QP and L_1 states.

Figure 4.12 illustrates specific responses obtained along the upper branch, at the last stable time-dependent state obtained when increasing Ri, labelled (a–h) in figure 4.9. The plots show the time series $E(t)$ over 0.25 viscous time units as well as phase portraits obtained by plotting $E(t)$ against a delayed $E(t - \tau)$. The delay τ was selected such that the associated frequency $F = 1/(\tau Re\sqrt{1 + Ri}) = 0.3$ is larger, but not excessively so, than the scaled frequency $F \approx 0.2$ of L_2. The responses (a) and (c) correspond to limit cycles L_2 and L_1 respectively. Limit cycle L_1 is also the response in (h), and its presence can be recognised in the quasi-periodic responses (e, f, g), with the low beat frequency and that of L_1 locked in a 1:18 ratio in case (e). Case (b) illustrates a locked mixed mode of L_1 and L_2 is a regime close to the double-Hopf point dH_{12}. This mixed mode seems to arise from a flip bifurcation of L_2 (Floquet multipler crossing the unit circle at -1) at a lower Ri (or Re). Response (d) exhibits near heteroclinic behaviour between limit cycles L_1 and L_2, with about equal power at both frequencies, again likely associated with the strongly resonant

double-Hopf bifurcation H_{12}. A plot of the (long) time average of the scaled kinetic energy $\langle E \rangle$ along the upper branch of the fold in figure 4.13 shows that the mixed mode in case (d) has slightly higher kinetic energy than its L_1 neighbours.

The scaling $Re \sim \sqrt{Ri}$ holds along the subcritical Hopf curve (black line in figure 4.2). This scaling can be justified near the onset of instability of the base steady state S at large Ri and Re by assuming a linear stratification, so that

$$\boldsymbol{u} = (u(z,t), w(x,t)), \quad p = p(x,t), \quad T_x = T_{zz} = 0. \tag{4.9}$$

In this case, the system (4.1) simplifies to

$$u_t + wu_z = -p_x + u_{zz}, \quad w_t + uw_x = w_{xx} + Gr\,T, \quad T_t + wT_z = T_{xx}/Pr. \tag{4.10}$$

In the steady case, this further reduces to

$$w_{xxxx} = uw_{xxx} - Gr\,T_{xx} = uw_{xxx} - r^4 w, \tag{4.11}$$

where $r^4 = T_z GrPr$. The existence of a similarity solution $w = w(rx)$ leads to the condition $u \sim r$, i.e. $Re \sim r \sim \sqrt[4]{Gr}$ using the entrainment condition $u = -Re$ at the top of the stratified region. Similar arguments for a related problem are made in Hanratty *et al.* [26], and in Blanchette *et al.* [9] who also present supporting physical experiments.

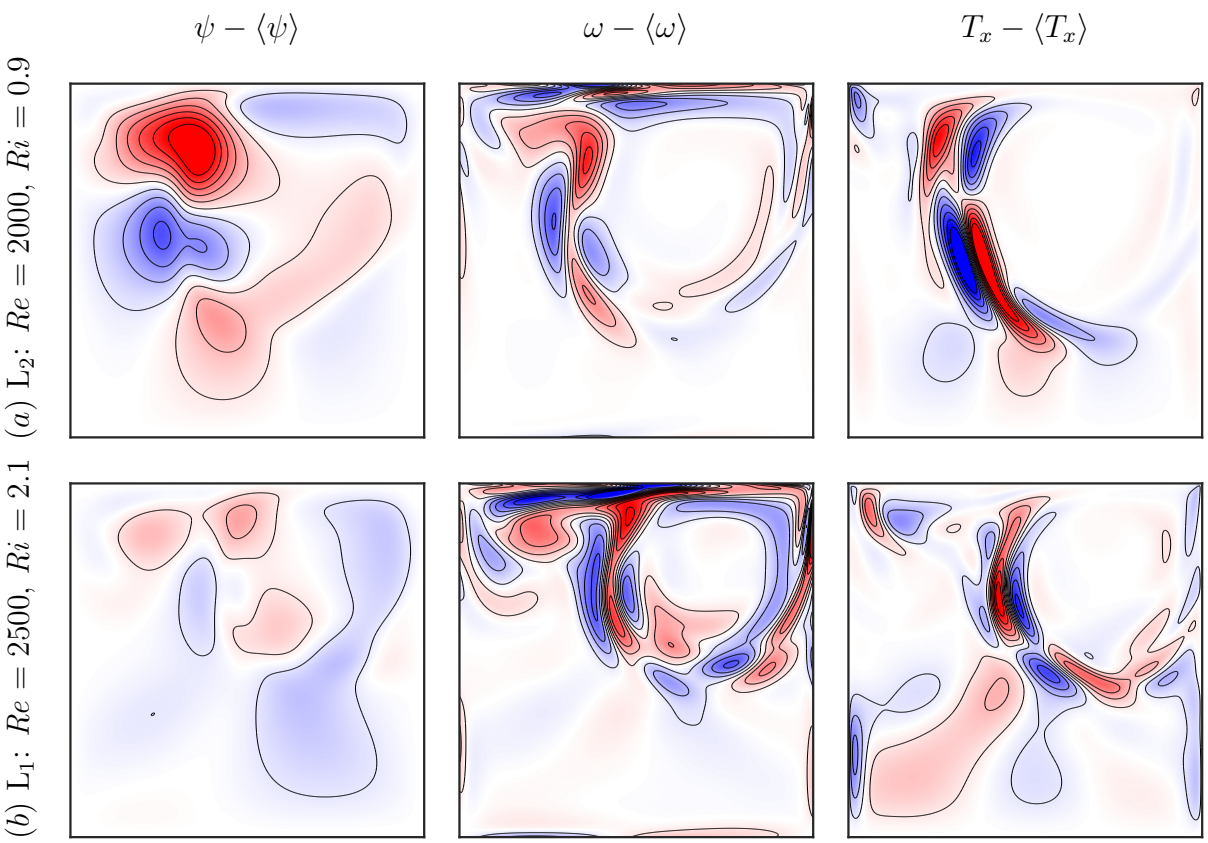

Figure 4.10: Snapshots of deviations from their time averages for streamfunction, vorticity, and horizontal temperature gradient, for the limit cycles at parameter points (Re, Ri) as indicated. The online Wu *et al.* [92], shows animations over one period.

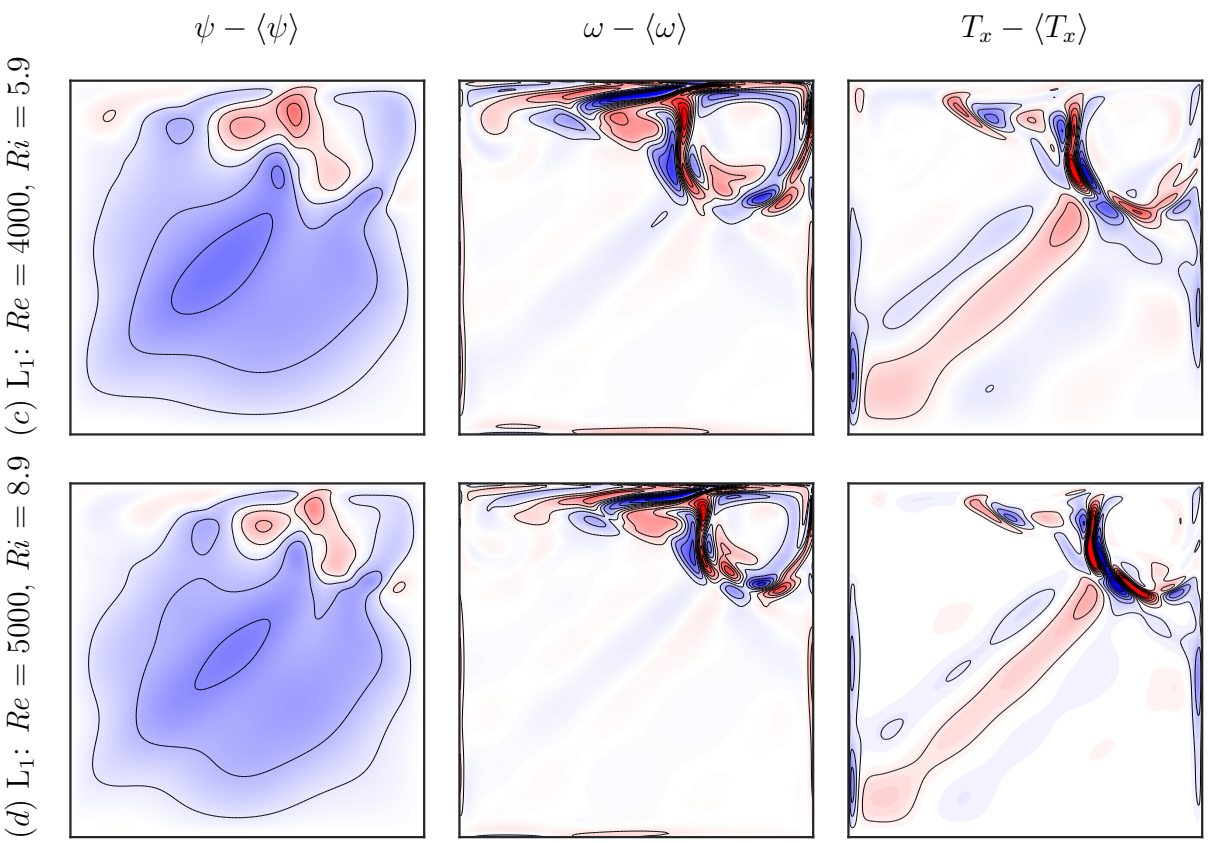

Figure 4.11: Snapshots of deviations from their time averages for streamfunction, vorticity, and horizontal temperature gradient, for the limit cycles at parameter points (Re, Ri) as indicated. The online Wu *et al.* [92], shows animations over one period.

In the time-dependent case, balancing the terms in (4.10) and assuming the solution to be periodic with angular frequency ω yields

$$\omega^2 w \sim w_{tt} \sim Gr\ T_t \sim Gr\ T_z w, \tag{4.12}$$

i.e. $\omega \sim \sqrt{Gr\ T_z}$. So, for large Ri,

$$F \sim \frac{\omega/2\pi}{Re\sqrt{Ri}} = \frac{\omega/2\pi}{\sqrt{Gr}} \sim \frac{\sqrt{T_z}}{2\pi} \sim \frac{1}{2\pi} \approx 0.159, \tag{4.13}$$

approaches a constant, further justifying the choice of the frequency scaling (4.8).

The data in figure 4.13 also suggests the scaling

$$\langle E \rangle \sim 1/\sqrt{Ri} \sim 1/Re \sim 1/\sqrt[4]{Gr}, \tag{4.14}$$

along the fold curves. There, the peak frequency f of the response scales like

$$f = F\ Re\sqrt{1+Ri} \sim Re\sqrt{Ri} \sim Ri, \tag{4.15}$$

resulting in $\langle E \rangle \sim 1/\sqrt{f}$.

The scaled frequency of L_1 along its fold above $(Ri, Re) \approx (5, 3600)$ was observed to marginally increase from $F \approx 0.115$ to $F \approx 0.118$ at $(Ri, Re) \approx (9, 5000)$. However, at $(Ri, Re) \approx (10.7, 5500)$ (corresponding to the rightmost upper data point in figure 4.13) the scaled frequency F of L_1 at its fold was found to be significantly higher, namely $F \approx 0.135$, which is much closer to the value predicted by (4.13).

4.4.4 Dynamics above the Neutral Curve

The flow response for selected Re values was computed for $Ri \in [0.1, 10]$ over at least four viscous times, and up to 15 viscous times for cases with low-frequency content. Responses associated with a coarse grid of logarithmically spaced Ri values were first obtained using zero velocity and a linear temperature profile as the initial

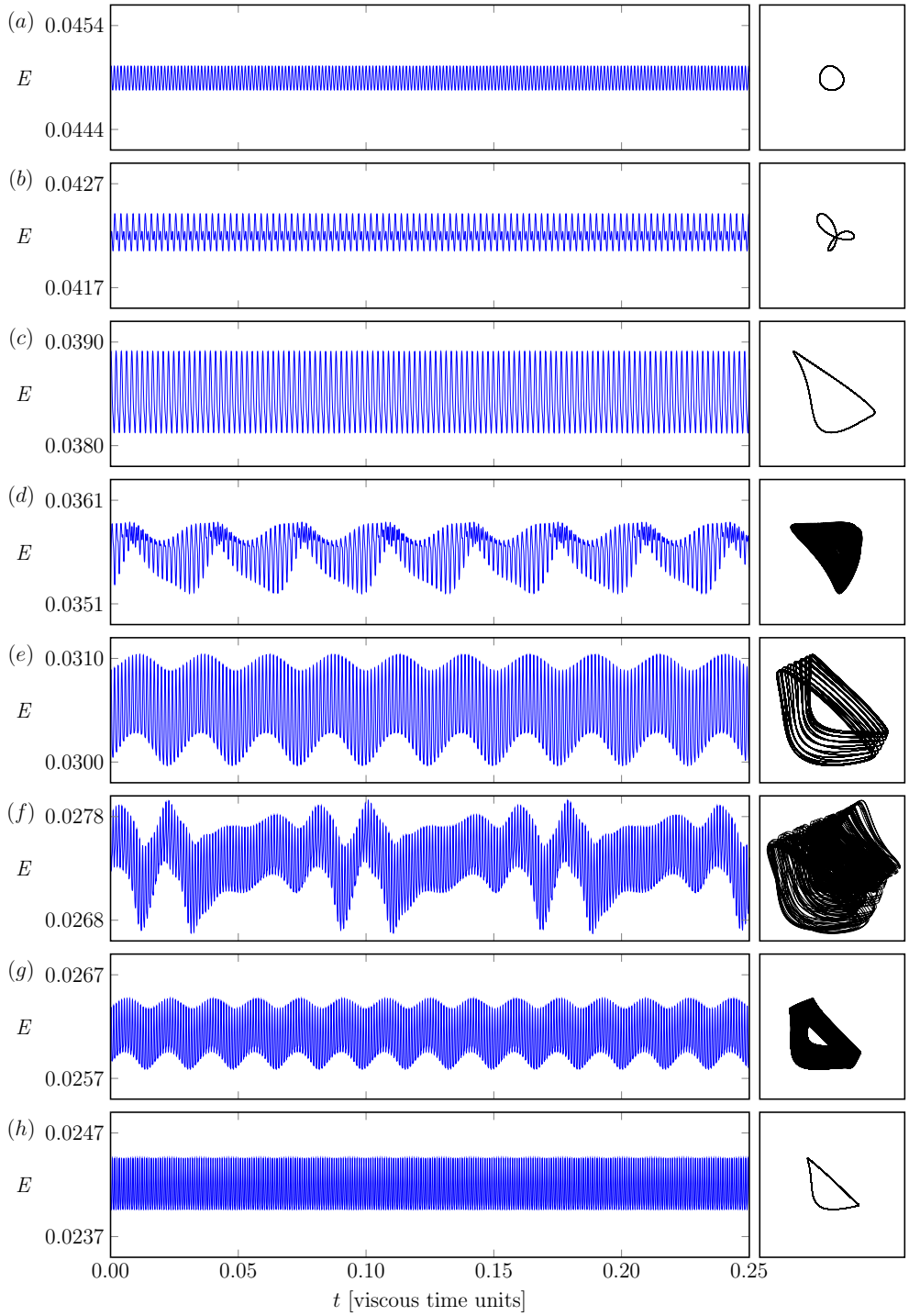

Figure 4.12: Time series of the E responses over a window of 0.25 viscous units, at the (Ri, Re) values indicated in figure 4.9 by the locations of the labels $(a–h)$, together with the corresponding phase portraits using $(E(t-\tau), E(t))$ with delay $\tau = 1/(0.3Re\sqrt{1+Ri})$.

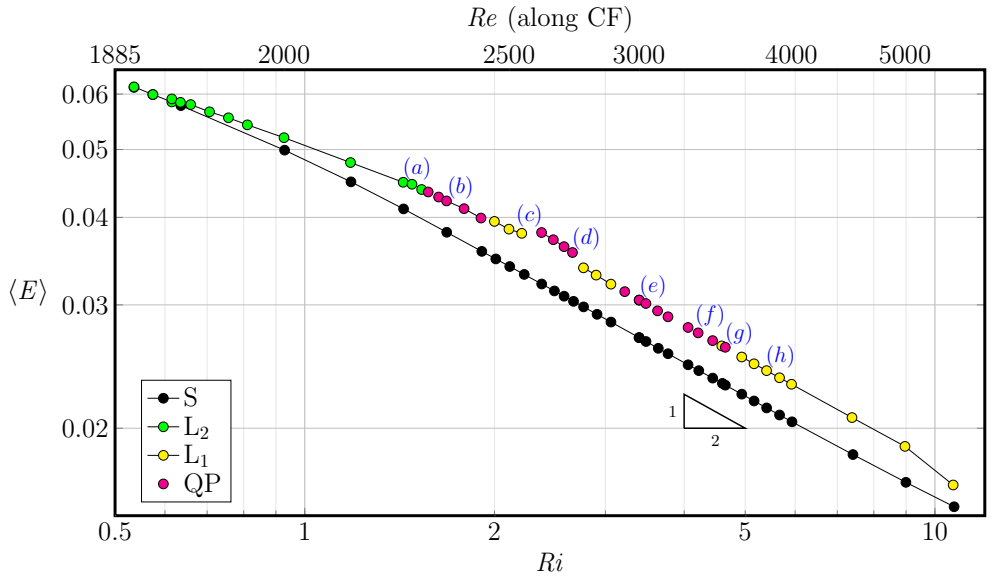

Figure 4.13: Scaled kinetic energy E of steady states and mean time scaled kinetic energy $\langle E \rangle$ of unsteady states along the cyclic fold upper branch as function of Ri. The points labelled (a–h) correspond to the same labelled points in figure 4.9.

condition. The responses for intermediate Ri were then obtained via continuation using these solutions as initial conditions. No systematic effort was made to identify multiple stable solutions, which do exist in certain parameter regimes (resulting in hysteresis), except in the subcritical band in the upper Ri range (the region shaded magenta in figures 4.2 and 4.15), where both the base state S and a time-dependent solution are stable and co-exist. In this region, a detailed investigation to find the edges of the hysteresis band was executed using a variety of different initial conditions.

An overview of the unsteady flow response over the extensive (Ri, Re) parameter regime considered is presented in figure 4.15, which provides, for each Re considered, the variation with Ri of the power spectral density (PSD) of the E time series. To obtain the individual PSDs, the E time series were first trimmed to remove transients, de-trended and Blackman filtered. The resulting PSDs were collated and normalised to peak power over all Ri values for each given Re. Table 4.1 contains the values of

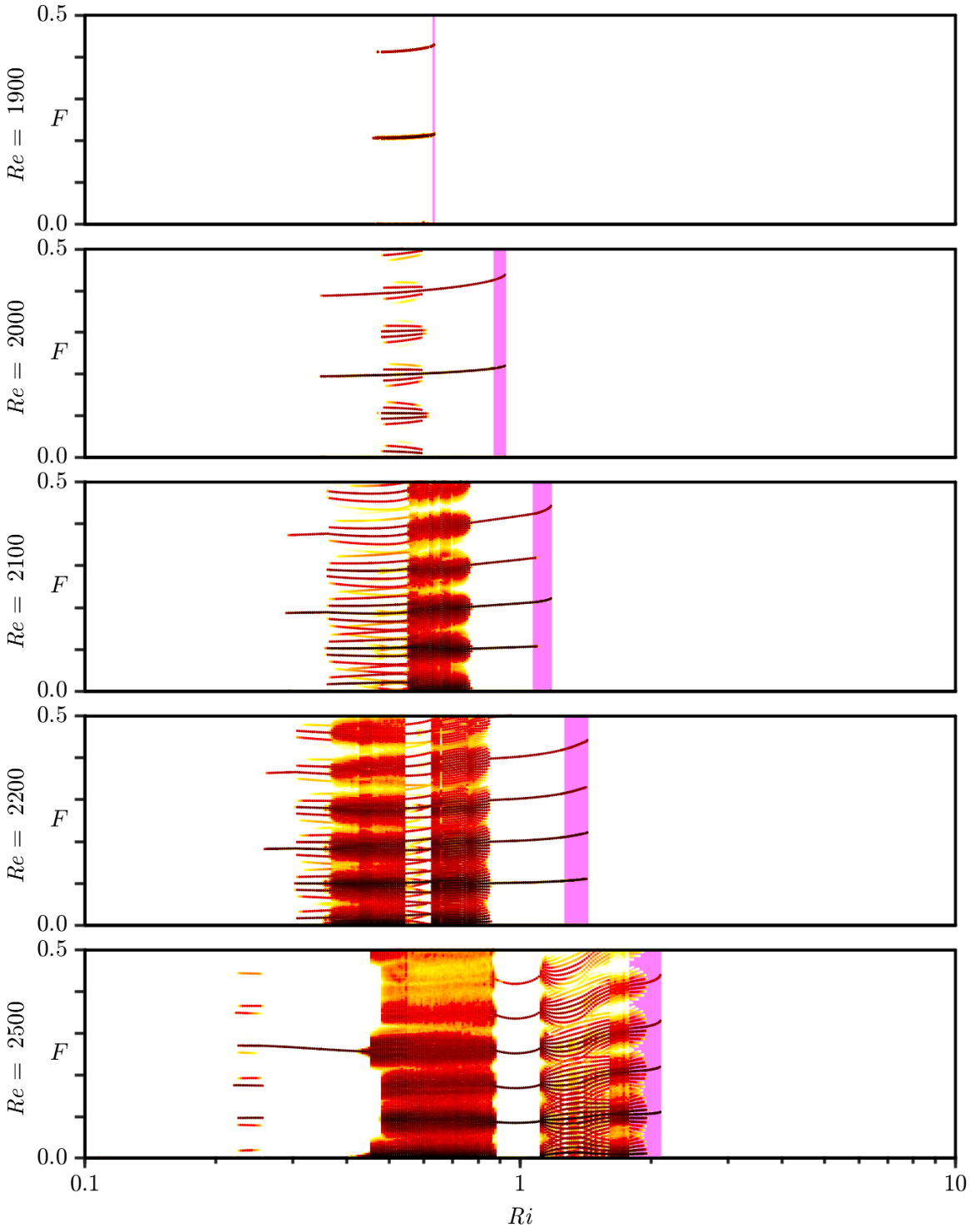

Figure 4.14: Variation of the power spectrum density (PSD) of E with Ri, in terms of scaled frequency F, for Re as indicated. Black corresponds to peak energy at the given Re, and white is $50dB$ or more below the peak.

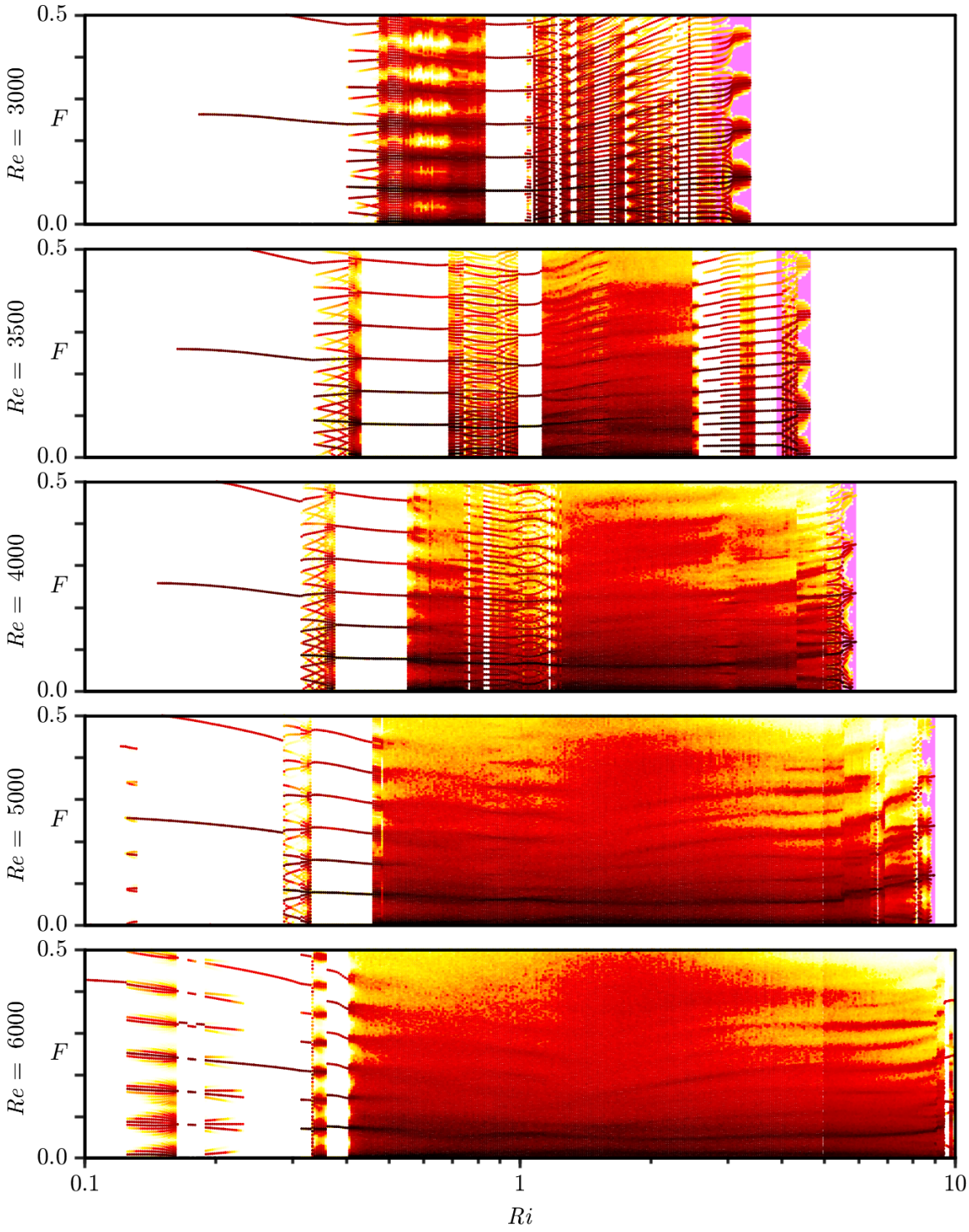

Figure 4.15: Variation of the power spectrum density (PSD) of E with Ri, in terms of scaled frequency F, for Re as indicated. Black corresponds to peak energy at the given Re, and white is $50dB$ or more below the peak.

Re	1900	2000	2100	2200	2500
peak power	0.087	0.12	0.43	0.70	1.6
Ri at peak	0.581	0.615	0.512	0.652	0.548
Re	3000	3500	4000	5000	6000
peak power	2.5	2.1	2.7	3.5	3.4
Ri at peak	0.542	0.714	0.622	0.652	0.555

Table 4.1: Peak power and corresponding Ri of E spectral data at Re as indicated.

the normalising peak power of the PSD for each Re value, as well as the Ri value at the peaks. Since E already includes a scaling Re^2, these peak values merely represent the pre-factor for this scaling, and allow comparisons across different Re. Note that peak power is consistently reached at $Ri \approx 0.6$, i.e. when shear and buoyancy forces are of comparable strength. Figure 4.15 illustrates the increasing complexity of the responses as Re is increased. It shows a "view from the top" of the normalised PSDs as a function of Ri obtained for each Re as indicated, with a colour scale from white (low energy) to red/black (high energy), corresponding to a power ratio of 10^5 (50 dB range). Values below 10^{-5} of peak power were omitted (set to white).

As Re increases, the Ri band over which an unsteady response is obtained widens. At the lower Ri end of this range, the spectra is that of a pure limit cycle (single frequency plus harmonics), identified as L_2 for $Re \approx 1900$ to 2500, L_3 for $Re \approx 3000$ to 5000, and L_5 for $Re \approx 5000$ and 6000. At both $Re = 2500$ and $Re = 5000$, the respective limit cycles L_2 and L_5 quickly transform into quasi-periodic states, and then into limit cycle L_3 as Ri increases across the Neimark–Sacker bifurcation curves emanating from the nearby double-Hopf points, dH_{23} and dH_{35}, described earlier. A pure limit cycle L_4 (figure 4.16), was also observed at $Re = 6000$ in a small range

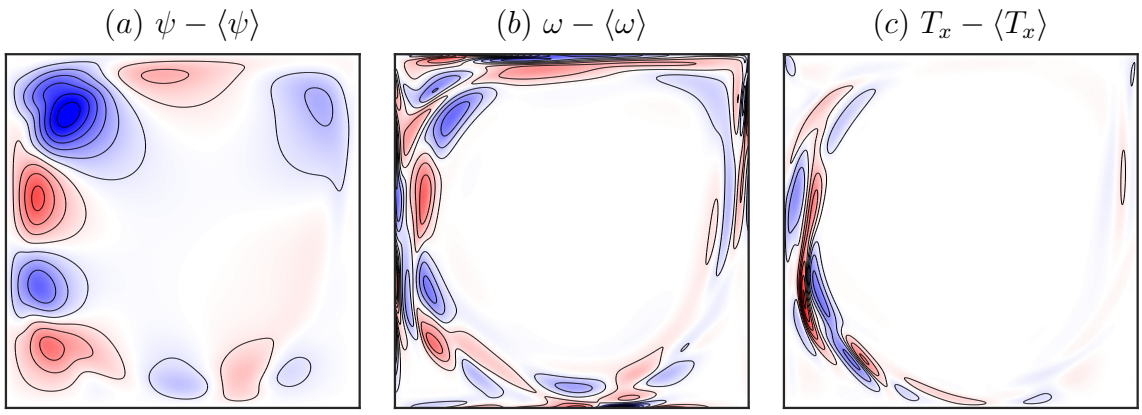

Figure 4.16: Snapshots of the deviations from their mean for streamfunction, vorticity, and horizontal temperature gradient for the limit cycle L_4 at $Re = 6000$ and $Ri = 0.17$.

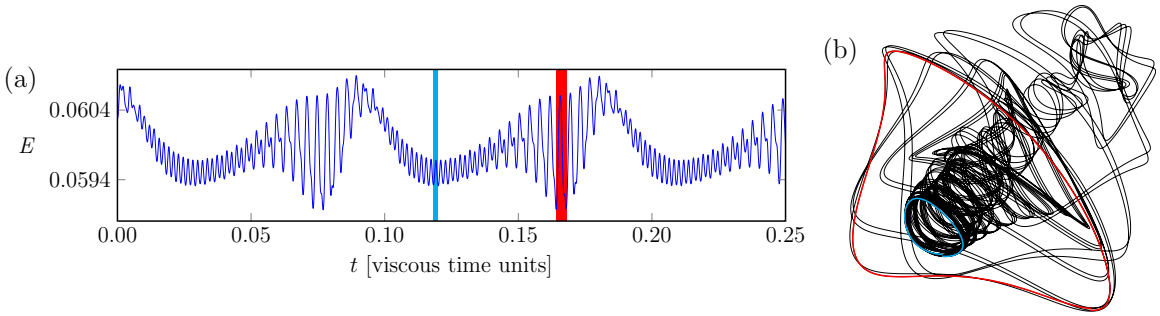

Figure 4.17: An example of global heteroclinic dynamics at $(Ri, Re) = (0.6902, 2100)$: (a) Time series of the response E over a window of 0.25 viscous units and (b) corresponding phase portrait $(E(t-\tau), E(t))$ with delay $\tau = 1/(0.3Re\sqrt{1+Ri})$.

with $Ri \approx 0.17$, close to the supercritical Hopf bifurcation curve H_5, suggesting the presence of another Hopf bifurcation H_4. In the parameter regime considered, this Hopf bifurcation is not a primary instability of the basic state S. The scaled frequency of L_4 is $F \approx 0.325$, giving a rotation number $F/4 \approx 0.081$, which is comparable to those of the other limit cycles shown in figure 4.7(b).

With increasing Ri, the spectra of the computed responses become more complex showing characteristics typical of quasi-periodic flows with incommensurate frequen-

cies. There are intervals in Ri where the spectra are periodic, due to the frequencies locking into rational ratios. These lockings are more prevalent at lower Re values. The locked regions (Arnol'd tongues) emerge from points along the Neimark–Sacker curves, which have their origin at the various double-Hopf points, and extend and interact far from the immediate vicinity of the double-Hopf points, leading to a panoply of more complex dynamical states featuring low-frequency spectral peaks associated with global homoclinic or heteroclinic behaviour Boyland [12].

In example of heteroclinic behaviour is presented in figure 4.17, which shows the E response at $Re = 2100$ and $Ri = 0.6902$. The time series (figure 4.17a) consists of a fast low-amplitude oscillation followed by a slower large-amplitude oscillation. This repeats periodically with a period of approximately 0.1 viscous time units. The short segments in the time series highlighted in blue and red correspond to times when the flow is close to the unstable (saddle) limit cycles L_2 and L_1. The nature of this near-heteroclinic cycle between the two saddle limit cycles is further illustrated in the phase portrait in figure 4.17(b), where the parts of the phase portrait corresponding to the blue and red segments of the time series are also coloured. These parts of the phase portrait have the same shape as the phase portraits of stable L_2 and L_1 limit cycles in figure 4.12(a) and (c). The rest of the phase portrait (in black) corresponds to the slow near-heteroclinic drift between the two limit cycles. These periodic drifts take approximately 0.05 viscous times, which is approximately 12 oscillations of L_1 and 24 oscillations of L_2.

An example of homoclinic behaviour is presented in figure 4.18, which shows the E response at $Re = 2750$ and selected values of $Ri \sim 0.86$. Below a critical value $Ri_c \approx 0.865625$ the response is a dyadic quasi-periodic state, with one scaled frequency that hardly varies with Ri, $F \approx 0.08$ (corresponding to a period of 0.033 viscous times), and a second lower frequency that goes to zero as $Ri \to Ri_c$. The

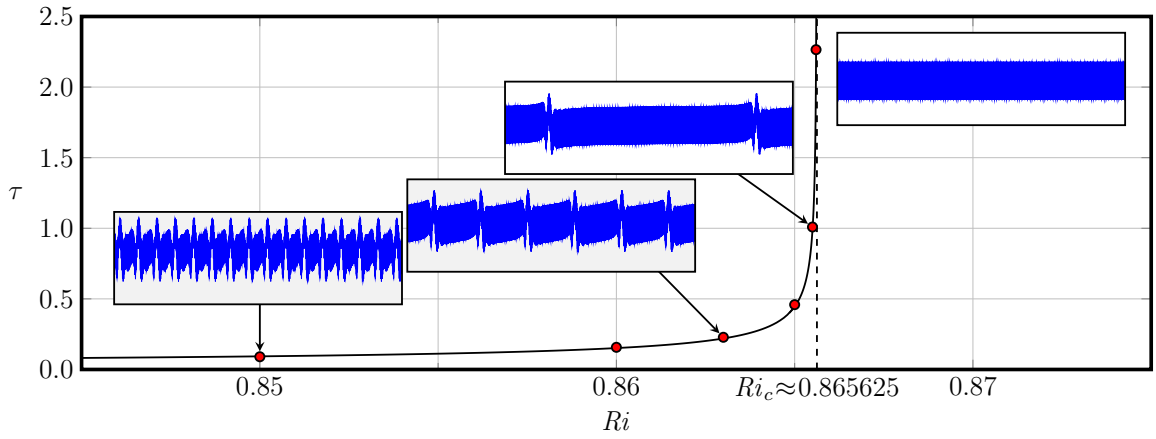

Figure 4.18: An example of homoclinic dynamics (SNIC on the torus) at $Re = 2750$ and $Ri \approx 0.86$: The quasi-period τ (in viscous time units) of a QP state (red bullets) and the black curve is the fit $\tau = 0.005 + 0.011/\sqrt{Ri_c - Ri}$, where Ri_c is the critical value of Ri at the SNIC bifurcation. The inserts show time series of $E \in [0.05, 0.06]$ over 1.4 viscous times at the indicated Ri. The time-series for $Ri > Ri_c$ show the resulting locked response on the torus.

corresponding period goes to infinity as $\tau = 0.005 + 0.011/\sqrt{Ri_c - Ri}$. The slow-fast behaviour seen in the time series terminates at $Ri = Ri_c$ with the creation of a pair of limit cycles on the torus, one unstable (saddle) and the other stable (node), at the saddle-node-on-an-invariant-cycle (SNIC) on a torus bifurcation Lopez and Marques [47]. For $Ri > Ri_c$, only the stable limit cycle on the torus is observed via direct simulations.

Figure 4.19 presents snapshots of the horizontal temperature gradient T_x at $Re = 5000$ and four selected buoyancy strengths, $Ri = 2, 4, 6$, and 8. The four responses are quasi-periodic with a very low frequency content (see figure 4.15). The snapshots are shown at a phase when the E oscillations are intense. The colourmap is scaled by $3/Ri$, so that it is inversely proportional, at fixed Re, to the buoyancy intensity measured by the Grashof number Gr. With increasing Ri, the lid-driven roller is

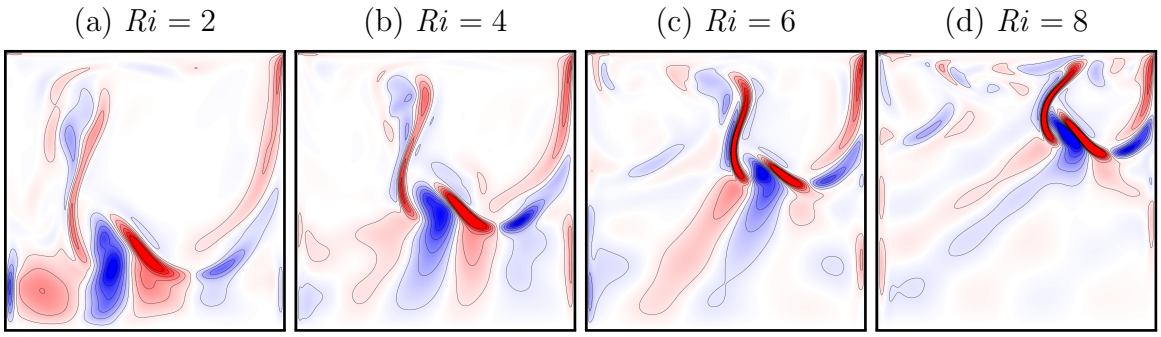

Figure 4.19: Snapshots of the horizontal temperature gradient T_x of quasi-periodic states at $Re = 5000$ and Ri as indicated; the contours are equispaced in the range $|T_x| \leq 3/Ri$. The online Wu *et al.* [93] shows animations over 0.01 viscous time.

smaller and more confined to the upper downstream corner of the cavity. In all four cases, the relatively strong buoyancy pushes back on the roller quasi-periodically, and the shear forces exerted by the roller scoop up cold fluid from below and drive it up toward the hot lid. With increasing Ri, the colder fluid tends to impinge on the top lid and is alternately deflected to the right or to the left. In the latter case, this results in a wave of smaller (boomerang-shaped) cells propagating to the top uptream (left) corner of the cavity. This wave dissipates to some degree in the boundary layers but remains sufficiently strong so as to form a buoyancy barrier identifiable by the (blue, bean-shaped) stationary T_x cell evident in figures 4.19(c, d). These dynamics are more clearly evident in the accompanying online Wu *et al.* [93].

Various flip bifurcations have also been detected above the neutral curve. Those occuring at $Re = 3500$ in the vicinity of $Ri = 3$ are relatively easy to identify in the PSDs shown in figure 4.15. For example, a frequency-locked limit cycle arising from a SNIC on the torus at $Ri \approx 2.57$ loses stability at $Ri \approx 2.63$ via a flip bifurcation, with the resulting period-doubled limit cycle itself losing stability via another flip bifurcation at $Ri \approx 2.86$. The period-quadrupled limit cycle remains stable up to

$Ri \approx 3.2$. Beyond $Ri = 3.2$, the flow is aperiodic, and then frequency locks again at $Ri \approx 3.47$.

4.5 Discussion and Conclusions

The impact of a stable temperature stratification on the flow of a fluid of Prandtl number $Pr = 1$ in a lid-driven square cavity was examined numerically over a comprehensive range of Reynolds numbers Re and bulk Richardson numbers Ri quantifying the strengths of the shear and stratification, respectively. Particular attention was placed on how the competition between shear and stratification destabilizes the flow and leads to complex dynamics.

At sufficiently small Re, the flow is steady and the results are in line with those from previous experimental studies in the square cavity Koseff and Street [36], Cohen *et al.* [15]: at lower Ri shear effects dominate and a large lid-driven roller occupies most of the cavity, while at larger Ri buoyancy effects confine the roller towards the downtream end of the top lid, leaving below a nearly stagnant linearly stratified fluid organized into a stack of weak counter-rotating horizontal cells driven by shears at the vertical walls.

For $Ri \lesssim 0.5$, the lid-driven roller drives hot fluid from the top of the cavity to interact with the colder fluid at the bottom, resulting in horizontal temperature gradients. These temperature gradient are sources of vorticity and combine with wall boundary layer effects to destabilize steady states at low Ri, compared to the isothermal case $Ri = 0$ at the same Re. The instability is a supercritical Hopf bifurcation, and the instability mode (the Hopf eigenfunction) consists of m pairs of cells of opposite-signed vorticity (or horizontal temperature gradient) that propagate around the periphery of the roller. In the limit $Ri \to 0$, this matches the Hopf instability of the isothermal lid-driven cavity, with $m = 5$. For $0 < Ri < 0.5$, we find

two more such supercritical Hopf bifurcations with $m = 3$ and 2, whose frequencies are related to an overall winding number m of the main roller.

For $Ri \gtrsim 0.5$, the instability of the steady flow switches to a subcritical Hopf, resulting in a hysteresis region where both the steady state and nonlinear unsteady states are attracting depending on initial conditions. At larger Ri this transition occurs at $Re \sim \sqrt{Ri}$. In that regime, the existence of a periodic limit cycle corresponding to a small roller with $m = 1$ confined to the downstream upper corner provides a localized periodic forcing which results in an internal wavebeam propagating into the nearly linearly stratified fluid in the rest of the container. These waves are driven by the propagating cells on the periphery of the roller, with a frequency which adjusts to the buoyancy frequency so that the wavebeams tend to propagate at 45^{circ} with increasing Ri. Indirect evidence of such internal wavebeams was inferred from time series correlations in the experiments of Cohen *et al.* [15].

Above the Hopf bifurcation curves, the various bifurcating modes interact nonlinearly and complicated dynamics ensue. The complexity increases with increasing Re; frequency spectra indicate the presence of quasi-periodic mixed modes with intervals of locking, as well as low frequency responses due to homoclinic or heteroclinic dynamics. Even though the flow has multiple frequencies, and even a broadband spectrum in some parameter regimes, for large Ri since the roller is smaller and the lower region of the cavity is stratified (albeit nonlinearly), coherent wavebeams triggered by the propagating cells along the periphery of the roller are still readily identifiable.

It is not clear to what extent three-dimensional effects, such as Taylor-Görtler vortices on the lid-driven roller, would affect the above described dynamics. It would be desirable to determine this. Cohen *et al.* [15] report that the lid-driven stratified flow is not strongly three-dimensional in their experiments, and they were in parameter regimes comparable to those we have considered. Nevertheless, the two-dimensional

results we present should be interpreted with some care. It is unfortunate that a comparably comprehensive parametric study in three dimensions is presently a daunting task.

Chapter 5

LIBRATIONAL FORCING OF A RAPIDLY ROTATING FLUID-FILLED CUBE

5.1 Abstract

The flow response of a rapidly rotating fluid-filled cube to low-amplitude librational forcing is investigated numerically. Librational forcing is the harmonic modulation of the mean rotation rate. For libration frequencies less than twice the mean rotation frequency, the system supports inertial waves. The response is comprised of two main components: resonant excitation of the inviscid inertial eigenmodes of the cube, and internal shear layers whose orientation is governed by the inviscid dispersion relation. The internal shear layers are driven by the fluxes in the forced boundary layers on walls orthogonal to the rotation axis and originate at the edges where these walls meet the walls parallel to the rotation axis, and are hence called edge beams. The relative contributions to the response from these components is obscured if the mean rotation period is not small enough compared to the viscous dissipation time, i.e. if the Ekman number is too large. We conduct simulations of the Navier–Stokes equations with no-slip boundary conditions using parameter values corresponding to a recent set of laboratory experiments, and reproduce the experimental observations and measurements. Then, we reduce the Ekman number by one and a half orders of magnitude, allowing for a better identification and quantification of the contributions to the response from the eigenmodes and the edge beams.

5.2 Introduction

The dynamics of fluid systems in rapid rotation are strongly influenced by the restorative nature of the Coriolis force, rendering the system to act like an oscillator. Systems slightly perturbed away from solid-body rotation (SBR) tend to return to SBR via viscous dissipation, but it is possible to maintain them away from SBR by continuously perturbing them. The situation becomes interesting when the deviation away from SBR is much larger than the size of the perturbation. For a simple oscillator, this happens when it is forced with small amplitude at the natural frequency. This idea provides a mechanism to extract energy from that available in the rapidly rotating flow to drive large scale flows via small amplitude mechanical forcing at or near resonant frequencies. Furthermore, this idea has wide-ranging implications in rapidly rotating geophysical and astrophysical flows Malkus [62], Tilgner [85], Noir *et al.* [71], Davidson [17], Le Bars *et al.* [39]. For rapidly rotating fluid systems, much insight has been gained from linearizing the system about SBR and considering the response to various types of forced perturbations. Greenspan [24] gives a comprehensive account of the early work in this regard, and in their review article, Le Bars *et al.* [39] give an overview of the more recent experimental, theoretical and numerical investigations of the flow response to various types of mechanical forcings, including libration, precession and tidal forcing.

The linear inviscid equations are of hyperbolic type when the disturbance frequency is less than twice the SBR frequency Lord Kelvin [34]. The inviscid inertial eigenmodes of the container, known as Kelvin modes when the container is a right-circular cylinder, have particular spatial structure depending on the disturbance frequency. These are neutral modes, i.e. the real part of the eigenvalues is zero. In a viscous setting these modes are expected to be damped, and those with higher spatial

variations more so Greenspan [24, p. 83]. So, in a rapidly rotating viscous flow, one expects to preferentially excite modes with low spatial variation via near-resonant forcing Aldridge and Toomre [4]. The spatial structure of the imposed forcing may also play a role in selecting modes of similar structure. The experiments of Boisson *et al.* [10], consisting of a rapidly rotating fluid-filled cube subjected to small amplitude libration over a range of frequencies strongly suggest that the spatial structure of the forcing indeed influences the resonant response.

A further complication in all of this is that rapidly rotating flows that are subjected to localized perturbations with frequencies less than twice the SBR frequency emit inertial wave beams from the localized perturbation along the directions of the characteristics of the hyperbolic system. For the librating cube under consideration, the localized perturbations are at the edges where the top and bottom endwalls meet the vertical sidewalls and are driven by the Ekman fluxes in the top and bottom endwall boundary layers Boisson *et al.* [10]; the vertical direction being taken in the direction of the mean rotation. The flow response can be dominated by the beams, completely swamping the contribution from the resonantly excited eigenmode. Which dominates, beam or eigenmode, is not straightforward to predict *a priori*, and it depends on how fast the system is rotating compared to how fast it viscously dissipates, and on how small the forcing amplitude is. The concepts of inviscid inertial eigenmodes and inertial wave beams stem from analyzing the governing equations in two limits: inviscid (vanishing Ekman number) and linear (vanishing Rossby number). These limits present challenges to both experimental investigations and to numerical simulations of the Navier–Stokes equations.

Here we report on numerical simulations of the full three-dimensional Navier–Stokes equations with no-slip boundary conditions corresponding to the librating cube experiments of Boisson *et al.* [10]. We reproduce their experimental findings

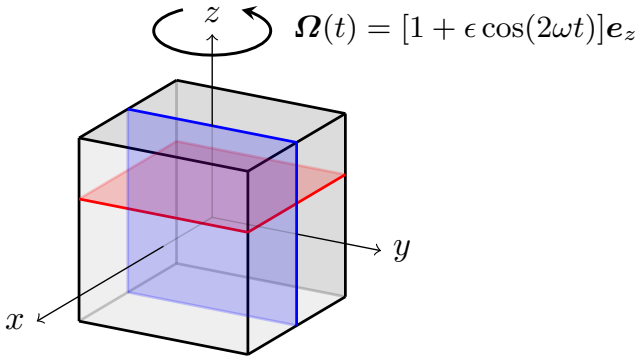

Figure 5.1: Schematic of the librating cube, including the observation planes $x = 0$ (vertical) and $z = 1/6$ (horizontal).

and then consider a series of simulations in which both the Ekman number and the Rossby number are reduced significantly, and we also extend the range of libration frequencies considered to cover from zero to twice the SBR frequency. We find peak responses at many frequencies and are able to identify either low-order inertial inviscid eigenmodes or low-order retracing edge beams in these responses. If the Ekman number is too large, the contributions from these eigenmodes and retracing beams are blended due to viscous effects. The beams are present at all frequencies, and for moderate Ekman numbers their contribution to the response is essentially uniform in frequency, regarless of whether they retrace or not. Reducing the Ekman number increases the separation between the peaks by both sharpening the peaks and reducing detuning. Even for very small libration amplitudes (Rossby number), nonlinear effects are evident in the response, primarily consisting of the beams pinning and deforming the eigenmode spatio-temporal structure.

5.3 Governing Equations and Their Symmetries

Consider a cube with sides of length L, completely filled with an incompressible fluid of kinematic viscosity ν that has a mean rotation Ω_0 that is modulated harmonically at a frequency $\sigma_0/2$ and relative amplitude ϵ, which is often referred to as the Rossby number of the libration. The system is non-dimensionalized using L as the length scale and $1/\Omega_0$ as the time scale, and described in terms of a non-dimensional Cartesian co-ordinate system $\boldsymbol{x} = (x, y, z)$ that is fixed in the cube, with the origin at the center of the cube and the rotation vector pointing in the z direction (which we refer to as the vertical direction). The non-dimensional velocity field is $\boldsymbol{u} = (u, v, w)$ and the corresponding vorticity field is $\boldsymbol{\nabla} \times \boldsymbol{u} = (\omega_x, \omega_y, \omega_z)$. The non-dimensional angular velocity is

$$\boldsymbol{\Omega}(t) = [1 + \epsilon \cos(2\omega t)]\boldsymbol{e}_z \,, \tag{5.1}$$

where the non-dimensional libration frequency $\omega = \sigma_0/2\Omega_0$, and $\boldsymbol{e}_z$ is the unit vector in the z direction. Figure 5.1 shows a schematic of the system. Using a non-inertial frame of reference, the cube frame, introduces both a Coriolis and an Euler body force into the (non-dimensional) governing equations:

$$\frac{\partial \boldsymbol{u}}{\partial t} + \boldsymbol{u} \cdot \boldsymbol{\nabla}\boldsymbol{u} + 2\boldsymbol{\Omega} \times \boldsymbol{u} + \frac{d\boldsymbol{\Omega}}{dt} \times \boldsymbol{x} = -\boldsymbol{\nabla} p + E\nabla^2 \boldsymbol{u}, \quad \boldsymbol{\nabla} \cdot \boldsymbol{u} = 0, \quad \boldsymbol{u}|_{\partial \mathcal{C}} = \boldsymbol{0}, \tag{5.2}$$

where $E = \nu/\Omega_0 L^2$ is the Ekman number giving the ratio of the mean rotation time scale, $1/\Omega_0$, to the viscous time scale, L^2/ν. In the cube frame of reference, the no-slip boundary conditions on all six walls of the cube are trivial ($\partial\mathcal{C}$ signifies the boundaries of the cube). Note that Boisson *et al.* [10] define the Ekman number as $\nu/[2\Omega_0(L/2)^2]$ where they used $L/2$ as the length scale and $1/2\Omega_0$ as the time scale, so that their Ekman number is twice ours.

The Navier–Stokes system (6.5) is invariant to a reflection through the plane $z = 0$, and a $\pi/2$ rotation about the z-axis. The actions of these symmetries on the velocity

and pressure are

$$\begin{aligned}\mathcal{K}_z(u,v,w,p)(x,y,z,t) &= (u,v,-w,p)(x,y,-z,t),\\ \mathcal{R}_{\pi/2}(u,v,w,p)(x,y,z,t) &= (-v,u,w,p)(-y,x,z,t).\end{aligned} \tag{5.3}$$

These are the only spatial symmetries of the Navier–Stokes system (6.5).

The inviscid inertial modes are the eigensolutions to the inviscid limit of system (6.5), linearized about the state of solid-body rotation, i.e.

$$\frac{\partial \boldsymbol{u}}{\partial t} + 2\boldsymbol{\Omega}_0 \times \boldsymbol{u} = -\boldsymbol{\nabla} p, \qquad \boldsymbol{\nabla}\cdot\boldsymbol{u} = 0, \qquad \boldsymbol{u}\cdot\boldsymbol{n}|_{\partial\mathcal{C}} = 0, \tag{5.4}$$

where $\boldsymbol{n}$ is the normal at the walls of the cube and $\boldsymbol{\Omega}_0 = \boldsymbol{e}_z$.

Since the linearized inviscid system (5.4) is a direct reduction from (6.5), it also is invariant to $\mathcal{K}_z$ and $\mathcal{R}_{\pi/2}$. The system (5.4) is invariant to an additional spatial symmetry,

$$\overline{\mathcal{R}}_{\pi/2}(u,v,w,p)(x,y,z,t) = (v,-u,-w,-p)(-y,x,z,t). \tag{5.5}$$

The nonlinear term $\boldsymbol{u}\cdot\boldsymbol{\nabla}\boldsymbol{u}$ is the sole term in (6.5) which breaks $\overline{\mathcal{R}}_{\pi/2}$. The important point is that both the Euler force and the viscous term in (6.5) are invariant to $\overline{\mathcal{R}}_{\pi/2}$, so that it is not that the libration does not have this symmetry, but rather that the forced system is nonlinear. For small enough forcing ϵ, (6.5) has a unique solution which is invariant to all symmetries of the system ($\mathcal{K}_z$ and $\mathcal{R}_{\pi/2}$) and is synchronous with the forcing. In (E,ϵ)-parameter space, there is a critical curve dividing the parameter space into regions where this symmetric synchronous state is stable and where it is not. The objective of the experiments in Boisson *et al.* [10] was to see what is the forced response for small E and ϵ, and how the response is related to the eigenmodes of (5.4). A conclusion from their study was that only eigenmodes with the symmetry of the librational forcing could be excited. They reasoned that the modes with $\overline{\mathcal{R}}_{\pi/2}$ invariance could not be excited because the librational forcing does

not have this symmetry. However, librational forcing is described by the Euler force, which is both $\mathcal{R}_{\pi/2}$ and $\overline{\mathcal{R}}_{\pi/2}$ invariant. It is because (6.5) is nonlinear that it has no $\overline{\mathcal{R}}_{\pi/2}$-invariant solutions.

5.4 Numerical Technique for the Viscous Nonlinear Forced Flow

The Navier–Stokes system (6.5) is discretized using a spectral-collocation method in all three spatial directions. The velocity and pressure are approximated by polynomials of degree N written in barycentric form with weights $w_0 = 0.5$, $w_n = (-1)^n$ for $n \in [1, N-1]$, and $w_N = 0.5(-1)^N$, associated to the Chebyshev–Gauss–Lobatto grid. Spatial differentiation is performed via direct matrix-vector multiplication by the pseudospectral differentiation matrix (common to all three directions).

The time integration scheme used is the fractional-step improved projection method of Hugues and Randriamampianina [27], based on a linearly implicit and stiffly stable, second-order accurate scheme combining a backward differentiation formula for the linear terms and an explicit mix, equivalent to linear extrapolation, of Adams–Moulton and Adams–Bashforth steps for the nonlinear convective terms Vanel *et al.* [88]. The predictor stage of the fractional step method solves a Helmholtz equation for a pressure field, for which Neumann conditions consistent with (6.5) are applied at the walls. The corrector stage then projects the resulting predicted velocity field onto the space of (discretely) divergence-free polynomials via a Stokes problem, which is also handled by solving a Helmholtz equation for the corrected pressure, albeit with homogeneous Neumann boundary conditions. Further details can be found in Hugues and Randriamampianina [27].

The code was verified and validated against the experimental results of Boisson *et al.* [10], most of which are reproduced numerically in following section. The Ekman number E determines the thickness of the boundary layers and edge beams in the

interior, and these are the features that need to be resolved numerically. The boundary layer thickness scales with $E^{1/2}$, it is the thinnest length scale in the problem, and the edge beam thickness scales with $E^{1/3}$ Wood [89]. The Chebyshev–Gauss–Lobatto collocation grid distribution leads to very well-resolved boundary layers. For small libration amplitudes ($\epsilon<0.1$), ϵ does not add any further constraints on the spatial (or temporal) resolution requirements. In this study, we report on results for Ekman numbers in the range $E\in[10^{-6},10^{-4.6}]$ (the larger value corresponding to the experimental condition used by Boisson *et al.* [10]), for which we used different spatial resolutions. We used $N^3=72^3$ collocation points for $E\geq10^{-5}$, $N^3=96^3$ for $E=10^{-5.5}$, and $N^3=156^3$ for $E=10^{-6}$. With these grid resolutions, the solutions manifest spectral convergence of at least 6 orders of magnitude. The required temporal resolution depends on the libration frequency ω. For $\omega\in[0.58,1)$, we used 100 time-steps per libration period $\tau=\pi/\omega$ so that the time step $\delta t=\tau/100$. For the lower frequencies, $\omega<0.58$, we used $80/\omega$ (rounded up to the nearest integer) time-steps per period. Being a forced oscillator problem, the response consists of a transient and a forced response. In order to examine the forced response, the system needs to be integrated in time until the transient contribution is negligible. As E is reduced, the transient is longer lived. For $E=10^{-6}$, we find that this occurs in a few multiples of the spin-up time $E^{-1/2}$, which is much shorter than the viscous time E^{-1}.

Since the flows being studied are $\mathcal{K}_z$-invariant, the volume integrals of the velocity $\boldsymbol{u}$ and helicity $H=\boldsymbol{u}\cdot(\boldsymbol{\nabla}\times\boldsymbol{u})$ both vanish, but their variances do not. Convenient global measures of the forced response are the time-averages of the standard deviations away from solid-body rotation in the velocity, Σ_V, and the helicity, Σ_H, relative to the amplitude of the libration ϵ, where

$$\Sigma_V^2 = \frac{1}{\tau\epsilon^2}\int_0^\tau \int_{\mathcal{V}} |\boldsymbol{u}|^2 \, d\mathcal{V}\, dt \quad \text{and} \quad \Sigma_H^2 = \frac{1}{\tau\epsilon^4}\int_0^\tau \int_{\mathcal{V}} |\boldsymbol{u}\cdot(\boldsymbol{\nabla}\times\boldsymbol{u})|^2 \, d\mathcal{V}\, dt. \tag{5.6}$$

The volume integrals are computed over a volume $\mathcal{V}$ which excludes the boundary layers. The thickness of the boundary layers was determined from z-profiles of the ω_x vorticity component Lopez and Marques [48], Gutierrez-Castillo and Lopez [25, similar to the approach in]. As expected, the thickness varies with $E^{1/2}$. Also note that $0.5\epsilon^2\Sigma_V^2$ is the time-average of the kinetic energy in $\mathcal{V}$.

5.5 Results

We begin by simulating two cases that were investigated in detail in the experiments of Boisson *et al.* [10]. These cases were at libration frequencies $\omega = 0.6742$ and 0.6484, both with $E = 2.65\times10^{-5} \approx 10^{-4.6}$ and $\epsilon = 0.04 \approx 10^{-1.4}$. These two frequencies were selected because they correspond to the lowest order eigenmodes with $n = 2$ (a full sine wavelength in z) that are $\mathcal{R}_\pi$ invariant ($s = +$), and they are the leading two such modes: $[2, 1, +]$ ($M_{2.1}$ in our notation) for $\omega = 0.6742$, and $[2, 2, +]$ (which is $\overline{\mathcal{R}}_{\pi/2}$ but not $\mathcal{R}_{\pi/2}$ invariant) for $\omega = 0.6484$. Figures 5.2(a–d) show the horizontal vorticity ω_x in the plane $x = 0$ at phases $\varphi = 2\omega t \bmod 2\pi = 0$ and $\pi/2$, and figures 5.2(e–h) show the vertical vorticity ω_z in the plane $z = 1/6$, also at phases $\varphi = 0$ and $\pi/2$. These can be compared directly with the experimental results in the same planes and phases in figures 5 and 6 of Boisson *et al.* [10]. Furthermore, the online movie 1 of our simulations can also be directly compared with the corresponding movies of the experimental results which Boisson *et al.* [10] make available as online supplementary material, showing animations over a libration period. There is excellent agreement between our numerical simulations and the experimental measurements. As noted by Boisson *et al.* [10], the $\omega = 0.6742$ case shows the structure of the eigenmode $[2, 1, +]$

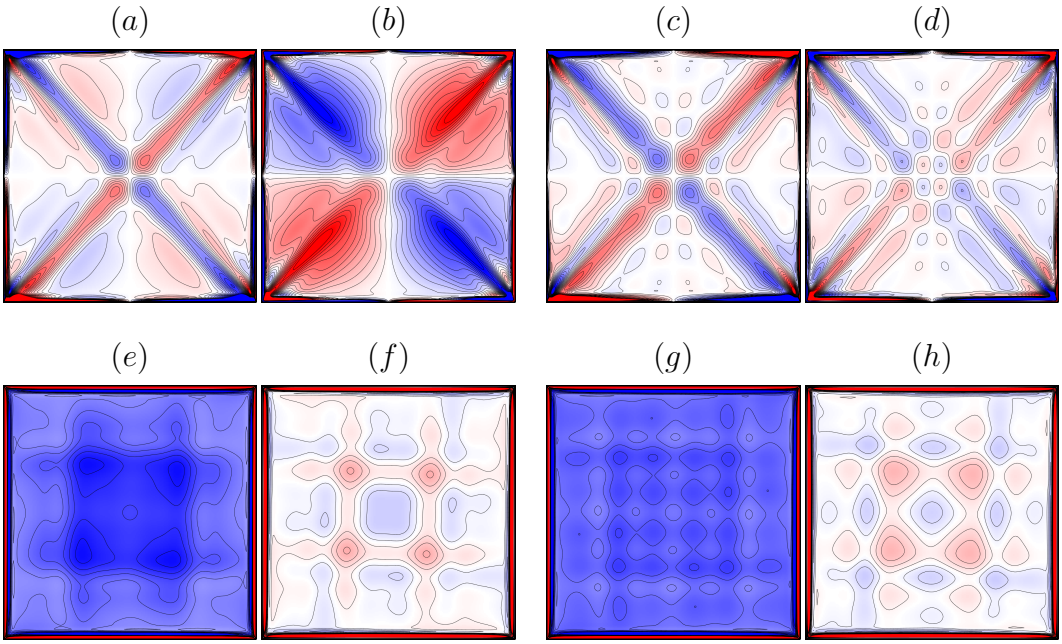

Figure 5.2: Contours of ω_x in the vertical plane $x=0$ for $\omega=0.6742$ at phases $\varphi=2\omega t$ mod 2π of the oscillation (a) $\varphi=0$ and (b) $\varphi=\pi/2$, and for $\omega=0.6484$ at phases (c) $\varphi=0$ and (d) $\varphi=\pi/2$, and of ω_z in the vertical plane $z=1/6$ for $\omega=0.6742$ at phases (e) $\varphi=0$ and (f) $\varphi=\pi/2$, and for $\omega=0.6484$ at phases (g) $\varphi=0$ and (h) $\varphi=\pi/2$, all for $(E,\epsilon)=(10^{-4.6},10^{0.04})$ corresponding to the two experimental cases in figures 5 and 6 of Boisson *et al.* [10]. Contour levels are equispaced $|\omega_x|\leq 3000$ and $|\omega_z|\leq 5000$. See the online movie 1 for animations over one libration period.

($M_{2.1}$), particularly during phases of the libration period where the edge beams are weakest, but the $\omega = 0.6484$ case does not have the horizontal structure of the $[2, 2, +]$ eigenmode, which is $\overline{\mathcal{R}}_{\pi/2}$ but not $\mathcal{R}_{\pi/2}$ invariant. It is clear from figures 5.2(g, h) that the response at $\omega = 0.6484$ is $\mathcal{R}_{\pi/2}$ invariant.

For the same two libration frequencies, $\omega = 0.6742$ and $\omega = 0.6484$, we varied ϵ from 0.02 to 0.16, as was done in Boisson *et al.* [10] to show that the kinetic energy of the response (measured in the plane $z = 1/6$) scales with ϵ^2. We have verified this, and hence defined Σ_V^2 in (6.11) with an ϵ^{-2} factor and Σ_H^2 with an ϵ^{-4} factor.

Boisson *et al.* [10] studied the system response to different librational frequencies in the range $\omega \in [0.60, 0.73]$, for $E = 2.65 \times 10^{-5}$ and $\epsilon = 0.02$. Note that over this range of ω, the linear dispersion relation dictates that the edge beams are inclined with respect to the (x, y)-plane at angles ranging from $\arccos(0.60) \approx 53.13$ degrees to $\arccos(0.73) \approx 43.11$ degrees. To quantify the response, they used particle image velocimetry (PIV) measurements of the velocity in the vertical plane $x = 0$ (excluding the boundary region 8% in from the walls as the PIV measurements there were unreliable) to calculate the corresponding $\mathcal{L}_2$ norm of the kinetic energy associated with the velocity components in that measurement plane, scaled by ϵ^{-2}. Their results (figure 8 in their paper) showed a well-defined peak at $\omega \approx 0.676$, which they associated with the $[2, 1, +]$ mode ($M_{2.1}$ in our notation), which is $\mathcal{K}_z \times \mathcal{R}_{\pi/2}$ invariant. Surrounding this peak, the response is nearly constant at about 15% of the peak response, which they interpreted as being associated with the kinetic energy of the edge beams. They also noted the presence of a slight bump in the response at $\omega \approx 0.695$, and suggested that this could be attributed to the $[4, 5, +]$ mode ($M_{4.3}$), which has eigenfrequency $\sigma \approx 0.6962$ and is also $\mathcal{K}_z \times \mathcal{R}_{\pi/2}$ invariant. They did not report any clear evidence of any other eigenmodes being excited.

Boisson *et al.* [10] also tried to find some relationship between the low-order in-

$R_{1.9}$: 0.1104	$R_{1.8}$: 0.1240	$R_{1.7}$: 0.1414	$R_{1.6}$: 0.1644	$R_{1.5}$: 0.1961	$R_{2.9}$: 0.2169
$R_{1.4}$: 0.2425	$R_{2.7}$: 0.2747	$R_{1.3}$: 0.3162	$R_{3.8}$: 0.3511	$R_{2.5}$: 0.3714	$R_{3.7}$: 0.3939
$R_{4.9}$: 0.4061	$R_{1.2}$: 0.4472	$R_{5.9}$: 0.4856	$R_{4.7}$: 0.4961	$R_{3.5}$: 0.5145	$R_{5.8}$: 0.5300
$R_{2.3}$: 0.5547	$R_{5.7}$: 0.5812	$R_{3.4}$: 0.6000	$R_{7.9}$: 0.6139	$R_{4.5}$: 0.6247	$R_{5.6}$: 0.6402
$R_{6.7}$: 0.6508	$R_{7.8}$: 0.6585	$R_{8.9}$: 0.6644	$R_{1.1}$: 0.7071	$R_{9.8}$: 0.7474	$R_{8.7}$: 0.7526
$R_{7.6}$: 0.7593	$R_{6.5}$: 0.7682	$R_{5.4}$: 0.7809	$R_{9.7}$: 0.7894	$R_{4.3}$: 0.8000	$R_{7.5}$: 0.8137
$R_{3.2}$: 0.8321	$R_{8.5}$: 0.8480	$R_{5.3}$: 0.8575	$R_{7.4}$: 0.8682	$R_{9.5}$: 0.8742	$R_{2.1}$: 0.8944
$R_{9.4}$: 0.9138	$R_{7.3}$: 0.9191	$R_{5.2}$: 0.9285	$R_{8.3}$: 0.9363	$R_{3.1}$: 0.9487	$R_{7.2}$: 0.9615
$R_{4.1}$: 0.9701	$R_{9.2}$: 0.9762	$R_{5.1}$: 0.9806	$R_{6.1}$: 0.9864	$R_{7.1}$: 0.9899	$R_{8.1}$: 0.9923
$R_{9.1}$: 0.9939					

Table 5.1: Retracing rays, $R_{i.j}$, with $i, j \leq 9$, and their corresponding frequency (equivalent cases $R_{\gamma i.\gamma j}$ with $\gamma \neq 1$ are not included).

viscid inertial modes (i.e. $[n, m, +]$ with n even and both n and m small) and the low-order retracing rays. The ray tracing concept relates to the characteristics of the linear inviscid system (5.4). The characteristics are aligned with respect to the mean rotation axis according to the linear dispersion relation; for a disturbance frequency ω, characteristics are inclined at angle β with respect to the (x, y) plane such that $\cos\beta = \omega$. Rays are traced in a vertical plane including the rotation axis, say $x = 0$, from the edges of the cube where a vertical wall ($y = \pm L/2$) and a horizontal wall ($z = \pm L/2$) meet. The motivation for this is that the imbalance in boundary layer fluxes on the vertical and horizontal walls leads to localized perturbations at the edges which propagate as edge beams into the interior along the characteristic directions. In the inviscid setting, these characteristics are surfaces of discontinuity which are regularized by viscosity into shear layers, i.e. the so-called beams Wood [89]. Retracing rays start from an edge, and after a finite number of reflections off the walls, end

up at the same or a different edge. The angle that a retracing ray makes with the (x, y) plane is $\beta = \arctan(j/i)$, such that

$$\omega = \cos\left(\arctan(j/i)\right) = i/\sqrt{i^2 + j^2}, \tag{5.7}$$

where i and j are the number of reflections off the vertical and horizontal walls, respectively (reflections at edges increment both i and j). Table 5.1 lists the frequencies ω (rounded off to 4 significant figures) associated to the low-order retracing rays $R_{i.j}$ with $i, j \leq 9$. Note that $R_{\gamma i.\gamma j}$ for any γ are equivalent, and so only the cases with $\gamma = 1$ are listed. In the frequency range considered in the experiments of Boisson *et al.* [10], $\omega \in [0.60, 0.73]$, there are exactly 3 low-order retracing rays cases, $R_{i.j}$ with $i, j \leq 5$. These are $R_{1.1}$ at $\omega = 0.7071$, $R_{3.4}$ at $\omega = 0.600$, and $R_{4.5}$ at $\omega = 0.6247$. For $E \approx 10^{-4.6}$ used in the experiments, and the energy norm in the plane

that was used, there were no responses at or near these frequencies. However, it should be noted that the beams are viscously attenuated Cortet *et al.* [16]. They are strongest near the edges from where they are emitted, and lose intensity along their path. They also lose intensity upon wall reflections through the viscous boundary layers. So, for relatively large E, there is little difference in the response from a low-order retracing case compared to a high-order case, or to a non-retracing case for that matter. This accounts for the observed near-constant response away from the single response peak at $\omega \approx 0.676$. In order to detect a signature from a retracing ray case, it is desirable to use smaller E. Even then, it is also important to use an appropriate measure. While the kinetic energy can provide a good measure for a smooth global quantity, such as an eigenmode, it does not do as well in quantifying the strength of a shear layer; the helicity variance Σ_H^2 turns out to be a better measure. This is consistent with the property that inertial waves are intrinsically helical [17, §3.3.1].

In order to further explore the system's response to librational forcing, and clarify

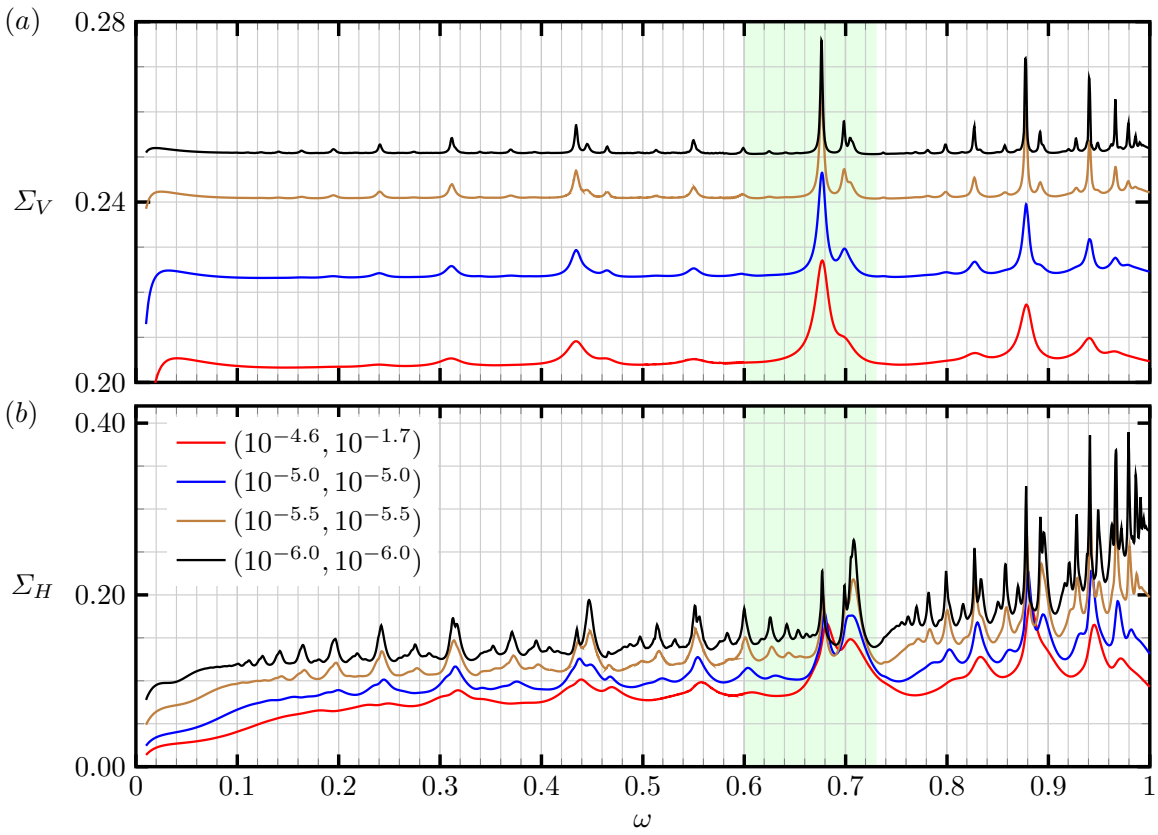

Figure 5.3: Variation of (a) Σ_V and (b) Σ_H with ω for (E, ϵ) as indicated. The shaded band corresponds to the ω range considered in Boisson *et al.* [10].

the interpretation of the response in terms of linear inviscid concepts, it is desirable to reduce both E and ϵ. This is challenging both experimentally and numerically. Numerically, we have computed the responses not only for the E, ϵ and ω values covered in the experimental study Boisson *et al.* [10], but have also extended the ranges to $E \in [10^{-6}, 10^{-4.6}]$, and ϵ as small as 10^{-6}. These much smaller E and ϵ cases bring us a little closer to the linear inviscid limit. Also, we extended the frequency range to $\omega \in (0, 1)$ with a very fine resolution $\delta\omega = 0.001$ (with refinement about some major peaks using $\delta\omega = 0.0005$). Reducing E progressively reveals more peaks in the responses, and the peaks that were present at the larger E become sharper and shift slightly as the effects of viscous detuning are reduced.

Figure 5.3(a) is the Σ_V–ω response diagram. Focusing on the response curve for $(E,\epsilon)=(2.65\times10^{-5},10^{0.02})\approx(10^{-4.6},10^{-1.7})$, corresponding to the experiments of Boisson *et al.* [10], we find excellent qualitative agreement between their time-averaged kinetic energy response and our Σ_V response. The quantitative differences are due to our use of a global measure (as noted earlier, $0.5\epsilon^2\Sigma_V^2$ is the time-average of the kinetic energy in the cube volume, excluding boundary layer contributions) rather that the experimental use of only the two velocity components in the measurement plane (excluding 8% of the plane in from the wall). The corresponding Σ_H response at $(E,\epsilon)\approx(10^{-4.6},10^{-1.7})$ in figure 5.3(b) shows a clearer, but still broad, peak in the neighborhood of $\omega=0.69$ corresponding to the slight bump in the energy response noted in the experiments and also present in our Σ_V response. As discussed in Boisson *et al.* [10], this may be due to another eigenmode being resonantly excited, but being of higher order than $M_{2.1}$ it is more viscously damped at this E, and also the bump is near $\omega=0.7071$ which corresponds to the lowest order retracing ray $R_{1.1}$. Given that the bump in Σ_V becomes a clear peak in Σ_H lends further weight to the interpretation of $R_{1.1}$ contributing to the response. Reducing E sharpens the responses and helps to distinguish the contributions.

For $(E,\epsilon)=(10^{-6},10^{-6})$, the highest peak in the Σ_V response occurs at $\omega=0.676$, which is close to the frequency of the eigenmode $M_{2.1}$. There are two other peaks at $\omega=0.698$ and 0.705, and in the vicinity of these two peaks are the frequencies of the eigenmodes $M_{4,3}$ Boisson *et al.* [[4, 5, +] in the notation of 10] and $M_{6,6}$ ([6, 11, +]), which are both $\mathcal{K}_z\times\mathcal{R}_{\pi/2}$ invariant. There is also a small bump close to $\omega=0.62$, but in the vicinity of this bump there are no low-order $\mathcal{K}_z\times\mathcal{R}_{\pi/2}$ symmetric eigenmodes. Also, in the vicinity of $\omega=0.7$, the edge beams are being driven at approximately 45 degrees with respect to the rotation vector. Therefore, it is difficult to say if the peak in Σ_V at $\omega=0.705$ is due to a resonance with the eigenmode $M_{6.,6}$ or if it is due to

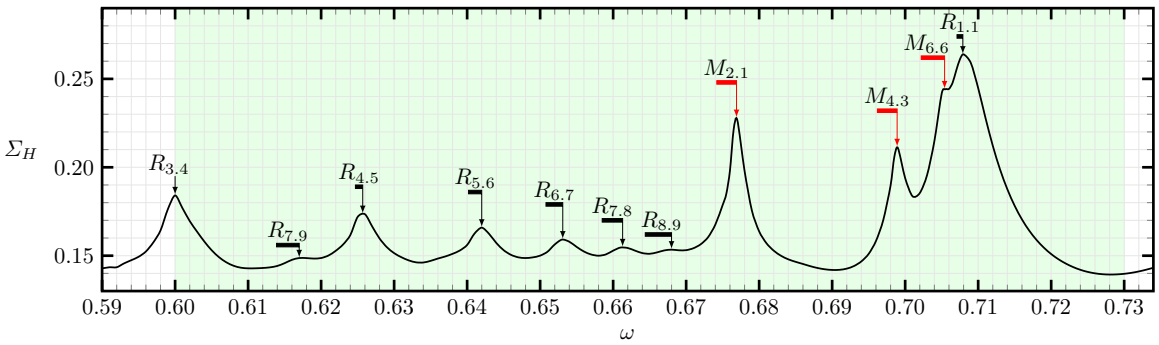

Figure 5.4: Close-up of the Σ_H–ω response for $(E,\epsilon)=(10^{-6},10^{-6})$ shown in figure 5.3, with the major peaks identified, along with the deviation from their ominal frequency (detuning). The detuning is indicated with a horizontal bar (black for $R_{i.j}$ and red for $M_{n.m}$) whose ends are at the corresponding inviscid frequency and the peak's frequency.

the retracing ray $R_{1.1}$. Actually, the response peak has contributions from both $M_{6.,6}$ and $R_{1.1}$. In the Σ_H response, the highest peak occurs at $\omega=0.707$, and this is very close to the $R_{1.1}$ frequency $\omega=1/\sqrt{2}\approx 0.7071$.

We now restrict our attention to the Σ_H response diagram at $(E,\epsilon)=(10^{-6},10^{-6})$, since Σ_H is much better at capturing localized responses, such as beams, in the flow dynamics, while also detecting resonant low-order eigenmodes. In figure 5.3(b) four dominant peaks are observed in the (highlighted) range $\omega\in[0.6,0.73]$ considered by Boisson *et al.* [10], at frequencies $\omega=0.677$, 0.699, 0.705 and 0.708. In order to more clearly see the details, figure 5.4 is a close-up over the frequency range $\omega\in[0.59,0.73]$, and it includes identifications of the major peaks with either low-order retracing rays or low-order eigenmodes, and the associated viscous detuning (i.e., the difference between the peak frequency and the frequency of the associated retracing ray or eigenmode). In the following, we elaborate on how these identifications are arrived at.

Figure 5.5 shows snapshots of ω_x in the vertical plane $x=0$ at phase $\varphi=\pi/2$ for the frequencies ω of the four main peaks in figure 5.4, together with the normalized

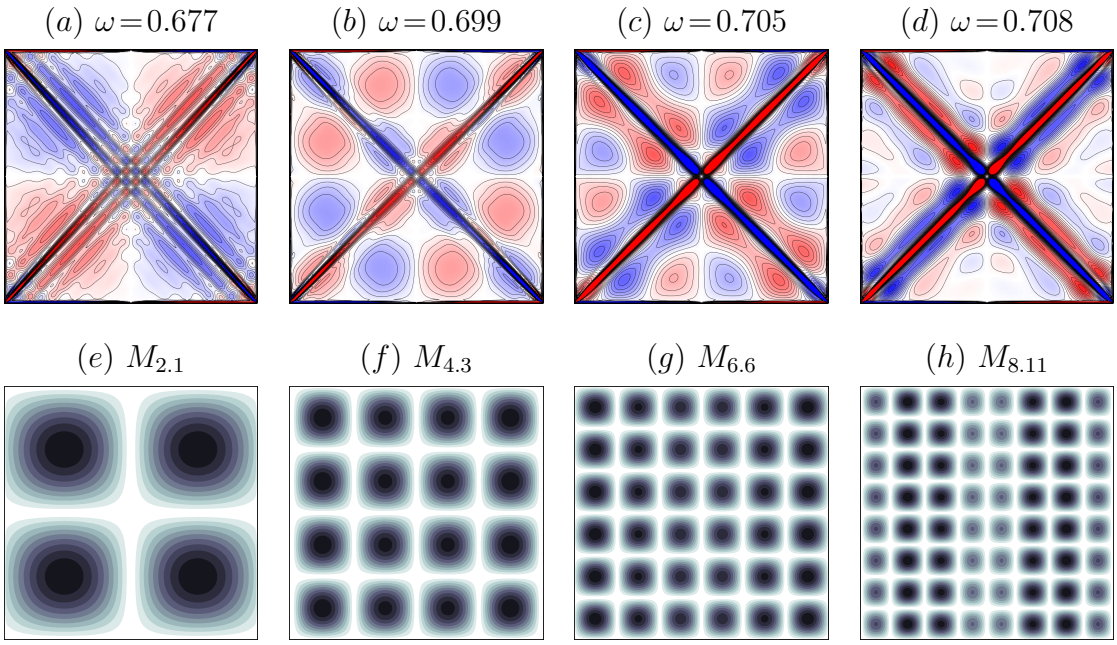

Figure 5.5: Contours of (a–d) ω_x in the vertical plane $x=0$ at the phase $\varphi=\pi/2$, for $(E,\epsilon)=(10^{-6},10^{-6})$ and ω as indicated, and (e–h) the normalized amplitude of ω_x of the inviscid inertial eigenmodes $M_{n.m}$, with n and m as indicated, in the vertical plane $x=0$. All contour levels are equispaced with $\omega_x\in[-2.5,2.5]$ for (a–d).

amplitude of ω_x of the matching low-order inviscid inertial eigenmodes $M_{n.m}$, whose eigenfrequencies are close to these ω values. Figure 5.6 shows snapshots of ω_z at the same phase in the horizontal plane $z=0.45$ (close to the top wall), together with corresponding ω_z-amplitude of the eigenmodes in a horizontal plane. The online movies 2, 3, 4 and 5 are animations of these (both nonlinear simulations and corresponding inviscid inertial eigenmodes) over one libration period, providing additional insight.

At $\omega=0.677$, the characteristic four cells in the vertical plane (figure 5.5e) and one cell filling the horizontal plane (figure 5.6e) of eigenmode $M_{2.1}$, whose eigenfrequency is $\sigma\approx0.6742$, are easily recognizable in figures 5.5(a) and 5.6(a), respectively, and animated over one period in movie 2. The numerical simulations of ω_x in the vertical

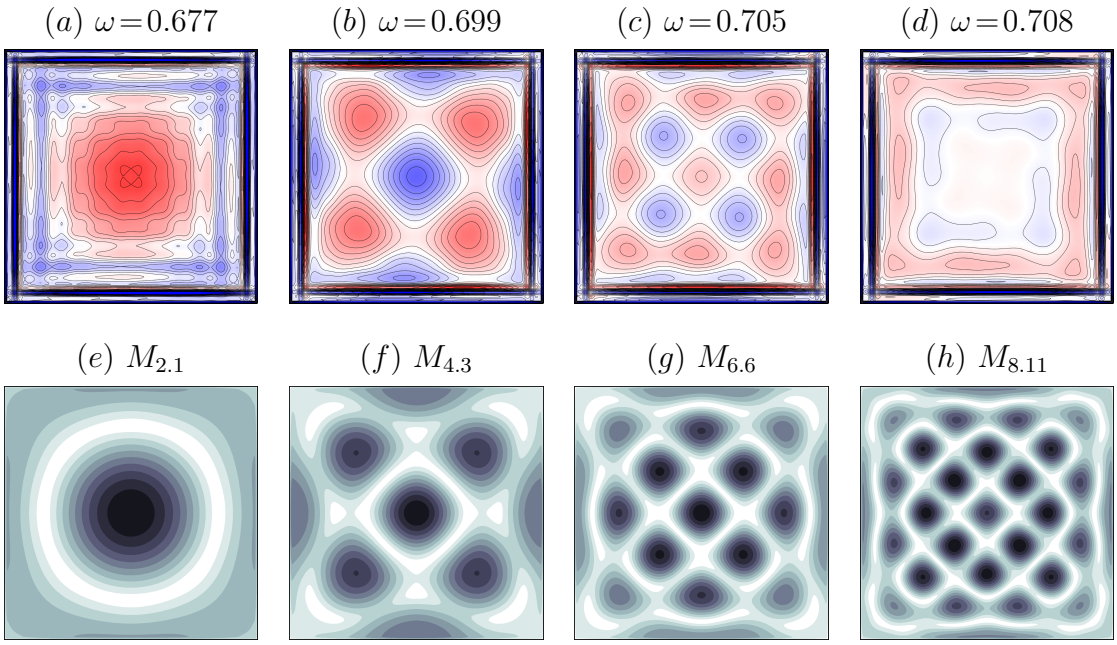

Figure 5.6: Contours of (*a*–*d*) ω_x in the horizontal plane $z=0.45$ at the phase $\varphi=\pi/2$, for $(E,\epsilon)=(10^{-6},10^{-6})$ and ω as indicated, and (*e*–*h*) the normalized amplitude of the ω_z of the inviscid inertial eigenmodes $M_{n.m}$, with n and m as indicated, in a horizontal plane. All contour levels equispaced with $\omega\in[-2.5,2.5]$ for (*a*–*d*). The second row is the first row of the sequence of modes shown in figure D.3.

plane $x=0$ clearly show that the beams originating at the top and bottom edges are not retracing. The beams intersect the $z=0.45$ horizontal plane close to the vertical walls and produce minimal interference with the dominant eigenmode away from the edges. At $\omega=0.699$ the beams are more focused and more intense, and appear to be retracing (see figure 5.5*b*), however the frequency is relatively far from $1/\sqrt{2}$ of the retracing ray $R_{1.1}$. The nonlinear simulations (figures 5.5*b* and 5.6*b*) show the presence of eigenmode $M_{4.3}$ (whose eigenfrequency is 0.6962), featuring a distinct 4×4 cell structure in the vertical plane $x=0$ and an easily identifiable pattern in the $z=0.45$ horizontal cut, which is only mildly affected by the beams; these are more

clearly evident in the animation in movie 3. With the forcing frequency $\omega = 0.705$ being closer to the retracing ray $R_{1.1}$ frequency, the flow is more dominated by the beams and the signature of a dominant eigenmode is harder to identify. The pattern of cells in the vertical plane $x = 0$ in figure 5.5(c) can only be loosely related to the similar cut for eigenmode $M_{6.6}$ in figure 5.5(g) due to the increased interaction between the beams and the smaller sized cells of the eigenmode. Nevertheless, the horizontal cuts in figures 5.6(c, g) provide evidence of the presence of $M_{6.6}$ at that frequency, albeit at a weaker level compared to mode $M_{4.3}$ at frequency $\omega = 0.699$. Also note the aggregation, entrainment and reinforcement of the cell structures in the direction of the beams in figure 5.5(c); this is more apparent in the online movie 4 showing this simulation over one libration period. At $\omega = 0.708$, traces of eigenmodes have almost disappeared from the nonlinear simulations in figures 5.5(d) and 5.6(d), and the flow is completely dominated by the edge beams, with a resonance peak associated to the retracing ray $R_{1.1}$ being predominant in the Σ_H response shown in figures 5.3 and 5.4. For comparison, we have included in figures 5.5(h) and 5.6(h) the next highest mode $M_{8.11}$ from the sequence in figures D.3 and D.6 (in the D), whose eigenfrequency closely matches the forcing frequency, and which might be expected to become more evident at yet smaller values of E. This extrapolation is also supported by the observation that at forcing frequencies $\omega = 0.677$, 0.699, and 0.705 there is evidence in the nonlinear simulations of the near-resonant excitation of the dominant modes $M_{2.1}$, $M_{4.3}$, and $M_{6.6}$, with eigenfrequencies 0.6742, 0.6962, and 0.7022; these all have approximately constant detuning (the difference between forcing frequency and eigenfrequency) of approximately $+0.003$. The movie 5 is also suggestive of the presence of $M_{8.11}$ in the response, but it is highly deformed by the beams.

At the vertical level $z = 0.45$, the eigenmode $M_{4.3}$ in figure 5.5(b) is only weakly perturbed by the beams emanating from the top edges. In order to better understand

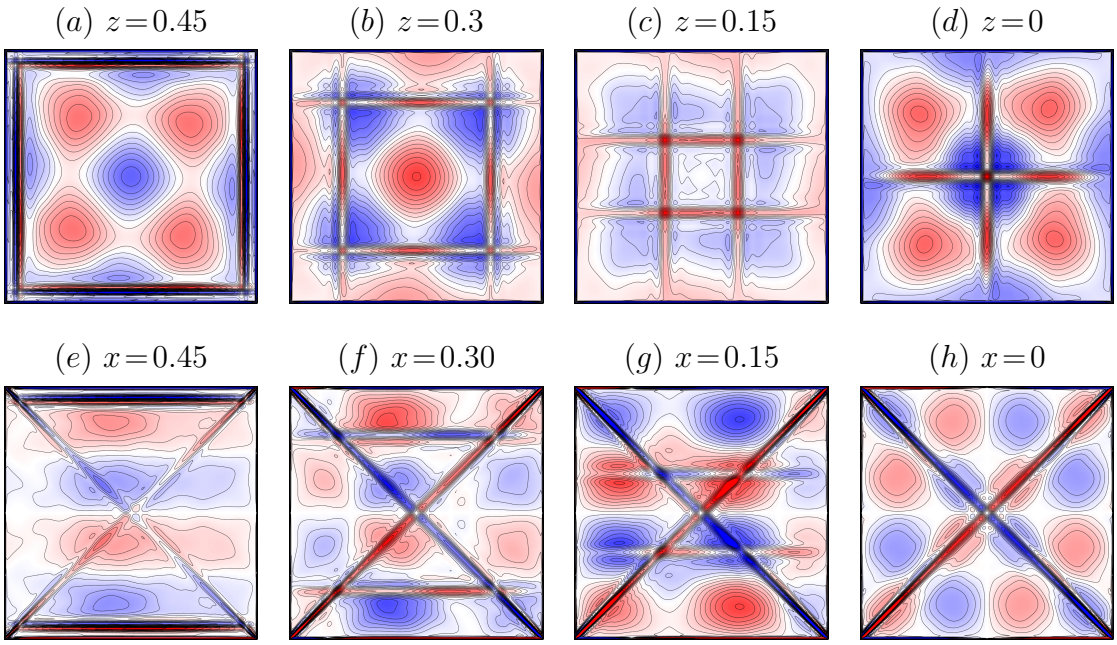

Figure 5.7: Contours of ω_z at the horizontal planes as indicated at $(E,\epsilon)=(10^{-6},10^{-6})$, $\omega=0.699$ and phase $\varphi=\pi/2$. All contour levels are equispaced with $\omega\in[-2.5,2.5]$. See the online movies 6 and 7 for animations over one libration period.

the interaction between the mode and the beams we consider the response at $\omega=0.699$, examining ω_z at different horizontal planes $z=0$, 0.15, 0.30, and 0.45 and ω_x at different vertical planes $x=0.45$, 0.30, 0.15 and 0. These are plotted in figure 5.7, showing the snapshots at the phase $\varphi=\pi/2$. Except for minor deformations due to beam interactions, the structure of the flow in these z-planes retains the overall shape of the eigenmode $M_{4.3}$ (figure 5.6f). The relative strength of the response in the different z-planes is consistent with the dependence of ω_z on z predicted by (D.17). With $n=4$, the factor $\cos n\pi z$ in (D.17) is approximately $(1.00,-0.31,-0.81,0.81)$ at $z=(0.00,0.15,0.30,0.45)$, and explains the relative signs and magnitudes at the various z-levels. In particular, at $z=0.15$ the contribution from the mode is much weaker and hence more susceptible to be deformed or even overpowered by the beams

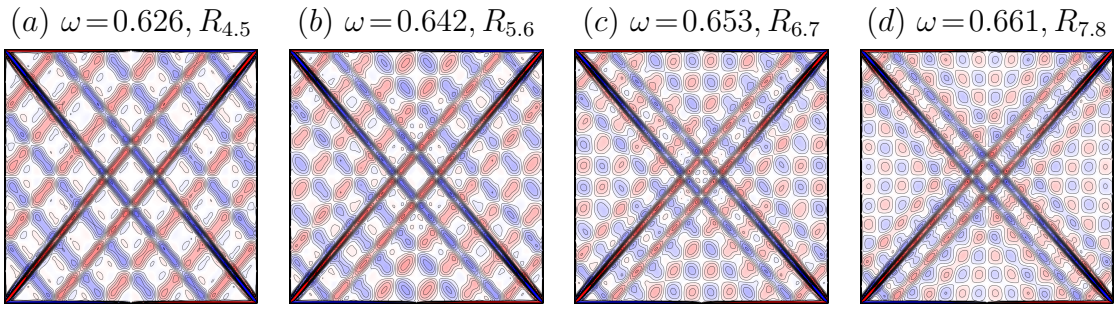

Figure 5.8: Contours of ω_x in the vertical plane $x=0$ for $(E,\epsilon)=(10^{-6},10^{-6})$ and phase $\varphi=\pi/2$ at ω as indicated. All contour levels equispaced with $\omega_x\in[-2.5,2.5]$.

(see figure 5.7c). The plots in vertical x-planes also show the $n=4$ vertical structure of $M_{4.3}$, along with distortions resulting from the nonlinear interactions between the mode and the beams.

While the snapshots in figure 5.7 help identify the presence of the mode $M_{4.3}$ at the different z-levels and x-levels, they do not provide a dynamic account of the impact of the beams on the mode. In movie 6, the animation of mode $M_{4.3}$ in a horizontal plane shows a clockwise progressive wave of cells in the plane, whereas the numerical simulations in the various z-planes show that the beams tend to hinder this progression, pinning and distorting the cells in their vicinity, and confining other cells to a restricted space. For example, the four (red) cells in figure 5.7(c) are confined to their respective quadrant, while the central cell is pinned at the center, with a somewhat distorted structure. On the other hand, the central cell in figure 5.7(a) is unperturbed and free to rotate, while the four (blue) outer cells are pinned by the beams. This differential interaction in different z-planes, which is due to the vertical inclination of the beams, leads to a torsional forcing in the axial (vertical) direction. The dynamic interaction between the beams and mode in the x-planes is depicted in movie 7.

The range $\omega \in [0.6, 0.73]$ also includes a cascade of peaks at the frequencies very close to those of the retracing rays $R_{3.4}$, $R_{4.5}$, $R_{5.6}$, $R_{6.7}$, and $R_{7.8}$ illustrated in figure 5.8. These are indicated in the Σ_H–ω response diagram in figure 5.4. At these frequencies, the flow is more dominated by the edge beams; their retracing contributes to increased phase coherence in the beams. The intensity of these beams and the height of the peaks decrease as the order the beam (the number of reflections on horizontal and vertical walls) increases; the more reflections on the walls the greater the viscous attenuation of the beams in the boundary layers, and the farther they have to travel before reaching an edge, being viscously attenuated along the way.

We now consider the system's response over the broader frequency range. In the range $\omega \in (0, 0.6)$, there is one notable peak at $\omega = 0.434$ in the Σ_V response for $(E, \epsilon) = (10^{-4.6}, 10^{-1.7})$ shown in figure 5.3(a). This peak corresponds to the inviscid inertial mode $M_{2.3}$, with eigenfrequency $\sigma \approx 0.4339$, and whose horizontal structure is shown in figure D.2 and its vertical structure in figure D.5 (these figures are in the D). This frequency is also close to the frequency $\omega \approx 0.4472$ of the retracing ray $R_{1.2}$. There is a smaller bump in the Σ_V response associated to $(E, \epsilon) = (10^{-4.6}, 10^{-1.7})$ at $\omega = 0.312$ corresponding to $M_{2.6}$, whose frequency 0.3115 is also close to the frequency $\omega \approx 0.3162$ of retracing ray $R_{1.3}$. The proximity of these resonant inviscid inertial modes and low-order retracing rays at the relatively large $E = 10^{-4.6}$ results in a broad blended peak. Decreasing E to 10^{-6} separates the contributions of modes and the beams into distinct peaks as the reduced viscous damping both sharpens the peaks and reduces their detuning.

A sequence of peaks corresponding to retracing rays $R_{1.j}$, $j = 9 \to 1$ with increasing ω cumulating at $\omega = 1/\sqrt{2}$ for $R_{1,1}$ is also observed. The intensity of these beams increases with decreasing order j (the number of reflection on the horizontal walls). Figure 5.10 illustrates some of these states.

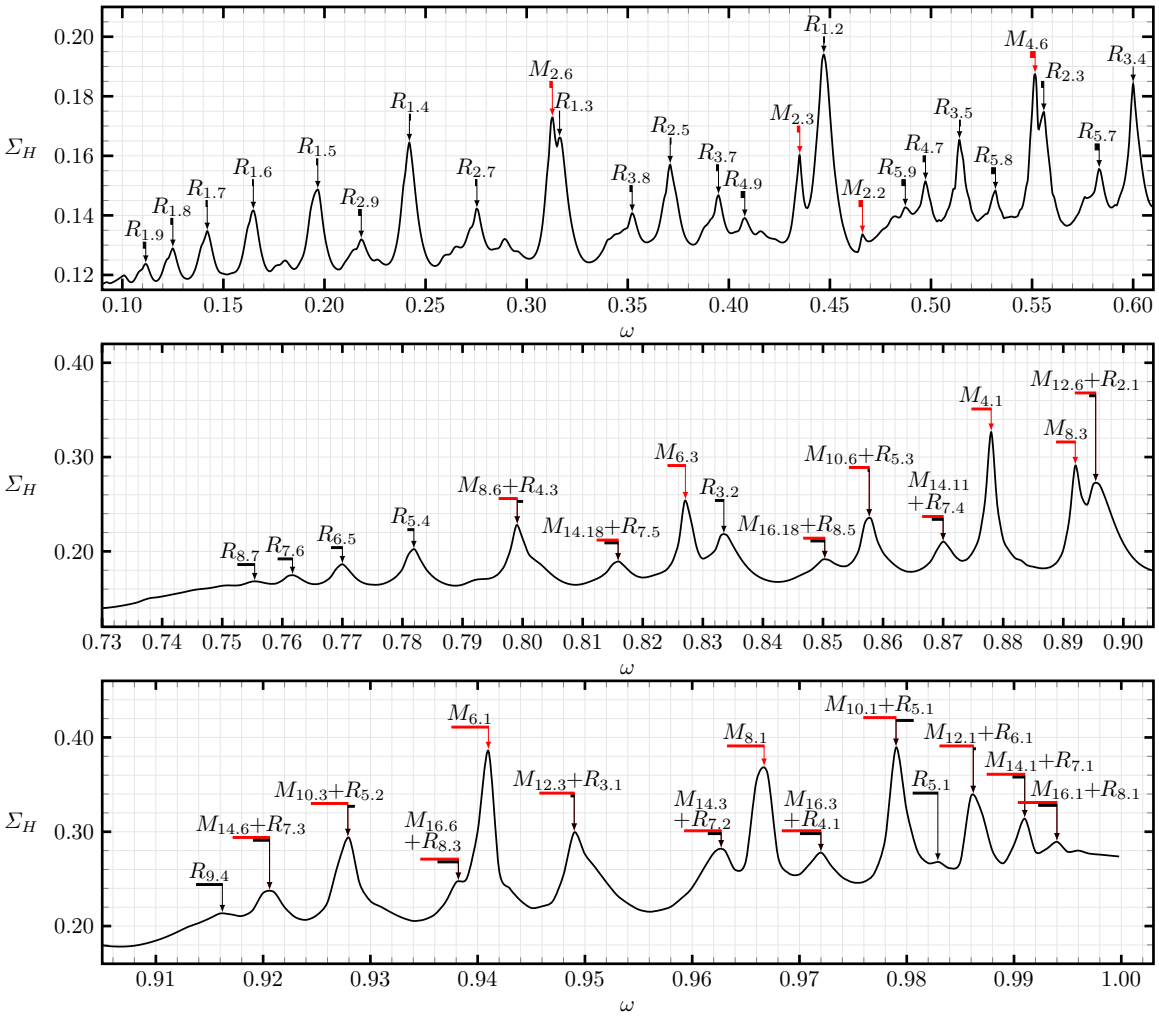

Figure 5.9: Close-ups of the Σ_H–ω response for $(E, \epsilon) = (10^{-6}, 10^{-6})$ shown in figure 5.3, with the major peaks identified, along with the deviation from their nominal frequency (detuning).

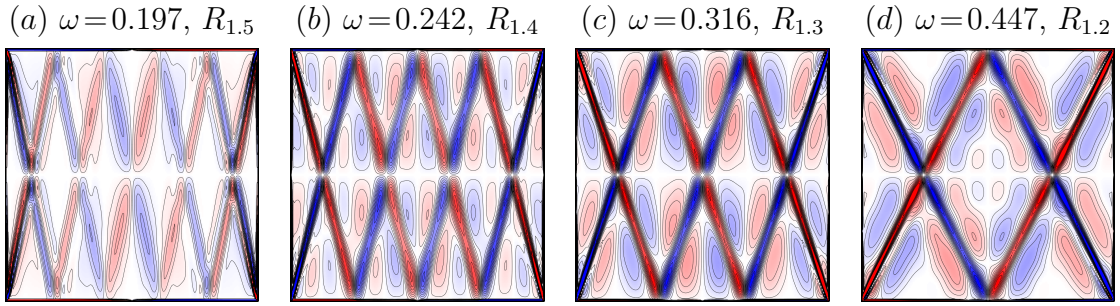

Figure 5.10: Contours of ω_x in the vertical plane $x=0$ for $(E,\epsilon)=(10^{-6},10^{-6})$ at phase $\varphi=\pi/2$ and ω as indicated. All contour levels equispaced with $\omega_x\in[-2.5,2.5]$.

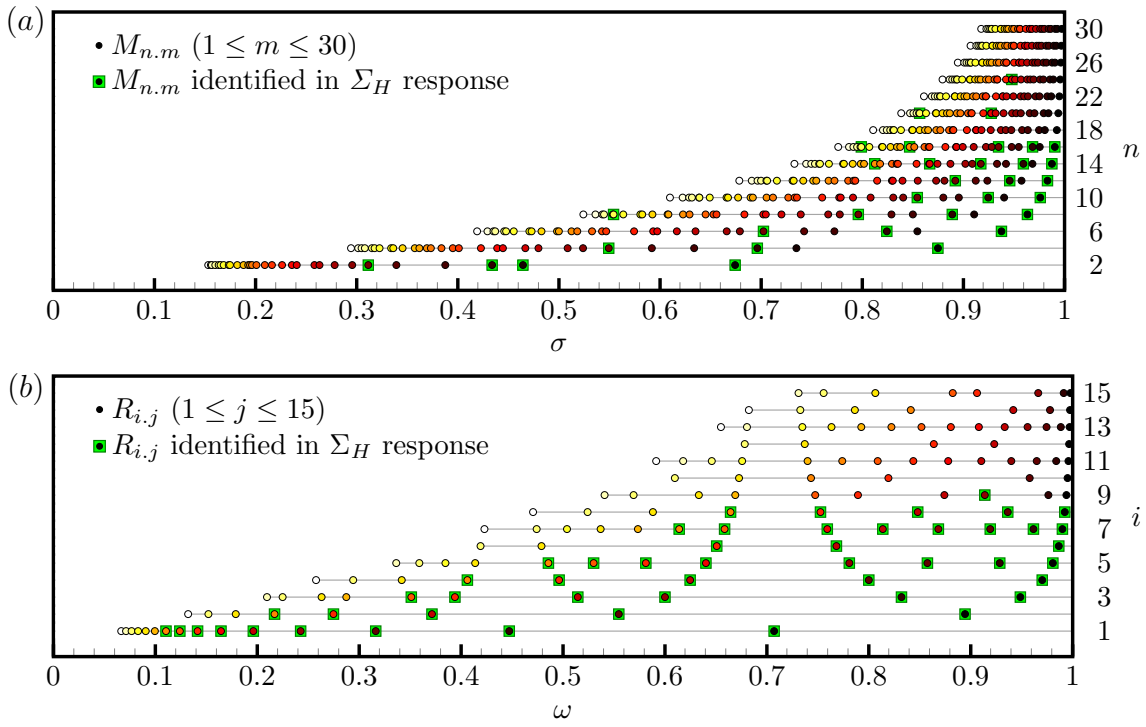

Figure 5.11: (a) Eigenfrequencies σ of the inviscid inertial modes $M_{n.m}$ for $1\le n,m\le 30$ (n even), and (b) frequencies ω of the retracing rays $R_{i.j}$ for $1\le i,j\le 15$.

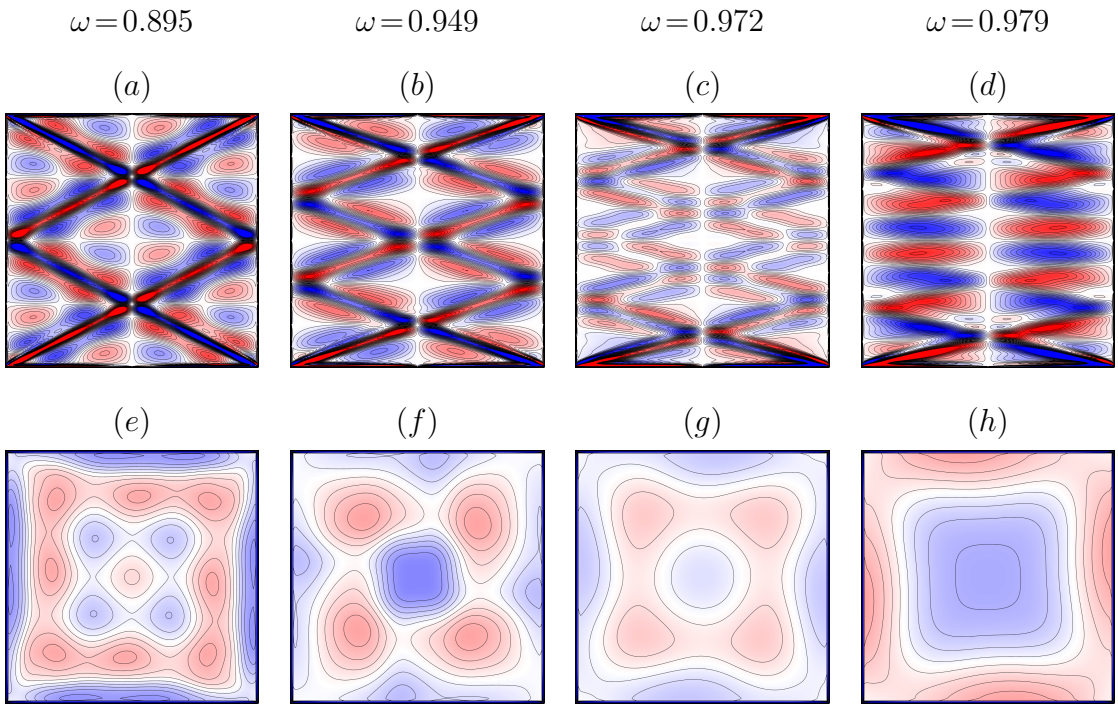

Figure 5.12: Contours of $(a-d)$ ω_x in the vertical plane $x=0$ and $(e-h)$ ω_z in the horizontal plane $z=0$, for $(E,\epsilon)=(10^{-6},10^{-6})$ at phase $\varphi=\pi/2$ and ω as indicated. All contour levels equispaced with $\omega_x \in [-2.5, 2.5]$.

We now turn our attention to the frequency range $\omega \in (0.73, 1)$. For the experimental conditions, $(E,\epsilon)=(10^{-4.6},10^{-1.7})$, the Σ_V response (figure 5.3a) has relatively strong peaks associated to inertial modes $M_{4.1}$ and $M_{6.1}$, and a weaker peak corresponding to $M_{8.1}$. These peaks become more intense and localized for $(E,\epsilon)=(10^{-6},10^{-6})$. A few other minor peaks emerge for $\omega \gtrsim 0.8$, including one near $\omega=0.965$ corresponding to $M_{10.1}$, but the overall response is at or marginally above the background response level. On the other hand, the Σ_H response in figure 5.3(b) reveals an abundance of peaks with increasing power as $\omega \to 1$. The higher peak count in this range of ω corresponds to the higher number of both low-order inertial eigenmodes and retracing rays with frequency close to 1, illustrated in figure 5.11. This figure

also illustrates the absence of either low-order retracing rays or inertial eigenmodes $M_{n.m}$ with $m=1,3,6$ in the vicinity of the $R_{1.1}$ frequency $\omega=1/\sqrt{2}$. The Σ_H response also picks up the sequence of retracing beams $R_{j+1.j}$, $j=7\rightarrow 1$. The response at $\omega=0.799$ shows significant contributions from both $R_{4.3}$ and $M_{8.6}$, and at $\omega=0.896$ the response peak has contributions from both $R_{2.1}$ and $M_{4.3}$. In fact, all major peaks for $\omega\gtrsim 0.8$ consist of contributions from both retracing rays and inertial modes, as illustrated in figure 5.12. For example, figure 5.12(a) clearly shows the presence of $R_{2.1}$ in the ω_x contours in the plane $x=0$ at $\omega=0.895$, with $M_{12.6}$ (more generally of an eigenmode $M_{12.m}$) recognizable in the background, while figure 5.12(e) shows the ω_z structure in the horizontal plane $z=0$ of $M_{12.6}$ (more generally of an eigenmode $M_{n.6}$). In figure 5.12(b), the vertical structure of ω_z at $\omega=0.949$ indicates the strong presence of $R_{3.1}$, while the number of changes of background color close to the median (vertical line $y\approx 0$) together with the plot of ω_z in a horizontal plane in figure 5.12(f) show the presence of eigenmode $M_{12.3}$. As the forcing frequency ω approaches 1, the beams (retracing or not) become increasingly more horizontal and are subject to increasing dissipative interactions with the top and bottom wall boundary layers and many reflections at the sidewalls. As a result, it is more difficult for these beams to retain coherence all the way to the mid-vertical section of the cube, thereby leaving a fairly undisturbed picture of the inertial modes away from the top and bottom endwalls. Figures 5.12(c,g) at $\omega=0.972$, close to the frequencies of $R_{4.1}$ and $M_{16.3}$, and figure 5.12(d,h) at $\omega=0.979$, close to the frequencies of $R_{5.1}$ and $M_{10.1}$, illustrate these effects. The beam $R_{5.1}$ can be better observed with minimal interference from $M_{10.1}$ at $\omega=0.983$. The combination $M_{10.1}+R_{5.1}$ is also the first of a sequence of modes and beams $M_{2i.1}+R_{i.1}$, $i=5,6,7,8$, observed in unison in the Σ_H and the vorticity responses in the range $0.975\lesssim\omega<1$.

Whether an inviscid eigenmode or inertial edge beam, or a combination, is ob-

served in the response at a particular forcing frequency ω depends on the separation between the corresponding natural frequencies of these eigenmodes and beams (these are listed in tables 5.1 and D.1 and illustrated in figure 5.11 for the low-order modes and retracing beams), compared to detuning due to viscous and nonlinear effects. For relatively large $E=10^{-4.6}$ viscous effects spread the influence of the modes and beams over a wide ω-bandwidth, with contributions from both combining to a single peak. This is especially so in the Σ_V response. For example, see the response at $\omega=0.879$, where $M_{4.1}$ and $R_{2.1}$ compete, and $\omega=0.941$, where $M_{6.1}$ and $R_{3.1}$ compete. At smaller Ekman number $E=10^{-6}$ the peaks become sharper, making the distinction between the two contributions possible, especially in the Σ_H response. However, contributions from higher order modes and beams become apparent and the same difficulties repeat on a smaller frequency range, much like what happens when focusing in on a fractal. Still, at $E=10^{-6}$ many modes and beams appear combined into single peaks because of the proximity of their natural frequencies. These typically manifesting themselves during different phases of the librational period or in different cross-sections of the cube. For example, at $E=10^{-6}$, $M_{2i.1}$ appears in the same response with $R_{i.1}$, for $i=5,6,7$, and 8; $M_{2i,3}$ with $R_{i.2}$ for $i=2,5,7$, and 8 (note that $R_{8.2}=R_{4.1}$); $M_{2i.6}$ with $R_{i.3}$ for $i=4,5,7$ and 8; and $M_{2i.18}$ with $R_{i.5}$ for $i=7$ and 8. At certain frequencies multiple eigenmodes were also observed at different phases together with a retracing beam. For example, $M_{4i.11}$ and $M_{2i.3}$ with $R_{i.2}$ at $\omega=0.928$ for $i=5$ and at $\omega=0.949$ for $i=6$, and $M_{4i.25}$ and $M_{2i.6}$ with $R_{i.3}$ at $\omega=0.799$ for $i=4$ and at $\omega=0.858$ for $i=6$. The higher-order eigenmodes (omitted from figure 5.9) can be thought of as spatial (pseudo-)harmonics of the lower-order modes, with slightly different temporal eigenfrequencies, as examplified by figures D.3(c,f) and D.6(c,f). Movie 8 summarizes the response ω_x in the plane $x=0$ at phase $\varphi=\pi/2$ as ω increases from 0.001 to 0.999 with steps of 0.001. It clearly illustrates the vertical structure of the beams, which

are stronger when they are retracing, and at certain peak frequencies the low-order eigenmodes are very predominant. As ω passes through these peaks the change in dominance between beams and modes creates a flashing effect in the movie.

5.6 Discussion and Conclusions

The flow response of a rapidly rotating fluid-filled cube to low-amplitude librational forcing was investigated numerically over the entire range of forcing frequencies supporting inertial waves responses. The enclosed geometry has natural inviscid inertial eigenmodes which the librational forcing can excite resonantly, and in the physical situation governed by the Navier–Stokes equations the resonant response is subject to viscous damping and detuning, and nonlinear saturation. The geometry of the cube and the nature of the librational forcing imparts the system with invariance to $\mathcal{K}_z \times \mathcal{R}_{\pi/2}$ consisting of reflection about the horizontal midplane and rotation of $\pi/2$ about the rotation axis of the cube. The eigenmodes, coming from the Euler equations linearized about the state of solid-body rotation, are invariant to additional symmetries that the Navier–Stokes equations solutions are not as a consequence of the nonlinear terms. For sufficiently low libration amplitudes the Navier–Stokes response flow is invariant to $\mathcal{K}_z \times \mathcal{R}_{\pi/2}$ and only the eigenmodes that are $\mathcal{K}_z \times \mathcal{R}_{\pi/2}$ invariant are resonantly excited. The Navier–Stokes response also consists of internal shear layers, called edge beams as they emerge from edges where the horizontal walls of the cube meet the vertical walls. These are driven by the periodic fluxes in the horizontal wall boundary layers. In the interior they follow the directions of the characteristics of the linear inviscid problem, and reflect off walls preserving these directions. They are thinner and more intense with decreasing Ekman number, and the degree to which the velocity and vorticity vectors align (enhanced helicity) along these beams also increases with decreasing Ekman number. For finite Ekman num-

bers, they are viscously attenuated along their paths and upon wall reflections, and they interact nonlinearly when they cross or are in close proximity. For some libration frequencies, they return to an edge after completing a small number of reflections off the walls. These low-order retracing cases tend to have increased phase coherence.

The eigenmodes and the beams correspond to two different mechanisms: the modes are intrinsic to the geometry of the rotating container, while the beams are extrinsically driven by the details of the body forcing (e.g., libration). In trying to determine what the response to external forcing is due to, the measure used to quantify the response can emphasize different aspects of the response. First and foremost, any measure needs to be of the flow response away from the boundary layers, as most measures are completely swamped by the boundary layer contributions. Many studies Boisson *et al.* [10], Sauret *et al.* [79] use a kinetic energy norm as the measure. The problem is that at the moderate Ekman numbers usually used, the contribution from the beams, regardless of whether they are retracing or not, tend to give a dominant near-constant response throughout the whole frequency range, and only the very lowest-order eigenmodes contribute an additional amount allowing their detection. Other experiments use a probe measuring pressure drop across the container Aldridge and Toomre [4], and this measure is also able to detect resonant responses from low order modes, but not any signal from the internal beams. Other numerical investigations have used a vorticity norm which has been able to detect peak responses from both resonant eigenmodes and retracing beams Lopez and Marques [48], Gutierrez-Castillo and Lopez [25]. Here, we have found that a measure based on the variance in the helicity results in a clear detection of both resonant low-order eigenmodes and retracing beams, and as the Ekman number is reduced, the associated response peaks sharpen and shift in accord with the reduced viscous damping and detuning. The measure utilizes the intrinsic helical nature of the inertial responses.

It is of interest to compare the responses in the librating cube to those in a librating cylinder. The librating cylinder also has responses that consists of eigenmode resonances or phase coherence in retracing beams Gutierrez-Castillo and Lopez [25]. In the cylinder, the Kelvin modes also come with a variety of symmetries, but the symmetry of the librating cylinder Navier–Stokes problem has $\mathcal{K}_z \times SO(2)$ symmetry. The $\mathcal{K}_z$ symmetry is the reflection about the horizontal midplane, as in the librating cube, and $SO(2)$ is the invariance to all rotations about the rotation axis. This continuous symmetry is replace by invariance to a single member, $\mathcal{R}_{\pi/2}$, the invariance to a rotation of $\pi/2$ about the rotation axis for the cube. As in the cube, low-amplitude librational forcing of the cylinder results in flow responses that have the symmetries of the system, and so only the axisymmetric reflection symmetric Kelvin modes are excited in the librating cylinder, just as only the $\mathcal{K}_z \times \mathcal{R}_{\pi/2}$ symmetric eigenmodes are excited in the librating cone. The beams in the librating cylinder are also much simpler. They form axisymmetric cones emanating from the edges where the cylinder endwalls meet the sidewall, whereas in the librating cube, as the beams emerge from straight edges, they form plane shear layers in the interior that intersect orthogonally. Of course, in the cylinder the conical beams also intersect orthogonally. Another difference is that in the librating cylinder, the flow is driven via viscous torque, whereas in the librating cube, since the motion of the vertical walls is not purely in their tangential direction, there is a significant contribution from the pressure torque driving the flow. How this difference manifests in the limit $E \to 0$ between the two geometries would be interesting to explore. This issue has been previously considered for librating spheroids Wu and Roberts [90]. In a very recent study of libration-driven flows in ellipsoidal shells, in which the flow is strongly influenced by the pressure torque associated to the solid boundary motions having a normal component to their motion, Lemasquerier *et al.* [40] conclude: "Thus, the relative importance between

localized shear layers and global inertial modes remains to be clarified, especially when both the forcing and the Ekman number are decreased." The present results provide a systematic study addressing precisely this issue. Although we have used $E=10^{-6}\ll 1$, $\epsilon=10^{-6}\ll 1$, and $\epsilon E^{-1/2}=10^{-3}\ll 1$, the response to librational forcing still has significant viscous damping and detuning (E is still too large for these effects to be negligible) and nonlinear saturation of resonances as well as nonlinear interactions within retracing beams lead to enhanced phase coherence, and in particular, nonlinear interactions between the resonantly excited eigenmodes and the beams (regardless of whether they retrace or not) lead to localized pinning and deformations ($\epsilon E^{-1/2}$ is still too large for nonlinear interactions to be negligible). It is unclear if there is a regime with $E\neq 0$ and $\epsilon\neq 0$ yet both small enough to have negligible viscous and nonlinear effects. On the other hand, it also still remains to be determined for small E how large does ϵ need to be for the synchronous $\mathcal{K}\times\mathcal{R}_{\pi/2}$ forced response to lose stability.

ACKNOWLEDGMENTS

This work was partially supported by National Science Foundation grant CBET-1336410. The computations were performed on the Saguaro Cluster of ASU Research Computing and School of Mathematical and Statistical Sciences computing facilities. The authors thank Jason Yalim for his expertise and valuable help in setting up some of these computations.

Chapter 6

CONCLUSIONS AND FUTURE WORK

6.1 Conclusions

The goal of this dissertation is to develop numerical solvers to solve flows in two-dimensional square and three-dimensional cubic cavities under various setups.

Due to the fact that most of the results included in this dissertation have been published in peer reviewed journals, and the conclusions for each specific configuration are articulated at the end of each chapter. Therefore, in this conclusion chapter, I only emphasize the most critical discoveries.

In the three dimensional lid-driven cavity problem, different flow states were identified in full space and its symmetric subspace. Moreover, the bifurcation diagram was obtained in the symmetric subspace, which provides significant information to explain the bursting behavior of the flow.

In the two dimensional stratified lid-driven cavity case, a wide range of parameters of simulations were done, and the onsets of instabilities of parameters were also identified, and the internal waves were observed too. The results shed light on the directions to the parameters, and the similar behaviors in the three-dimensional stratified lid-driven cavity.

In the libration cavity with the libration axis pointing in vertical direction, the physical mechanisms of resonance were demonstrated. Moreover, the interaction of these two mechanisms were also illustrated visually, with the inertial wave beams pinning and deforming the eigenmode spatio-temporal structure.

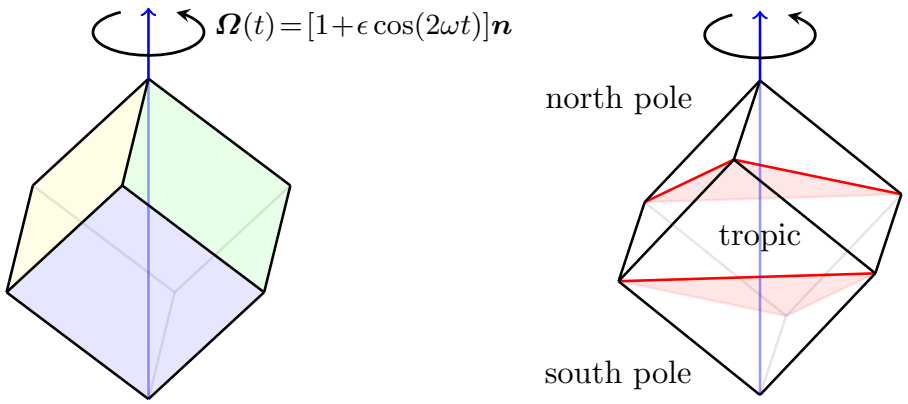

Figure 6.1: Schematic of the librating cube, and the rotation axis vector $\boldsymbol{n}=(1,1,1)/\sqrt{3}$.

6.2 Future Work

6.2.1 Librational Forcing of a Fluid-filled Cube Rapidly Rotating about a Diagonal Axis

In Chapter 5, the cube is librated in the direction $n=(0,0,1)$, and a subset of eigenmodes of the cube is excited. It might be interesting to consider that if the cube is librated in other directions because we want to know whether or not the same flow behaviors would happen under this configuration, such as excitation of eigenmodes and retracing rays. For instance, we choose the librating axis in the direction $\boldsymbol{n}=(1,1,1)/\sqrt{3}$, see figure 6.1. The governing equations and the boundary conditions are exactly the same as the case in Chapter 5, the non-dimensional governing equations are:

$$\frac{\partial \boldsymbol{u}}{\partial t}+\boldsymbol{u}\cdot\boldsymbol{\nabla}\boldsymbol{u}+2\boldsymbol{\Omega}\times\boldsymbol{u}+\frac{d\boldsymbol{\Omega}}{dt}\times\boldsymbol{x}=-\boldsymbol{\nabla}p+E\nabla^2\boldsymbol{u},\quad \boldsymbol{\nabla}\cdot\boldsymbol{u}=0, \tag{6.1}$$

where $E=\nu/\Omega_0 L^2$ is the Ekman number. In the cube frame of reference, the no-slip boundary conditions are $\boldsymbol{u}=\boldsymbol{0}$ on all six walls of the cube. The non-dimensional angular velocity is

$$\boldsymbol{\Omega}(t)=[1+\epsilon\cos(2\omega t)]\,\boldsymbol{n}\,,\quad \boldsymbol{n}=\frac{(1,1,1)}{\sqrt{3}}, \tag{6.2}$$

note that in Chapter 5, $\boldsymbol{\Omega}$ only has z component, but in this configuration, $\boldsymbol{\Omega}$ has all three components. We conducted the simulations at $(E, \epsilon) = (10^{-7}, 10^{-7})$ and $\omega \in (0, 1)$. The responses are quantified by the global enstrophy defined in equation (6.3).

$$\Sigma_V = \frac{1}{\tau} \int_0^\tau \int_{\mathcal{V}} |\boldsymbol{\nabla} \times \boldsymbol{u}|^2 \, d\mathcal{V} \, dt. \tag{6.3}$$

Some of the preliminary results are obtained, and Figure 6.2 (a) presents the global enstrophy response without clipping Σ_V, defined in equation 6.3, with respect to the libration frequency ω at $(E, \epsilon) = (10^{-7}, 10^{-7})$. The green curve represents the enstrophy in the entire volume, the blue curve represents the enstrophy in the tropic regions of the cube, and the yellow curve represents the enstrophy in the poles. The geometric regions of poles and tropic are visually defined Figure 6.1. When the libration frequency $\omega \in (0, 0.58)$, the green curve and blue curve are almost overlapping with each other, which indicates that at this frequency range, the flow tends to concentrate towards the tropic regions; for $\omega \in (0.58, 1)$, the green curve and yellow curve are almost overlapping with each other, which indicates that at this frequency range, the flow tend to concentrate towards the north and the south poles. Figure 6.2 (b) shows the responses of clipped global enstrophy with respect to the libration frequency $\omega \in (0, 1)$. This response diagram qualitatively shows that at any libration frequency $\omega \in (0, 1)$, at the vicinity of center of the cube, the flow moves at a constant rate. Figure 6.3 shows the contours of the enstrophy on the surfaces of the cube at different libration frequencies. The view angle is from the top of the rotation axis. The contours visually show that for $\omega \in (0, 0.58)$, the flow tends to concentrate on the corners and edges not attached with the rotation axis; for $\omega \in (0.58, 1)$, the flow tends to focus on the corners attached with the rotation axis. The exact flow structures inside the cube are currently under investigation.

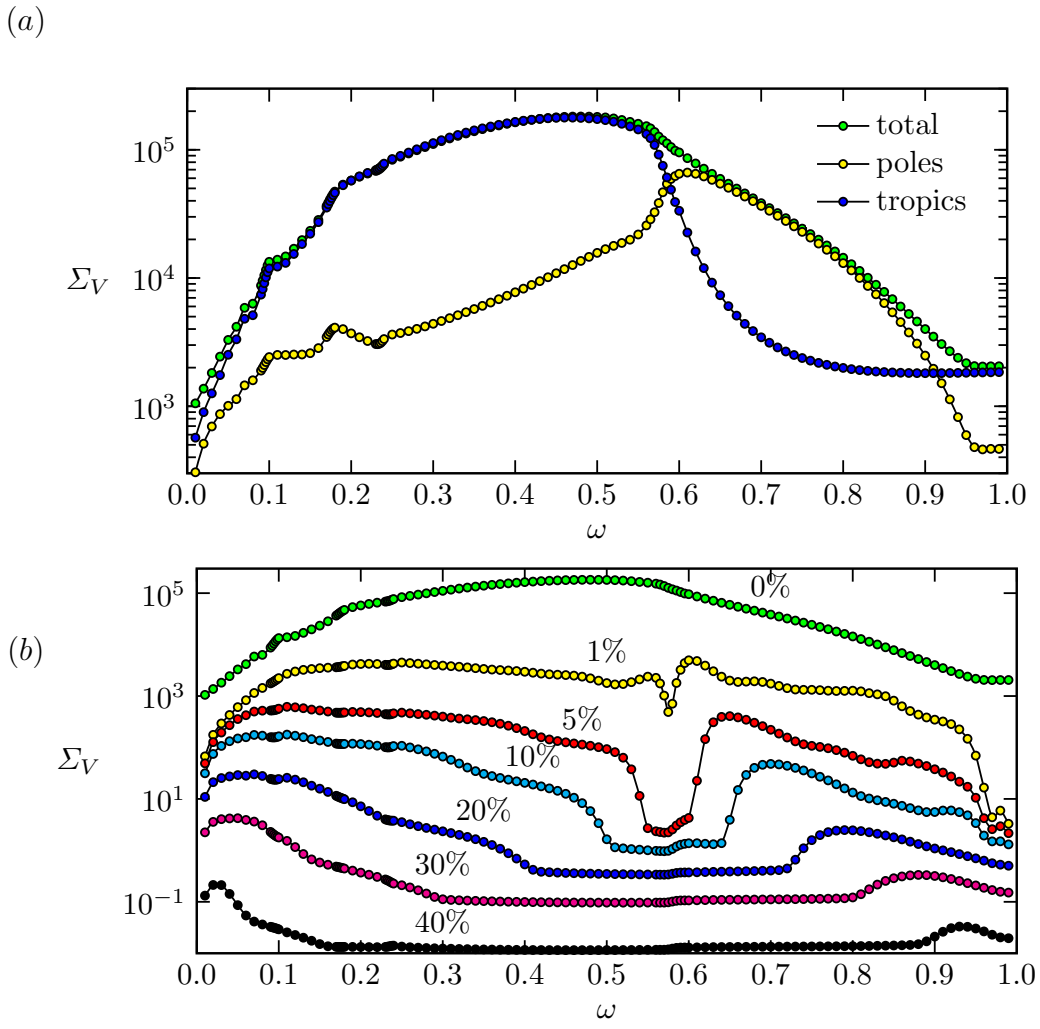

Figure 6.2: Global enstrophy response Σ_V vs. ω for $E = 10^{-7}$ and $\epsilon = 10^{-7}$. The numbers above each curve represent the number of percentage of side length in each dimension clipped away from each boundary when the global enstrophy is computed.

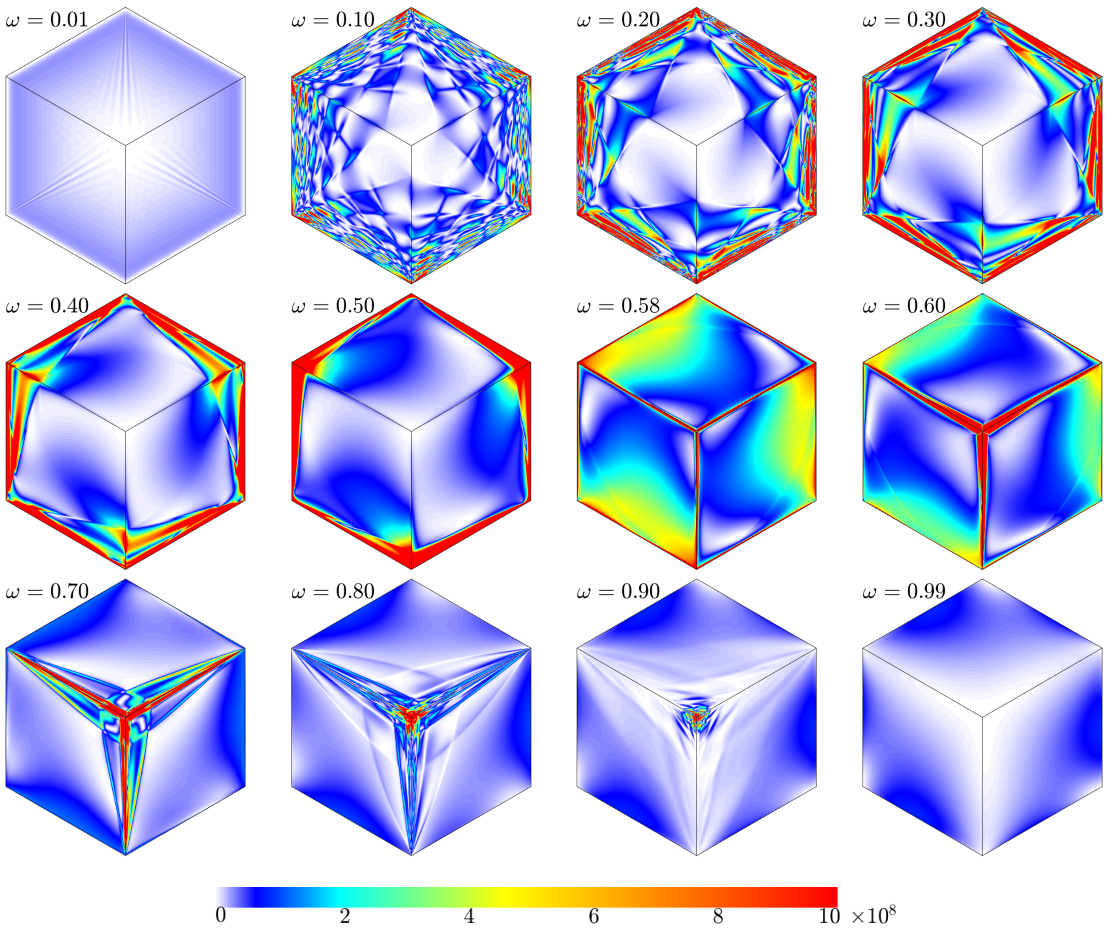

Figure 6.3: Contours of enstrophy on the surfaces of the cube at different ω values as indicated at the phase π. The colormap ranges from enstrophy $|\boldsymbol{\nabla} \times \boldsymbol{u}|^2 = 0$ (white) to 10^8 (red).

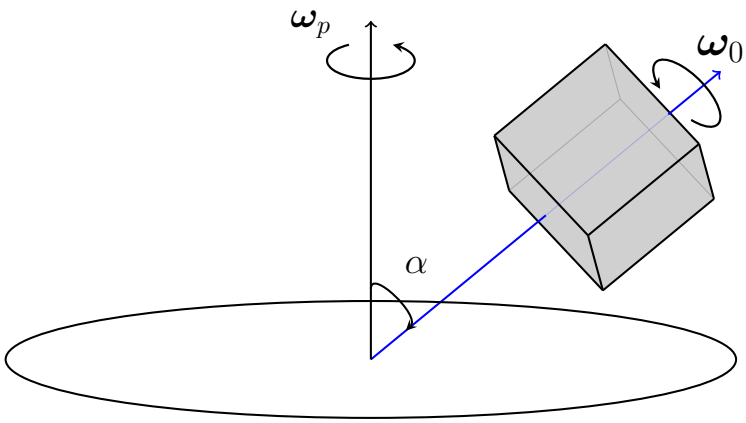

Figure 6.4: Schematic of the precession cube.

6.2.2 Weak Precessional Forcing of a Rapidly Rotating Fluid-filled Cube

In Chapter 5, only a subset of eigenmodes of the cube is excited, and the symmetry of those modes is consistent with the symmetry of the forcing. If we force the cube in other approaches, we want to know whether or not other eigenmodes of the cube can also be resonantly excited. Here we consider the precessional forcing. The cube is mounted at the center of a horizontal table that rotates with angular velocity Ω_p pointing in the vertical direction, and the cube rotates with angular velocity Ω_0 about its axis; the cube axis is tilted at an angle α relative to the vertical, and is at rest relative to the table. A schematic of the set-up is shown in Figure 6.4. There are three independent non-dimensional parameters govering the flow:

$$\begin{aligned} &\text{Cube rotation rate} && \omega_0 = \Omega_0 L^2/\nu, \\ &\text{Precession rate} && \omega_p = \Omega_p L^2/\nu, \\ &\text{Tilt angle} && \alpha. \end{aligned} \tag{6.4}$$

Choose the cube as the reference frame, the governing equations are:

$$\partial \boldsymbol{u}/\partial t + (\boldsymbol{u}\cdot\nabla)\boldsymbol{u} + 2(\boldsymbol{\omega}\times\boldsymbol{u}) + \partial\boldsymbol{\omega}/\partial t \times \boldsymbol{r} = -\nabla p + \nabla^2\boldsymbol{u}, \qquad \nabla\cdot\boldsymbol{u} = 0, \tag{6.5}$$

the boundary conditions are trivial $\boldsymbol{u}=\mathbf{0}$. The governing equations are the same as in Chapter 5, the only difference is still the body force. In this scenario, the body force is:

$$\boldsymbol{\omega}=\omega_p \sin\alpha(\cos\omega_0 t\,\widehat{\boldsymbol{x}}+\sin\omega_0 t\,\widehat{\boldsymbol{y}})+(\omega_0+\omega_p\cos\alpha)\widehat{\boldsymbol{z}}. \tag{6.6}$$

The axial component provides the solid-body rotation of the cube around its axis and the angular velocity orthogonal to the axis has modulus

$$a_f=|\omega_p|\sin\alpha, \tag{6.7}$$

providing a measure of the amplitude of the precessional forcing, and rotates about the cube axis with angular frequency ω_0. Note that although the forcing amplitude is independent of the sign of ω_p, the resulting flow is not.

Other non-dimensional parameters can be defined in terms of the three parameters (6.4), and are often used in describing precessing flow:

$$\begin{aligned}
&\text{Poincaré number} && Po=\omega_p/\omega_0,\\
&\text{Reynolds number} && Re=\omega_0+\omega_p\cos\alpha,\\
&\text{Ekman number} && E=1/\omega_0 \text{ or } 1/Re,\\
&\text{Rossby number} && Ro=\omega_p\sin\alpha/(\omega_0+\omega_p\cos\alpha).
\end{aligned} \tag{6.8}$$

With the non-dimensionalization used, the three parameters ω_0, ω_p and α appear in the governing equations only in the body forces via $\boldsymbol{\omega}$ (6.6). The other parameters (6.8) can be determined directly from these.

The ratio between the forcing frequency in the viscous time scale, ω_0, and the axial component of the angular velocity of the cube, $\omega_0+\omega_p\cos\alpha$, gives the linear dispersion relation [24]

$$2\cos\beta=\omega_0/(\omega_0+\omega_p\cos\alpha)=\omega_0/Re=1/(1+Po\cos\alpha)=\omega_f, \tag{6.9}$$

which is the forcing frequency in the inertial time scale, and β is the angle bewteen the wavevector of an inertial wave and the cube axis.

For $\mathcal{A}_f > 0$ the system (6.5) is only invariant to an inversion symmetry

$$\mathcal{I}(u, v, w, p)(x, y, z, t) = (-u, -v, -w, p)(-x, -y, -z, t). \tag{6.10}$$

The measurements used to quantify the flow are the global kinetic energy and the global helicity inside the cube.

$$\Sigma_K = \frac{1}{\tau} \int_0^\tau \int_{-0.5}^{0.5} \int_{-0.5}^{0.5} \int_{-0.5}^{0.5} |\boldsymbol{u}|^2 \, dx \, dy \, dz \, dt, \tag{6.11}$$

$$\Sigma_H = \frac{1}{\tau} \int_0^\tau \int_{-0.5}^{0.5} \int_{-0.5}^{0.5} \int_{-0.5}^{0.5} |\boldsymbol{u} \cdot (\boldsymbol{\nabla} \times \boldsymbol{u})|^2 \, dx \, dy \, dz \, dt, \tag{6.12}$$

where $\tau = 2\pi/\omega_0$.

I conducted the simulations at precession angle $\alpha = 1$ degree, and three selected rotation rates $\omega_0 = 10^4, 10^5, 4 \times 10^5$, along with the $Po \in [-0.50, 1.0]$. Some of the preliminary results are obtained.

Multiple peaks appear in the response diagram Figure 6.5. At each peak, the numerical vorticity field amplitdues are visualized on horizontal and vertical cuts, and also the structures of the vorticity field amplitudes are compared with respect to the correspoing eigenmdoes. Figure 6.6 $(a) - (d)$ shows the contours of vorticity field ω_x amplitudes on the vertical plane $x = 0$, and $(e) - (h)$ shows the vorticity field amplitudes of the corresponding eigenmodes on the same plane. Other than the inertial wave beams appear in the DNS solutions, the sturctures of the DNS and eigenmodes are very consitent. Moreover, Figure 6.7 shows the contours of vorticity field ω_z amplitudes on the horizontal plane $z = 1/6$. The structures of the DNS are also consistent with the structures of eigenmodes. Therefore, precessional forcing is also able to excite the eigenmodes of the cube. Unlike the case in Chapter 5,

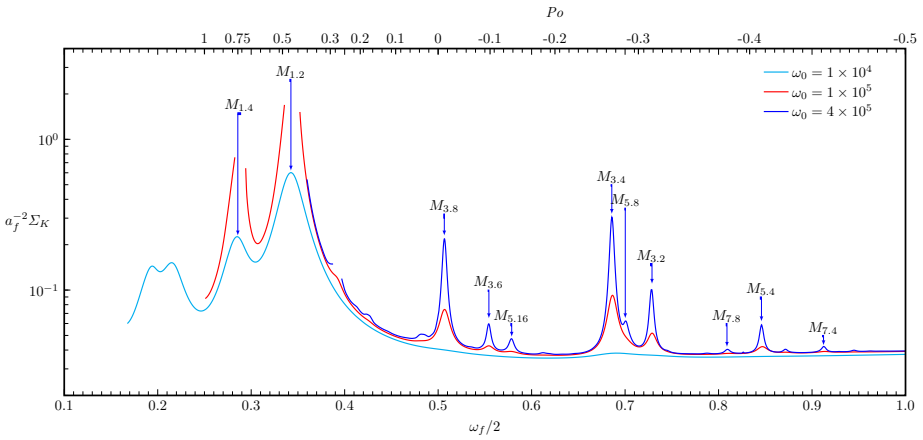

Figure 6.5: Variation of global energy Σ_K, scaled by $a_f^2 = (Po \sin\alpha)^2$ with $Po = \omega_p/\omega_0$ and forcing frequency $\omega_f = 1/(1 + Po\cos\alpha)$, for $\alpha = 1$ degree and ω_0 as indicated.

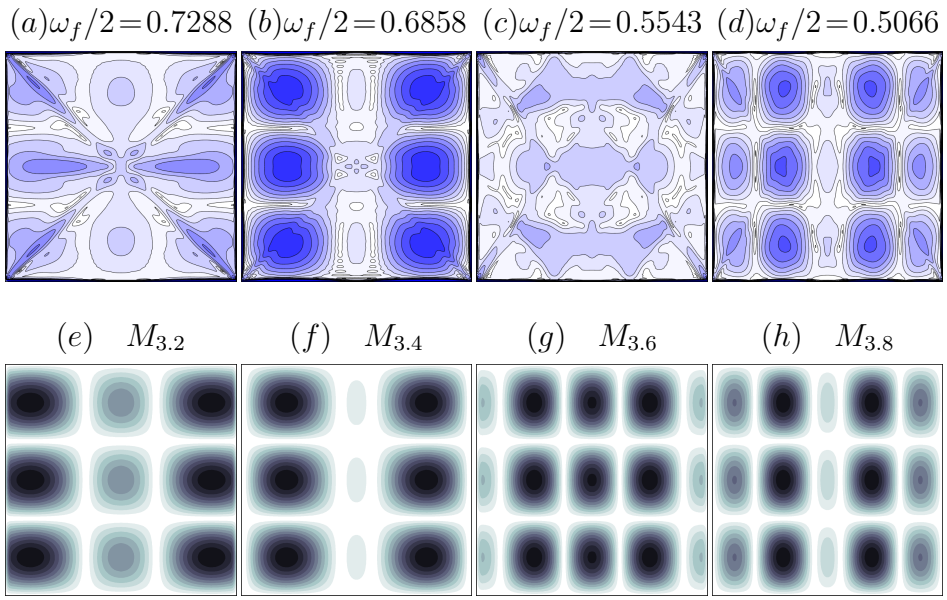

Figure 6.6: $(a) - (d)$ contours of $|\omega_x|$ of DNS in vertical middle plane $x = 0$, and the associated Poincaré numbers are $(a)Po = -0.314$, $(b)Po = -0.271$, $(c)Po = -0.098$, $(d)Po = -0.013$; $(e) - (f)$ contours of $|\omega_x|$ at $x = 0$ for different eigenmodes as indicated.

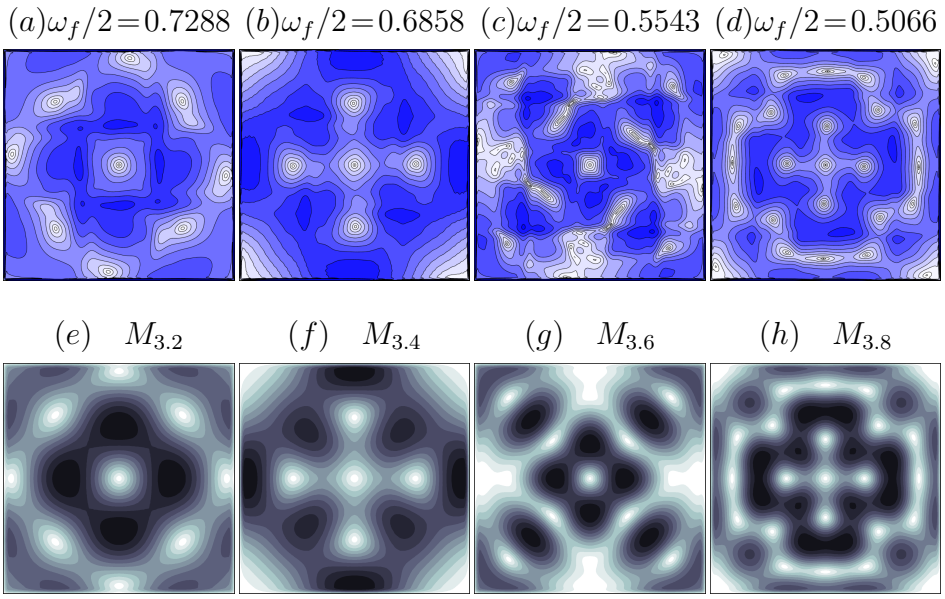

Figure 6.7: $(a)-(d)$ contours of $|\omega_z|$ of DNS in horizontal middle plane $z=1/6$, and the associated Poincaré number and contour levels are $(a)Po=-0.314$, $(b)Po=-0.271$, $(c)Po=-0.098$, $(d)Po=-0.013$; $(e)-(h)$ contours of $|\omega_z|$ at $z=1/6$ for different eigenmodes as indicated.

the modes with odd vertical wave numbers are excited. Moreover, at $\omega_0=1.0\times10^5$ and $Po=0.444$, the DNS solution is not sychronized with the forcing anymore and becomes quasi-periodic. Possibly the instability is due to triadic resonance, and candidate eigenmodes causing the resonance is under investigation.

REFERENCES

[1] Abshagen, J., J. M. Lopez, F. Marques and G. Pfister, "Symmetry breaking via global bifurcations of modulated rotating waves in hydrodynamics", Phys. Rev. Lett. **94**, 074501 (2005).

[2] Abshagen, J., J. M. Lopez, F. Marques and G. Pfister, "Bursting dynamics due to a homoclinic cascade in Taylor–Couette flow", J. Fluid Mech. **613**, 357–384 (2008).

[3] Åkervik, E., L. Brandt, D. S. Henningson, J. Hœpffner, O. Marxen and P. Schlatter, "Steady solutions of the Navier–Stokes equations by selective frequency damping", Phys. Fluids **18**, 068102 (2006).

[4] Aldridge, K. D. and A. Toomre, "Axisymmetric inertial oscillations of a fluid in a rotating spherical container", J. Fluid Mech. **37**, 307–323 (1969).

[5] Ansong, J. K. and B. R. Sutherland, "Internal gravity waves generated by convective plumes", J. Fluid Mech. **648**, 405–434 (2010).

[6] Auteri, F., N. Parolini and L. Quartapelle, "Numerical investigation of the stability of singular driven cavity flow", J. Comput. Phys. **183**, 1–25 (2002).

[7] Blackburn, H. M. and J. M. Lopez, "The onset of three-dimensional standing and modulated travelling waves in a periodically driven cavity flow", J. Fluid Mech. **497**, 289–317 (2003).

[8] Blackburn, H. M., F. Marques and J. M. Lopez, "Symmetry breaking of two-dimensional time-periodic wakes", J. Fluid Mech. **522**, 395–411 (2005).

[9] Blanchette, F., T. Peacock and R. Cousin, "Stability of a stratified fluid with a vertically moving sidewall", J. Fluid Mech. **609**, 305–317 (2008).

[10] Boisson, J., C. Lamriben, L. R. M. Maas, P. P. Cortet and F. Moisy, "Inertial waves and modes excited by the libration of a rotating cube", Phys. Fluids **24**, 076602 (2012).

[11] Boyd, J. P., *Chebyshev and Fourier Spectral Methods* (Dover, 2001), 2 edn.

[12] Boyland, P. L., "Bifurcations of circle maps: Arnol'd tongues, bistability and rotation intervals", Commun. Math. Phys. **106**, 353–381 (1986).

[13] Brezillon, A., G. Girault and J. M. Cadou, "A numerical algorithm coupling a bifurcating indicator and a direct method for the computation of Hopf bifurcation points in fluid mechanics", Computers & Fluids **39**, 1226–1240 (2010).

[14] Cheng, T. S. and W.-H. Liu, "Effect of temperature gradient orientation on the characteristics of mixed convection flow in a lid-driven square cavity", Computers & Fluids **39**, 965–978 (2010).

[15] Cohen, N., A. Eidelman, T. Elperin, N. Kleerin and I. Rogachevskii, "Sheared stably stratified turbulence and large-scale waves in a lid driven cavity", Phys. Fluids **26**, 105106 (2014).

[16] Cortet, P.-P., C. Lamriben and F. Moisy, "Viscous spreading of an inertial wave beam in a rotating fluid", Phys. Fluids **22**, 086603 (2010).

[17] Davidson, P. A., *Turbulence in Rotating, Stratified and Electrically Conducting Fluids* (Cambridge University Press, 2013).

[18] Dohan, K. and B. R. Sutherland, "Internal waves generated from a turbulent mixed region", Phys. Fluids **15**, 488–498 (2003).

[19] Feldman, Y. and A. Y. Gelfgat, "Oscillatory instability of a three-dimensional lid-driven flow in a cube", Phys. Fluids **22**, 093602 (2010).

[20] Fernando, H. J. S., "Turbulent mixing in stratified fluids", Annu. Rev. Fluid Mech. **23**, 455–493 (1991).

[21] Fortin, A., M. Jardak, J. J. Gervais and R. Pierre, "Localization of Hopf bifurcations in fluid flow problems", Intnl J. Num. Meth. Fluids **24**, 1185–1210 (1997).

[22] Goepfert, O. and A. Tilgner, "Dynamos in precessing cubes", New J. Phys. **18**, 103019 (2016).

[23] Gómez, F., R. Gómez and V. Theofilis, "On three-dimensional global linear instability analysis of flows with standard aerodynamics codes", Aerospace Science & Technology **32**, 223–234 (2014).

[24] Greenspan, H. P., *The Theory of Rotating Fluids* (Cambridge University Press, 1968).

[25] Gutierrez-Castillo, P. and J. M. Lopez, "Differentially rotating split-cylinder flow: responses to weak harmonic forcing in the rapid rotation regime", Phys. Rev. Fluids **2**, 084802 (2017).

[26] Hanratty, T. J., E. M. Rosen and R. L. Kabel, "Effect of heat transfer on flow field at low Reynolds numbers in vertical tubes", Ind. Eng. Chem. **50**, 815–818 (1958).

[27] Hugues, S. and A. Randriamampianina, "An improved projection scheme applied to pseudospectral methods for the incompressible Navier–Stokes equations", Intnl J. Num. Meth. Fluids **28**, 501–521 (1998).

[28] Itano, T. and S. Toh, "The dynamics of bursting process in wall turbulence", J. Phys. Soc. Japan **70**, 703–716 (2001).

[29] Ivey, G. N., K. B. Winters and J. R. Koseff, "Density stratification, turbulence, but how much mixing?", Annu. Rev. Fluid Mech. **40**, 169–184 (2008).

[30] Iwatsu, R., J. H. Hyun and K. Kuwahara, "Mixed convection in a driven cavity with a stable vertical temperature gradient", Intnl J. Heat Mass Transfer **36**, 1601–1608 (1993).

[31] Ji, T. H., S. Y. Kim and J. M. Hyun, "Transient mixed convection in an enclosure driven by a sliding lid", Heat Mass Transfer **43**, 629–638 (2007).

[32] Jordi, B. E., C. J. Cotter and S. J. Sherwin, "An adaptive selective frequency damping method", Phys. Fluids **27**, 094104 (2015).

[33] Karniadakis, G. E., "High-order splitting methods for the incompressible navier-stokes equations", J. Comput. Phys. **97**, 414–443 (1991).

[34] Lord Kelvin, "Vibrations of a columnar vortex", Phil. Mag. **10**, 155–168 (1880).

[35] Knobloch, E. and M. R. E. Proctor, "The double Hopf bifurcation with 2:1 resonance", Proc. Roy. Soc. Lond. A **415**, 61–90 (1988).

[36] Koseff, J. R. and R. L. Street, "Circulation structure in a stratified cavity flow", J. Hydraulic Engrg. **111**, 334–354 (1985).

[37] Kuhlmann, H. C. and S. Albensoeder, "Stability of the steady three-dimensional lid-driven flow in a cube and the supercritical flow dynamics", Phys. Fluids **26**, 024104 (2014).

[38] Kuznetsov, Y. A., *Elements of Applied Bifurcation Theory* (Springer, 2004), third edn.

[39] Le Bars, M., D. Cebron and P. Le Gal, "Flows driven by libration, precession, and tides", Annu. Rev. Fluid Mech. **47**, 163–193 (2015).

[40] Lemasquerier, D., A. M. Grannan, J. Vidal, D. Cébron, B. Favier, M. Le Bars and J. M. Aurnou, "Libration-driven flows in ellipsoidal shells", J. Geophys. Res. Planets **122**, 1926–1950 (2017).

[41] Leung, J. J. F., A. H. Hirsa, H. M. Blackburn, F. Marques and J. M. Lopez, "Three-dimensional modes in a periodically driven elongated cavity", Phys. Rev. E **71**, 026305 (2005).

[42] Liberzon, A., Y. Feldman and A. Y. Gelfgat, "Experimental observation of the steady-oscillatory transition in a cubic lid-driven cavity", Phys. Fluids **23**, 084106 (2011).

[43] Loiseau, J.-C., *Dynamics and Global Analyses of Three-Dimensional Flows*, Ph.D. thesis, Paris Institute of Technology (2014).

[44] Loiseau, J.-C., J.-C. Robinet and E. Leriche, "Intermittency and transition to chaos in the cubical lid-driven cavity flow", Fluid Dynam. Res. **48**, 061421 (2016).

[45] Lopez, J. M. and F. Marques, "Small aspect ratio Taylor-Couette flow: Onset of a very-low-frequency three-torus state", Phys. Rev. E **68**, 036302 (2003).

[46] Lopez, J. M. and F. Marques, "Finite aspect ratio Taylor-Couette flow: Shil'nikov dynamics of 2-tori", Physica D **211**, 168–191 (2005).

[47] Lopez, J. M. and F. Marques, "Centrifugal effects in rotating convection: nonlinear dynamics", J. Fluid Mech. **628**, 269–297 (2009).

[48] Lopez, J. M. and F. Marques, "Rapidly rotating cylinder flow with an oscillating sidewall", Phys. Rev. E **89**, 013013 (2014).

[49] Lopez, J. M. and F. Marques, "Nonlinear and detuning effects of the nutation angle in precessionally-forced rotating cylinder flow", Phys. Rev. Fluids **1**, 023602 (2016).

[50] Lopez, J. M. and J. Shen, "An efficient spectral-projection method for the Navier-Stokes equations in cylindrical geometries I. Axisymmetric cases", J. Comput. Phys. **139**, 308–326 (1998).

[51] Lopez, J. M., B. D. Welfert, K. Wu and J. Yalim, see Supplemental Material at `https://journals.aps.org/prfluids/supplemental/10.1103/PhysRevFluids.2.074401` for an animation corresponding to Fig. 3.4. (2017).

[52] Lopez, J. M., B. D. Welfert, K. Wu and J. Yalim, see Supplemental Material at `https://journals.aps.org/prfluids/supplemental/10.1103/PhysRevFluids.2.074401` for an animation corresponding to Fig. 3.5. (2017).

[53] Lopez, J. M., B. D. Welfert, K. Wu and J. Yalim, see Supplemental Material at `https://journals.aps.org/prfluids/supplemental/10.1103/PhysRevFluids.2.074401` for an animation corresponding to Fig. 3.15. (2017).

[54] Lopez, J. M., B. D. Welfert, K. Wu and J. Yalim, see Supplemental Material at `https://journals.aps.org/prfluids/supplemental/10.1103/PhysRevFluids.2.074401` for an animation corresponding to Fig. 3.20. (2017).

[55] Lopez, J. M., B. D. Welfert, K. Wu and J. Yalim, see Supplemental Material at `https://journals.aps.org/prfluids/supplemental/10.1103/PhysRevFluids.2.074401` for an animation corresponding to Fig. 3.21. (2017).

[56] Lopez, J. M., B. D. Welfert, K. Wu and J. Yalim, see Supplemental Material at `https://journals.aps.org/prfluids/supplemental/10.1103/PhysRevFluids.2.074401` for an animation corresponding to Fig. 3.22. (2017).

[57] Lopez, J. M., B. D. Welftert, K. Wu and J. Yalim, "Transition to complex dynamics in the cubic lid-driven cavity", PRF **2**, 074401 (2017).

[58] Maas, L. R. M., "On the amphidromic structure of inertial waves in a rectangular parallelepiped", Fluid Dynam. Res. **33**, 373–401 (2003).

[59] Maiti, M. K., A. S. Gupta and S. Bhattacharyya, "Stable/unstable stratification in thermosolutal convection in a square cavity", J. Heat Trans. **130**, 122001 (2008).

[60] Majda, A. J. and M. G. Shefter, "Elementary stratified flows with instability at large Richardson number", J. Fluid Mech. **376**, 319–350 (1998).

[61] Majda, A. J. and M. G. Shefter, "Nonlinear instability of elementary stratified flows at large Richardson number", Chaos **10**, 3–27 (2000).

[62] Malkus, W. V. R., "Precession of the Earth as the cause of geomagnetism", Science **160**, 259–264 (1968).

[63] Marques, F., A. Y. Gelfgat and J. M. Lopez, "Tangent double Hopf bifurcation in a differentially rotating cylinder flow", Phys. Rev. E **68**, 016310 (2003).

[64] Marques, F. and J. M. Lopez, "Onset of three-dimensional unsteady states in small aspect-ratio Taylor–Couette flow", J. Fluid Mech. **561**, 255–277 (2006).

[65] Marques, F. and J. M. Lopez, "Precession of a rapidly rotating cylinder flow: traverse through resonance", J. Fluid Mech. **782**, 63–98 (2015).

[66] Marques, F., J. M. Lopez and H. M. Blackburn, "Bifurcations in systems with Z_2 spatio-temporal and $O(2)$ spatial symmetry", Physica D **189**, 247–276 (2004).

[67] Mercader, I., O. Batiste and A. Alonso, "An efficient spectral code for incompressible flows in cylindrical geometries", Computers & Fluids (2010).

[68] Michaelian, M. E., T. Maxworthy and L. G. Redekopp, "The coupling between turbulent, penetrative convection and internal waves", Eur. J. Mech. B-Fluids **21**, 1–28 (2002).

[69] Munroe, J. R. and B. R. Sutherland, "Internal wave energy radiated from a turbulent mixed layer", Phys. Fluids **26**, 096604 (2014).

[70] Nicolás, A. and B. Bermúdez, "2D thermal/isothermal incompressible viscous flows", Intnl J. Num. Meth. Fluids **48**, 349–366 (2005).

[71] Noir, J., F. Hemmerlin, J. Wicht, S. M. Baca and J. M. Aurnou, "An experimental and numerical study of librationally driven flow in planetary cores and subsurface oceans", Phys. Earth Planetary Int. **173**, 141–152 (2009).

[72] Nurijanyan, S., O. Bokhove and L. R. M. Maas, "A new semi-analytical solution for inertial waves in a rectangular parallelepiped", Phys. Fluids **25**, 126601 (2013).

[73] Peltier, W. R. and C. P. Caulfield, "Mixing efficiency in stratified shear flows", Annu. Rev. Fluid Mech. **35**, 135–167 (2003).

[74] Peyret, R., *Spectral methods for incompressible viscous flow* (Springer-Verlag, 2002).

[75] Pham, H. T., S. Sarkar and K. A. Brucker, "Dynamics of a stratified shear layer above a region of uniform stratification", J. Fluid Mech. **630**, 191–223 (2009).

[76] Poliashenko, M. and C. K. Aidun, "A direct method for computation of simple bifurcations", J. Comput. Phys. **121**, 246–260 (1995).

[77] Rao, D., "Free gravitational oscillations in rotating rectangular basins", J. Fluid Mech. **25**, 523–555 (1966).

[78] Saad, Y., *Numerical Methods for Large Eigenvalue Problems* (SIAM, 2011), 2 edn.

[79] Sauret, A., D. Cébron, M. Le Bars and S. Le Dizés, "Fluid flows in a librating cylinder", Phys. Fluids **24**, 026603 (2012).

[80] Schneider, T. M., J. F. Gibson, M. Lagha, F. De Lillo and B. Eckhardt, "Laminar-turbulent boundary in plane Couette flow", Phys. Rev. E **78**, 037301 (2008).

[81] Shankar, P. N. and M. D. Deshpande, "Fluid mechanics in the driven cavity", Annu. Rev. Fluid Mech. **32**, 93–136 (2000).

[82] Sherman, F. S., J. Imberger and G. M. Corcos, "Turbulence and mixing in stably stratified waters", Annu. Rev. Fluid Mech. **10**, 267–288 (1978).

[83] Stevens, C. and J. Imberger, "The initial response of a stratified lake to a surface shear stress", J. Fluid Mech. **312**, 39–66 (1996).

[84] Strogatz, S. H., *Nonlinear Dynamics and Chaos* (Addison-Wesley, 2015), 2 edn.

[85] Tilgner, A., "Precession driven dynamos", Phys. Fluids **17**, 034104 (2005).

[86] Tuckerman, L. S. and D. Barkley, "Bifurcation analysis for timesteppers", in "Numerical Methods for Bifurcation Problems and Large-Scale Dynamical Systems", edited by E. Doedel and L. S. Tuckerman, vol. 119 of *Volumes in Mathematics and its Applications*, pp. 453–466 (Springer, 2000).

[87] Turner, J. S., *Buoyancy Effects in Fluids* (Cambridge Univ. Press, 1979).

[88] Vanel, J.-M., R. Peyret and P. Bontoux, "A pseudo-spectral solution of vorticity-stream function equations using the influence matrix technique", in "Numerical Methods for Fluid Dynamics II", edited by K. W. Morton and M. J. Baines, pp. 463–475 (Clarendon Press Oxford, 1986).

[89] Wood, W. W., "An oscillatory disturbance of rigidly rotating fluid", Proc. Roy. Soc. Lond. A **293**, 181–212 (1966).

[90] Wu, C.-C. and P. H. Roberts, "On a dynamo driven topographically by longitudinal libration", Geophys. Astrophys. Fluid Dyn. **107**, 20–44 (2013).

[91] Wu, k., B. D. . Welfert and J. M. Lopez, see Supplemental Material at `https://www.cambridge.org/core/journals/journal-of-fluid-mechanics/article/complex-dynamics-in-a-stratified-liddriven-square-cavity-flow/`

D9BF5F50711D8950CAA58E2E468630D1#fndtn-supplementary-materials for an animation corresponding to Fig. 4.6. (2018).

[92] Wu, k., B. D. Welfert and J. M. Lopez, see Supplemental Material at https://www.cambridge.org/core/journals/journal-of-fluid-mechanics/article/complex-dynamics-in-a-stratified-liddriven-square-cavity-flow/D9BF5F50711D8950CAA58E2E468630D1#fndtn-supplementary-materials for an animation corresponding to Fig. 4.10 and Fig. 4.11. (2018).

[93] Wu, k., B. D. Welfert and J. M. Lopez, see Supplemental Material at https://www.cambridge.org/core/journals/journal-of-fluid-mechanics/article/complex-dynamics-in-a-stratified-liddriven-square-cavity-flow/D9BF5F50711D8950CAA58E2E468630D1#fndtn-supplementary-materials for an animation corresponding to Fig. 4.19. (2018).

[94] Wu, K., B. D. Welfert and J. M. Lopez, "Librational forcing of a rapidly rotating fluid-filled cube", J. Fluid Mech. **842**, 469–494 (2018).

[95] Wu, K., B. D. Welftert and J. M. Lopez, "Complex dynamics in a stratified lid-driven square cavity flow", JFM **855**, 43–66 (2018).

APPENDIX A

CO-AUTHOR PERMISSIONS

I certify that my co-authors, Dr. Juan M. Lopez, Dr. Bruno D. Welfert and Jason Yalim have given me permission, in writing, to include all material in my PhD dissertation for Chapters 3,4 and 5.

APPENDIX B

NUMERICAL SOLVER

Suppose the chosen geometry is a three-dimensional cavity with length l meter, width w meters, and hight h meters. Use h length scale, the non-dimensional length, width and height is summaried in following table.,

	dimensional variable	non-dimensional variable
length	l meters	l/h
width	w meters	w/h
height	h meters	1
$x*, x$	$[-l/2, l/2]$	$[-l/2h, l/2h]$
$y*, y$	$[-w/2, w/2]$	$[-w/2h, w/2h]$
$z*, z$	$[-h/2, h/2]$	$[-1/2, 1/2]$

$x \in [-\frac{l}{2h}, \frac{l}{2h}]$, $y \in [-\frac{w}{2h}, \frac{w}{2h}]$, $z \in [-\frac{1}{2}, \frac{1}{2}]$. x, y, z are the non-dimensional. The aspect ratio we choose is $l/h = 1$ and $w/h = 1$.

Numerical Method

A pseudospectal collocation-Chebyshev method is implemented, each variable is expanded in the approximation space P_{MNR}, composed of Chebyshev polynomials, T_m, T_n and T_r of degrees less or equal than M, N and R in x, y, z directions.

$$u(x,y,z) = \sum_{m=0}^{M}\sum_{n=0}^{N}\sum_{r=0}^{R} \hat{u}_{mnr} T_m(\frac{2h}{l}x) T_n(2y) T_r(\frac{2h}{w}z) \tag{B.1}$$

$$v(x,y,z) = \sum_{m=0}^{M}\sum_{n=0}^{N}\sum_{r=0}^{R} \hat{v}_{mnr} T_m(\frac{2h}{l}x) T_n(2y) T_r(\frac{2h}{w}z) \tag{B.2}$$

$$w(x,y,z) = \sum_{m=0}^{M}\sum_{n=0}^{N}\sum_{r=0}^{R} \hat{w}_{mnr} T_m(\frac{2h}{l}x) T_n(2y) T_r(\frac{2h}{w}z) \tag{B.3}$$

$$T(x,y,z) = \sum_{m=0}^{M}\sum_{n=0}^{N}\sum_{r=0}^{R} \hat{T}_{mnr} T_m(\frac{2h}{l}x) T_n(2y) T_r(\frac{2h}{w}z)) \tag{B.4}$$

$$p(x,y,z) = \sum_{m=0}^{M}\sum_{n=0}^{N}\sum_{r=0}^{R} \hat{p}_{mnr} T_m(\frac{2h}{l}x) T_n(2y) T_r(\frac{2h}{w}z)) \tag{B.5}$$

All the partial derivatives are evaluated directly by the Chebyshev differentiation matrix. Since the computational domain is $[-1/2, -1/2]^3$, when we take partial derivatives by using Chebyshev differentiation matrix, we need to use chain rule, for instance

$$(\frac{\partial u}{\partial x})_{i,j,k} = \frac{2h}{l}(Du)_{i,j,k} \tag{B.6}$$

$$(\frac{\partial^2 u}{\partial x^2})_{i,j,k} = (\frac{2h}{l})^2(D^2u)_{i,j,k} \tag{B.7}$$

Since we use the Chebyshev collocation method, so all the values are directly evaluated at the Chebyshev-Gauss-Lobatto collocation points. Also note that since the aspect ratio we choose is 1 for both length and width, so there is a factor of $\frac{2h}{l}$ when we take the first partial derivative, and there is a factor of $(\frac{2h}{l})^2$ when we take the second partial derivative.

Temporal scheme:

$$\frac{3\boldsymbol{u}^{n+1} - 4\boldsymbol{u}^n + \boldsymbol{u}^{n-1}}{2\delta t} = -\nabla p^{n+1} - 2NL(\boldsymbol{u}^n) + NL(\boldsymbol{u}^{n-1}) - \triangle \boldsymbol{u}^{n+1} - \frac{d\boldsymbol{\Omega}^{n+1}}{dt} \times \boldsymbol{r} \tag{B.8}$$

The time integration used is second order accurate and is based on a combination of Adams-Bashforth and backward differentiation formula (AB/BDF2) schemes.
In order to improve the stability, the viscous term need to be written as

$$NL(\boldsymbol{u}) = (\boldsymbol{u} \cdot \nabla)\boldsymbol{u} + 2(\Omega \times \boldsymbol{u}) \tag{B.9}$$

$$L(\boldsymbol{u}) = \Delta \boldsymbol{u} = \nabla(\nabla \cdot \boldsymbol{u}) - \nabla \times (\nabla \times \boldsymbol{u}) = -\nabla \times (\nabla \times \boldsymbol{u}) \tag{B.10}$$

Write in component form:

$$L(u) = \frac{\partial^2 u}{\partial y^2} + \frac{\partial^2 u}{\partial z^2} - \frac{\partial^2 v}{\partial y \partial x} - \frac{\partial^2 w}{\partial z \partial x} \tag{B.11}$$

$$L(v) = \frac{\partial^2 v}{\partial x^2} + \frac{\partial^2 v}{\partial z^2} - \frac{\partial^2 u}{\partial x \partial y} - \frac{\partial^2 w}{\partial z \partial y} \tag{B.12}$$

$$L(w) = \frac{\partial^2 w}{\partial x^2} + \frac{\partial^2 w}{\partial y^2} - \frac{\partial^2 u}{\partial x \partial z} - \frac{\partial^2 v}{\partial y \partial z} \tag{B.13}$$

Which is due to divergence free, let $\Omega = (\Omega_x, \Omega_y, \Omega_z)$.

$$\Omega \times \boldsymbol{u} = (w\Omega_y - v\Omega_z, u\Omega_z - w\Omega_x, v\Omega_x - u\Omega_y) \tag{B.14}$$

$$\frac{d\Omega}{dt} \times \boldsymbol{r} = (z\frac{d\Omega_y}{dt} - y\frac{d\Omega_z}{dt}, x\frac{d\Omega_z}{dt} - z\frac{d\Omega_x}{dt}, y\frac{d\Omega_x}{dt} - x\frac{d\Omega_y}{dt}) \tag{B.15}$$

Code Implementation

Every quantity is evaluated directly on the Chebyshev-Gauss-Lobatto grid points. Let DX,DY,DZ denote the Chebyshev differentiation matrix with dimension $(M+1)^2, (N+1)^2, (R+1)^2$, and use i, j, k to denote the indices start from 0 to M, N, R respectively. In the code, define $U(0\!:\!M, 0\!:\!N, 0\!:\!R), V(0\!:\!M, 0\!:\!N, 0\!:\!R), W(0\!:\!M, 0\!:\!N, 0\!:\!R), P(0\!:\!M, 0\!:\!N, 0\!:\!R)$ as the velocity and pressure variables, $NLu(0\!:\!M, 0\!:\!N, 0\!:$

$R), NLv(0:M, 0:N, 0:R)$ and $NLw(0:M, 0:N, 0:R)$ as the nonlinear terms in momentum equation, $Lu(0:M, 0:N, 0:R), Lv(0:M, 0:N, 0:R)$ and $Lw(0:M, 0:N, 0:R)$ as the viscous terms in the momentum equation. The partial derivatives can be evaluated direct matrices multiplications, for instance:

$$U_x = \frac{\partial u}{\partial x}(:, :, k) = asp1 * DXU(:, :, k) \tag{B.16}$$

$$U_y = \frac{\partial u}{\partial y}(:, :, k) = asp2 * U(:, :, k)DY^T \tag{B.17}$$

$$U_x = \frac{\partial u}{\partial x}(i, :, :) = 2 * U(i, :, :)DZ^T \tag{B.18}$$

$$\begin{aligned} NLu &= (u\frac{\partial u}{\partial x}) + (v\frac{\partial u}{\partial y}) + (w\frac{\partial u}{\partial z}) + 2(W\Omega_y) - 2(V\Omega_z) \\ &= UU_x + VU_y + WU_z + 2W\Omega_y - 2V\Omega_z \end{aligned} \tag{B.19}$$

$$\begin{aligned} NLv &= (u\frac{\partial v}{\partial x}) + (v\frac{\partial v}{\partial y}) + (w\frac{\partial v}{\partial z}) + 2(U\Omega_z) - 2(W\Omega_x) \\ &= UV_x + VV_y + WV_z + 2U\Omega_z - 2W\Omega_x \end{aligned} \tag{B.20}$$

$$\begin{aligned} NLw &= (u\frac{\partial w}{\partial x}) + (v\frac{\partial w}{\partial y}) + (w\frac{\partial w}{\partial z}) + 2(V\Omega_x) - 2(U\Omega) \\ &= UW_x + VW_y + WW_z + 2V\Omega_x - 2U\Omega_y \end{aligned} \tag{B.21}$$

$$Lu = (\frac{\partial^2 u}{\partial y^2}) + (\frac{\partial^2 u}{\partial z^2}) - (\frac{\partial^2 v}{\partial y \partial x}) - (\frac{\partial^2 w}{\partial z \partial x}) = U_{xx} + U_{zz} - V_{xy} - W_{xz} \tag{B.22}$$

$$Lv = (\frac{\partial^2 v}{\partial x^2}) + (\frac{\partial^2 v}{\partial z^2}) - (\frac{\partial^2 u}{\partial x \partial y}) - (\frac{\partial^2 w}{\partial z \partial y}) = V_{xx} + V_{zz} - U_{yx} - W_{yz} \tag{B.23}$$

$$Lw = (\frac{\partial^2 w}{\partial x^2}) + (\frac{\partial^2 w}{\partial y^2}) - (\frac{\partial^2 u}{\partial x \partial z}) - (\frac{\partial^2 v}{\partial y \partial z}) = W_{xx} + W_{yy} - U_{zx} - V_{zy} \tag{B.24}$$

The Improved Projection Scheme:

step 1: compute the preliminary pressure P^*

$$\triangle p^* = \nabla \cdot \{-2NL(\boldsymbol{u}^n) + NL(\boldsymbol{u}^{n-1}) - \frac{d\boldsymbol{\Omega}^{n+1}}{dt} \times \boldsymbol{r}\} \tag{B.25}$$

with boundary conditions:

$$\frac{\partial p^*}{\partial n} = \boldsymbol{n} \cdot \{\frac{-3\boldsymbol{w} + 4\boldsymbol{u}^n - \boldsymbol{u}^{n-1}}{2\delta t} - 2NL(\boldsymbol{u}^n) + NL(\boldsymbol{u}^{n-1}) + 2L(\boldsymbol{u}^n) - L(\boldsymbol{u}^{n-1}) - \frac{d\boldsymbol{\Omega}^{n+1}}{dt} \times \boldsymbol{r}\} \tag{B.26}$$

where $\boldsymbol{w}$ is the boundary conditions of the velocity field.
Formulation of the linear system:

$$(\frac{\partial^2 p}{\partial x^2})_{i,j,k} + (\frac{\partial^2 p}{\partial y^2})_{i,j,k} + (\frac{\partial^2 p}{\partial z^2})_{i,j,k} = RHS_{i,j,k}$$
$$RHS = \nabla \cdot \{-2NL(\boldsymbol{u}^n) + NL(\boldsymbol{u}^{n-1}) - \frac{d\boldsymbol{\Omega}^{n+1}}{dt} \times \boldsymbol{r}\} \tag{B.27}$$

$$\begin{aligned} RHS = & \\ & asp1 * DX\{-2NL(u^n) + NL(u^{n-1}) - z\frac{d\Omega_y^{n+1}}{dt} + y\frac{d\Omega_z^{n+1}}{dt}\} + \\ & asp2 * DY\{-2NL(v^n) + NL(v^{n-1}) + z\frac{d\Omega_x^{n+1}}{dt} - x\frac{d\Omega_z^{n+1}}{dt}\} + \\ & 2 * DZ\{-2NL(w^n) + NL(w^{n-1}) - y\frac{d\Omega_x^{n+1}}{dt} + x\frac{d\Omega_y^{n+1}}{dt}\} \end{aligned} \tag{B.28}$$

$$\begin{aligned} & \sum_{t=1}^{M-1} DX_{i,t}^2 P_{t,j,k}^* + DX_{i,0}^2 P_{0,j,k}^* + DX_{i,M}^2 P_{M,j,k}^* \\ & + \sum_{t=1}^{N-1} DY_{j,t}^2 P_{i,t,k}^* + DY_{j,0}^2 P_{i,0,k}^* + DY_{j,N}^2 P_{i,N,k}^* \\ & + \sum_{t=1}^{R-1} DZ_{k,t}^2 P_{i,j,t}^* + DZ_{k,0}^2 P_{i,j,0}^* + DZ_{k,R}^2 P_{i,j,R}^* = RHS_{i,j,k} \end{aligned} \tag{B.29}$$

$$
\begin{aligned}
P^*_{0,j,k} = & \frac{\frac{1}{asp1} RHSx_{0,j,k} DX_{MM} - \frac{1}{asp1} RHSx_{M,j,k} DX_{0M}}{DX_{00} DX_{MM} - DX_{0M} DX_{M0}} \\
& - \sum_{t=1}^{M-1} \frac{DX_{MM} DX_{0t} - DX_{0M} DX_{Mt}}{DX_{00} DX_{MM} - DX_{M0} DX_{0M}} P^*_{t,j,k} \\
P^*_{M,j,k} = & \frac{\frac{1}{asp1} RHSx_{0,j,k} DX_{M0} - \frac{1}{asp1} RHSx_{M,j,k} DX_{0M}}{DX_{M0} DX_{0M} - DX_{00} DX_{MM}} \\
& - \sum_{t=1}^{M-1} \frac{DX_{M0} DX_{0t} - DX_{00} DX_{Mt}}{DX_{M0} DX_{0M} - DX_{00} DX_{MM}} P^*_{t,j,k} \\
P^*_{i,0,k} = & \frac{\frac{1}{asp2} RHSy_{i,0,k} DY_{NN} - \frac{1}{2} RHSy_{i,N,k} DY_{0N}}{DY_{00} DY_{NN} - DY_{0N} DY_{N0}} \\
& - \sum_{t=1}^{N-1} \frac{DY_{NN} DY_{0t} - DY_{0N} DY_{Nt}}{DY_{00} DY_{NN} - DY_{N0} DY_{0N}} P^*_{i,t,k} \\
P^*_{i,N,k} = & \frac{\frac{1}{asp2} RHSy_{i,0,k} DY_{N0} - \frac{1}{2} RHSy_{i,N,k} DY_{0N}}{DY_{N0} DY_{0N} - DY_{00} DY_{NN}} \\
& - \sum_{t=1}^{N-1} \frac{DY_{N0} DY_{0t} - DY_{00} DY_{Nt}}{DY_{N0} DY_{0N} - DY_{00} DY_{NN}} P^*_{i,t,k} \\
P^*_{i,j,0} = & \frac{\frac{1}{2} RHSz_{i,j,0} DZ_{RR} - \frac{1}{asp2} RHSz_{i,j,R} DZ_{0R}}{DZ_{RR} DZ_{00} - DZ_{0R} DZ_{R0}} \\
& - \sum_{t=1}^{R-1} \frac{DZ_{RR} DZ_{0t} - DZ_{0R} DZ_{Rt}}{DZ_{RR} DZ_{00} - DZ_{0R} DZ_{R0}} P^*_{i,j,t} \\
P^*_{i,j,R} = & \frac{\frac{1}{2} RHSz_{i,j,0} DZ_{R0} - \frac{1}{asp2} RHSz_{i,j,R} DZ_{00}}{DZ_{R0} DZ_{0R} - DZ_{00} DZ_{RR}} \\
& - \sum_{t=1}^{R-1} \frac{DZ_{R0} DZ_{0t} - DZ_{00} DZ_{Rt}}{DZ_{R0} DZ_{0R} - DZ_{00} DZ_{RR}} P^*_{i,j,t}
\end{aligned}
\tag{B.30}
$$

Plug the boundary p^* values into the Helmhotz equation, the linear system can be written as following:

$$
\begin{aligned}
& asp1^2 * \sum_{t=1}^{M-1} DX_{i,t}^2 P_{t,j,k}^* \\
& \quad - asp1^2 * DX_{i,0}^2 \sum_{t=1}^{M-1} \frac{DX_{MM}DX_{0t} - DX_{0M}DX_{Mt}}{DX_{MM}DX_{00} - DX_{0M}DX_{M0}} P_{t,j,k}^* \\
& \quad - asp1^2 * DX_{i,M}^2 \sum_{t=1}^{M-1} \frac{DX_{M0}DX_{0t} - DX_{00}DX_{Mt}}{DX_{M0}DX_{0M} - DX_{00}DX_{MM}} P_{t,j,k}^* \\
& \quad + asp2^2 * \sum_{t=1}^{N-1} DY_{j,t}^2 P_{i,t,k}^* \\
& \quad - asp2^2 * DY_{j,0}^2 \sum_{t=1}^{N-1} \frac{DY_{NN}DY_{0t} - DY_{0N}DY_{Nt}}{DY_{NN}DY_{00} - DY_{0N}DY_{N0}} P_{i,t,k}^* \\
& \quad - asp2^2 * DY_{j,N}^2 \sum_{t=1}^{N-1} \frac{DY_{N0}DY_{0t} - DY_{00}DY_{Nt}}{DY_{N0}DY_{0N} - DY_{00}DY_{NN}} P_{i,t,k}^* \\
& \quad + 2^2 * \sum_{t=1}^{R-1} DZ_{k,t}^2 P_{i,j,k}^* \\
& \quad - 2^2 * DZ_{k,0}^2 \sum_{t=1}^{R-1} \frac{DZ_{RR}DZ_{0t} - DZ_{0R}DZ_{Rt}}{DZ_{RR}DZ_{00} - DZ_{0R}DZ_{R0}} P_{i,j,t}^* \\
& \quad - 2^2 * DZ_{k,R}^2 \sum_{t=1}^{R-1} \frac{DZ_{R0}DZ_{0t} - DZ_{00}DZ_{Rt}}{DZ_{R0}DZ_{0R} - DZ_{00}DZ_{RR}} P_{i,j,t}^* \\
= & RHS_{i,j,k} - asp1^2 * DX_{i,0}^2 \frac{\frac{1}{asp1} RHSx_{0,j,k} DX_{MM} - \frac{1}{asp1} RHSx_{M,j,k} DX_{0M}}{DX_{MM}DX_{00} - DX_{0M}DX_{M0}} \\
& \quad - asp1^2 * DX_{i,M}^2 \frac{\frac{1}{asp1} RHSx_{0,j,k} DX_{M0} - \frac{1}{asp1} RHSx_{M,j,k} DX_{00}}{DX_{M0}DX_{0M} - DX_{00}DX_{MM}} \\
& \quad - asp2^2 * DY_{j,0}^2 \frac{\frac{1}{asp2} RHSy_{i,0,k} DY_{NN} - \frac{1}{asp2} RHSy_{i,N,k} DY_{0N}}{DY_{NN}DY_{00} - DY_{0N}DY_{N0}} \\
& \quad - asp2^2 * DY_{j,N}^2 \frac{\frac{1}{asp2} RHSy_{i,0,k} DY_{N0} - \frac{1}{asp2} RHSy_{i,N,k} DY_{00}}{DY_{N0}DY_{0N} - DY_{00}DY_{NN}} \\
& \quad - 2^2 * DZ_{k,0}^2 \frac{\frac{1}{2} RHSz_{i,j,0} DZ_{RR} - \frac{1}{2} RHSz_{i,j,R} DZ_{0R}}{DZ_{RR}DZ_{00} - DZ_{0R}DZ_{R0}} \\
& \quad - 2^2 * DZ_{k,R}^2 \frac{\frac{1}{2} RHSz_{i,j,R} DZ_{R0} - \frac{1}{2} RHSz_{i,j,R} DZ_{00}}{DZ_{R0}DZ_{0R} - DZ_{00}DZ_{RR}}
\end{aligned} \tag{B.31}
$$

$$\frac{3\boldsymbol{u}^* - 4\boldsymbol{u}^n + \boldsymbol{u}^{n-1}}{2\delta t} + 2NL(\boldsymbol{u}^n) - NL(\boldsymbol{u}^{n-1}) = -\nabla p^* + \Delta \boldsymbol{u}^* - \frac{d\boldsymbol{\Omega}^{n+1}}{dt} \times \boldsymbol{r} \quad \text{(B.32)}$$

Re-write the above equation and group all the $\boldsymbol{u}^*$ terms.

$$(\Delta - \frac{3}{2\delta t})\boldsymbol{u}^* = \nabla p^* + 2NL(\boldsymbol{u}^n) - NL(\boldsymbol{u}^{n-1}) - \frac{4\boldsymbol{u}^n - \boldsymbol{u}^{n-1}}{2\delta t} + \frac{d\boldsymbol{\Omega}^{n+1}}{dt} \times \boldsymbol{r} \quad \text{(B.33)}$$

with prescribed Dirichlet boundary conditions. Write the above equation in component form $\boldsymbol{u} = (u, v, w)$.

$$asp1^2 * \sum_{t=0}^{M} DX_{i,t}^2 u_{t,j,k}^* + asp2^2 * \sum_{t=0}^{N} DY_{j,t}^2 u_{i,t,k}^* + 2^2 * \sum_{t=0}^{R} DZ_{k,t}^2 u_{i,j,t}^* - \frac{3}{2\delta t} u_{i,j,k}^* = RHSx_{i,j,k} \quad \text{(B.34)}$$

$$asp1^2 * \sum_{t=0}^{M} DX_{i,t}^2 v_{i,t,k}^* + asp2^2 * \sum_{t=0}^{N} DY_{j,t}^2 v_{i,t,k}^* + 2^2 * \sum_{t=0}^{R} DZ_{k,t}^2 v_{i,j,t}^* - \frac{3}{2\delta t} v_{i,j,k}^* = RHSy_{i,j,k} \quad \text{(B.35)}$$

$$asp1^2 * \sum_{t=0}^{M} DX_{i,t}^2 w_{i,t,k}^* + asp2^2 * \sum_{t=0}^{N} DY_{j,t}^2 w_{i,t,k}^* + 2^2 * \sum_{t=0}^{R} DZ_{k,t}^2 w_{i,j,t}^* - \frac{3}{2\delta t} w_{i,j,k}^* = RHSz_{i,j,k} \quad \text{(B.36)}$$

$$\begin{aligned} RHSx_{i,j,k} &= \{\frac{\partial p^*}{\partial x} + 2NL(u^n) - NL(u^{n-1}) \\ &\quad - \frac{4u^n - u^{n-1}}{2\delta t} + z\frac{d\Omega_y^{n+1}}{dt} - y\frac{d\Omega_z^{n+1}}{dt}\}_{i,j,k} \\ &= \{asp1 * DXP^* + 2NLU - NLUold - \frac{4U - Uold}{2\delta t} + z\frac{d\Omega_y^{n+1}}{dt} - y\frac{d\Omega_z^{n+1}}{dt}\}_{i,j,k} \end{aligned} \quad \text{(B.37)}$$

$$RHSy_{i,j,k} = \{\frac{\partial p^*}{\partial y} + 2NL(v^n) - NL(v^{n-1}) - \frac{4v^n - v^{n-1}}{2\delta t} - z\frac{d\Omega_x^{n+1}}{dt} + x\frac{d\Omega_z^{n+1}}{dt}\}_{i,j,k}$$
$$= \{asp2 * DYP^* + 2NLV - NLVold - \frac{4V - Vold}{2\delta t} - z\frac{d\Omega_x^{n+1}}{dt} + x\frac{d\Omega_z^{n+1}}{dt}\}_{i,j,k} \quad \text{(B.38)}$$

$$RHSz_{i,j,k} = \{\frac{\partial p^*}{\partial z} + 2NL(w^n) - NL(w^{n-1}) - \frac{4w^n - w^{n-1}}{2\delta t} + y\frac{d\Omega_x^{n+1}}{dt} - x\frac{d\Omega_y^{n+1}}{dt}\}_{i,j,k}$$
$$= \{2 * DZP^* + 2NLW - NLWold - \frac{4W - Wold}{2\delta t} + y\frac{d\Omega_x^{n+1}}{dt} - x\frac{d\Omega_y^{n+1}}{dt}\}_{i,j,k} \quad \text{(B.39)}$$

In this step we impose the exact boundary values for the velocity components, and then reduce the system as $M-1$ by $N-1$ by $R+1$ linear system.

$$asp1^2 * \sum_{t=1}^{M-1} DX_{i,t}^2 u_{t,j,k}^* + asp2^2 * \sum_{t=1}^{N-1} DY_{j,t}^2 u_{i,t,k}^* + 2^2 * \sum_{t=1}^{R-1} DZ_{k,t}^2 u_{i,j,t}^* - \frac{3}{2\delta t} u_{i,j,k}^* = RHSx_{i,j,k} - asp1^2 * DX_{i,0}^2 U_{0,j,k} - asp1^2 * DX_{i,M}^2 U_{M,j,k} - asp2^2 * DY_{j,0}^2 U_{i,0,k} - asp2^2 * DY_{j,N}^2 U_{i,N,k} - 2^2 * DZ_{k,0}^2 U_{i,j,0} - 2^2 * DZ_{k,R}^2 U_{i,j,R} \quad \text{(B.40)}$$

$$asp1^2 * \sum_{t=1}^{M-1} DX_{i,t}^2 v_{t,j,k}^* + asp2^2 * \sum_{t=1}^{N-1} DY_{j,t}^2 v_{i,t,k}^* + 2^2 * \sum_{t=1}^{R-1} DZ_{k,t}^2 v_{i,j,t}^* - \frac{3}{2\delta t} v_{i,j,k}^* = RHSy_{i,j,k} - asp1^2 * DX_{i,0}^2 V_{0,j,k} - asp1^2 * DX_{i,M}^2 V_{M,j,k} - asp2^2 * DY_{j,0}^2 V_{i,0,k} - asp2^2 * DY_{j,N}^2 V_{i,N,k} - 2^2 * DZ_{k,0}^2 V_{i,j,0} - 2^2 * DZ_{k,R}^2 V_{i,j,R} \quad \text{(B.41)}$$

$$asp1^2 * \sum_{t=1}^{M-1} DX_{i,t}^2 w_{t,j,k}^* + asp2^2 * \sum_{t=1}^{N-1} DY_{j,t}^2 w_{i,t,k}^* + 2^2 * \sum_{t=1}^{R-1} DZ_{k,t}^2 w_{i,j,t}^* - \frac{3}{2\delta t} w_{i,j,k}^* = RHSz_{i,j,k} - asp1^2 * DX_{i,0}^2 W_{0,j,k} - asp1^2 * DX_{i,M}^2 W_{M,j,k} - asp2^2 * DY_{j,0}^2 W_{i,0,k} - asp2^2 * DY_{j,N}^2 W_{i,N,k} - 2^2 * DZ_{k,0}^2 W_{i,j,0} - 2^2 * DZ_{k,R}^2 W_{i,j,R} \quad \text{(B.42)}$$

step 3: correct the preliminary pressure and preliminary velocity through evaluating an intermediate variable ϕ:

$$\frac{3\boldsymbol{u}^{n+1}-3\boldsymbol{u}^{*}}{2\delta t}=-\nabla(p^{n+1}-p^{*}) \tag{B.43}$$

Apply the continuity equation and define the intermediate variable ϕ as $\phi=\frac{2\delta t}{3}(p^{n+1}-p^{*})$, we obtain following equation:

$$\Delta\phi=\nabla\cdot\boldsymbol{u}^{*} \tag{B.44}$$

With pure Neumann boundary condition:

$$\frac{\partial\phi}{\partial n}=0 \tag{B.45}$$

$$\begin{aligned} RHS&=\frac{\partial u^{*}}{\partial x}+frac\partial v^{*}\partial y+\frac{\partial w^{*}}{\partial z}\\ RHS_{i,j,k}&=(asp1*DXU^{*}+asp2*DYV^{*}+2*DZW^{*})_{i,j,k} \end{aligned} \tag{B.46}$$

$$asp1^{2}*\sum_{t=0}^{M}DX_{i,t}^{2}\phi_{t,j,k}+asp2^{2}*\sum_{t=0}^{N}DY_{j,t}^{2}\phi_{i,t,k}+2^{2}*\sum_{t=0}^{R}DZ_{k,t}^{2}\phi_{i,j,t}=RHS_{i,j,k} \tag{B.47}$$

Express the boundary values of ϕ in terms interior points values by the Neumann boundary condition.

$$\begin{aligned} \phi_{0,j,k}&=-\sum_{t=1}^{M-1}\frac{DX_{MM}DX_{0t}-DX_{0M}DX_{Mt}}{DX_{00}DX_{MM}-DX_{M0}DX_{0M}}\phi_{t,j,k}\\ \phi_{M,j,k}&=-\sum_{t=1}^{M-1}\frac{DX_{M0}DX_{0t}-DX_{00}DX_{Mt}}{DX_{M0}DX_{0M}-DX_{00}DX_{MM}}\phi_{t,j,k}\\ \phi_{i,0,k}&=-\sum_{t=1}^{N-1}\frac{DY_{NN}DY_{0t}-DY_{0N}DY_{Nt}}{DY_{00}DY_{NN}-DY_{N0}DY_{0N}}\phi_{i,t,k}\\ \phi_{i,N,k}&=-\sum_{t=1}^{N-1}\frac{DY_{N0}DY_{0t}-DY_{00}DY_{Nt}}{DY_{N0}DY_{0N}-DY_{00}DY_{NN}}\phi_{i,t,k}\\ \phi_{i,j,0}&=-\sum_{t=1}^{R-1}\frac{DZ_{RR}DZ_{0t}-DZ_{0R}DZ_{Rt}}{DZ_{RR}DZ_{00}-DZ_{0R}DZ_{R0}}\phi_{i,j,t}\\ \phi_{i,j,R}&=-\sum_{t=1}^{R-1}\frac{DZ_{R0}DZ_{0t}-DZ_{00}DZ_{Rt}}{DZ_{R0}DZ_{0R}-DZ_{00}DZ_{RR}}\phi_{i,j,t} \end{aligned} \tag{B.48}$$

Plug in the boundary condition into the above equation, we can form the linear system for the ϕ equation.

$$
\begin{aligned}
asp1^2 * \sum_{t=1}^{M-1} DX_{i,t}^2 \phi_{t,j,k} - \\
asp1^2 * DX_{i,0}^2 \sum_{t=1}^{M-1} \frac{DX_{MM}DX_{0t} - DX_{0M}DX_{Mt}}{DX_{MM}DX_{00} - DX_{0M}DX_{M0}} \phi_{t,j,k} - \\
asp1^2 * DX_{i,M}^2 \sum_{t=1}^{M-1} \frac{DX_{M0}DX_{0t} - DX_{00}DX_{Mt}}{DX_{M0}DX_{0M} - DX_{00}DX_{MM}} \phi_{t,j,k} + \\
asp2^2 * \sum_{t=1}^{N-1} DY_{j,t}^2 \phi_{i,t,k} - \\
asp2^2 * DY_{j,0}^2 \sum_{t=1}^{N-1} \frac{DY_{NN}DY_{0t} - DY_{0N}DY_{Nt}}{DY_{NN}DY_{00} - DY_{0N}DY_{N0}} \phi_{i,t,k} - \\
asp2^2 * DY_{j,N}^2 \sum_{t=1}^{N-1} \frac{DY_{N0}DY_{0t} - DY_{00}DY_{Nt}}{DY_{N0}DY_{0N} - DY_{00}DY_{NN}} \phi_{i,t,k} + \\
2^2 * \sum_{t=1}^{R-1} DZ_{k,t}^2 \phi_{i,j,k} - \\
2^2 * DZ_{k,0}^2 \sum_{t=1}^{R-1} \frac{DZ_{RR}DZ_{0t} - DZ_{0R}DZ_{Rt}}{DZ_{RR}DZ_{00} - DZ_{0R}DZ_{R0}} \phi_{i,j,t} - \\
2^2 * DZ_{k,R}^2 \sum_{t=1}^{R-1} \frac{DZ_{R0}DZ_{0t} - DZ_{00}DZ_{Rt}}{DZ_{R0}DZ_{0R} - DZ_{00}DZ_{RR}} \phi_{i,j,t} = RHS_{i,j,k}
\end{aligned}
\tag{B.49}
$$

step 4: finally correct the pressure and velocity field on the entire domain.

$$p^{n+1} = p^* + \frac{3}{2\delta t}\phi \tag{B.50}$$

$$\boldsymbol{u}^{n+1} = \boldsymbol{u}^* - \nabla\phi \tag{B.51}$$

APPENDIX C

NORMAL FORM OF DOUBLE HOPF BIFURCATION POINTS

The Hopf curves intersect each other at double-Hopf bifurcation points. There are two of these: dH_{12} at $(Ri, Re) \approx (2587, 0.214)$ and dH_{23} at $(4925, 0.1245)$. Typically, in the neighborhood of double-Hopf points, quasi-periodic mixed modes of the two limit cycles involved also exist, and in some cases the mixed modes are stable Kuznetsov [38], as is the case here for both double-Hopf bifurcations. Figures C.1 and C.2 describe two generic behaviors of solutions around these points.

At dH_{23}:

- The Hopf curves appear to intersect transversally (i.e. the Jacobian of the flow at dH_{23} is nonsingular) and provide a frame to express the dynamical system around dH_{23}. From Fig. 4.7 the frequencies associated with L_2 and L_3 are in a ratio close to, but not exactly, 2:3.
- The dynamical behavior around dH_{23} is then topologically equivalent to that of the 4-dimensional system Kuznetsov [38, (8.112)]

$$\dot{\xi} = \xi\left(a - \xi - \theta\eta + \mathcal{O}(\eta^2)\right), \quad \dot{\varphi} = \omega_2, \tag{C.1a}$$

$$\dot{\eta} = \eta\left(b - \delta\xi - \eta + \mathcal{O}(\xi^2)\right), \quad \dot{\phi} = \omega_3. \tag{C.1b}$$

The relation between the local coordinates (a, b) and (Ri, Re) is a change of basis, which is estimated from the slopes of the two Hopf curves at dH_{23} in Fig. C.3:

$$\begin{bmatrix} Ri - Ri_{23} \\ Re - Re_{23} \end{bmatrix} \propto \begin{bmatrix} 0.0005 & -0.0005 \\ -4 & 6 \end{bmatrix} \begin{bmatrix} a \\ b \end{bmatrix}, \tag{C.2}$$

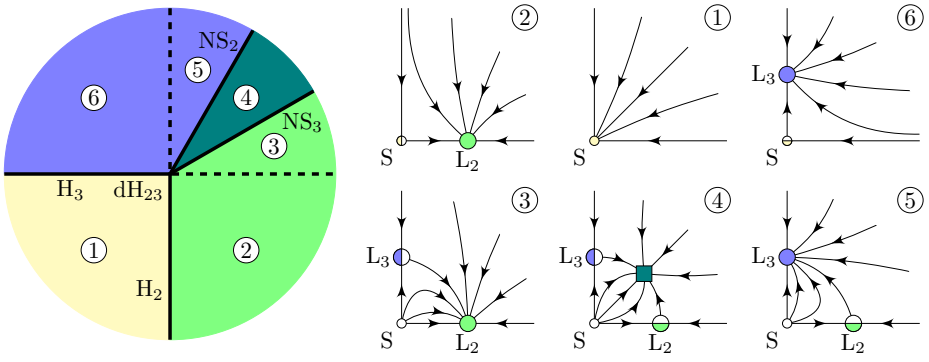

Figure C.1: Left: Generic bifurcation diagram for a nondegenerate simple type II (in the classification of Kuznetsov [38]) double Hopf bifurcation dH. The lines H_i and NS_i are Hopf and Neimark–Sacker bifurcation curves, resp. Right: Normal form phase diagram for each of the six regions. Solid (half-solid, open) circles indicate stable (saddle, unstable) states.

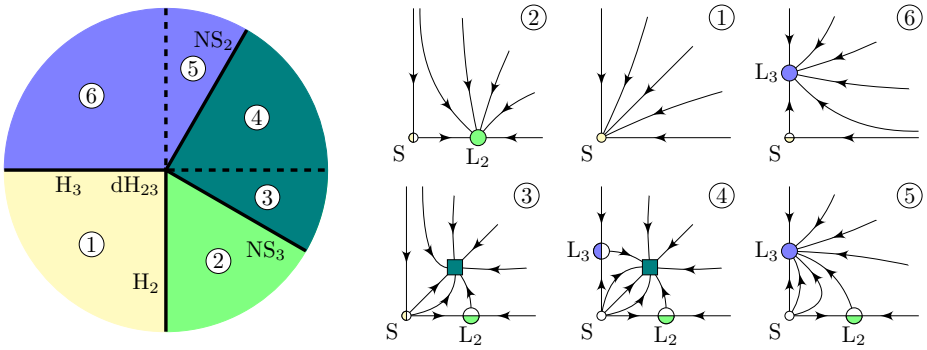

Figure C.2: Same as in Fig. C.1 but for a Nondegenerate Simple Type III Double Hopf Bifurcation. Only Phase Portrait ③ Has Changed Compared to Fig C.1 (Region ⑬ Should Read ⑫ in Kuznetsov [38]).

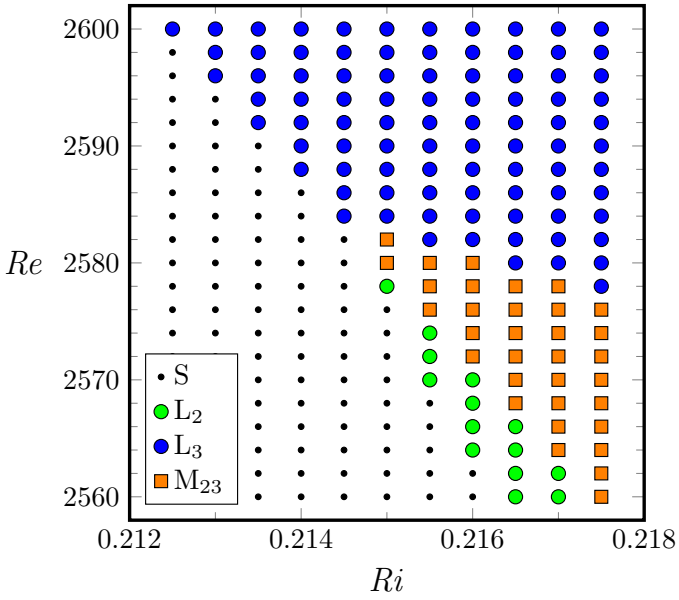

Figure C.3: Stable state observed via continuation of the steady state by increasing Ri at fixed Re in the indicated parameter ranges. The presence of two stable limit cycle solutions and a stable (quasi-periodic) mixed state indicate the presence of two supercritical Hopf branches intersecting at a double Hopf point.

where $\propto$ denotes collinearity and $(Re_{23}, Ri_{23}) = (2587, 0.214)$. The coordinates (a, b) also correspond to the real part of the leading eigenvalues of the Jacobian of the flow at dH_{23} (whose imaginary parts are the Hopf frequencies).

- The parameters θ and δ are estimated from Fig. C.3 by expressing the Neimark–Sacker curves in the frame of the Hopf directions at dH_{23}:

$$\begin{bmatrix} 0.001 \\ -2 \end{bmatrix} \propto \begin{bmatrix} 0.0005 & -0.0005 \\ -4 & 6 \end{bmatrix} \begin{bmatrix} \theta \\ 1 \end{bmatrix}, \quad \begin{bmatrix} 0.0005 \\ -4 \end{bmatrix} \propto \begin{bmatrix} 0.0005 & -0.0005 \\ -4 & 6 \end{bmatrix} \begin{bmatrix} 1 \\ \delta \end{bmatrix}.$$

  This yields $\theta \approx 5/3$ and $\delta \approx 0$. The trivial value of δ corresponds to the alignment of the Hopf and corresponding Neimark–Sacker curves, a degenerate situation in the normal form reduction of dynamical systems Kuznetsov [38, (HH.3) in Th.8.8].

- Whether $\delta = 0$ exactly is unclear from this direct numerical investigation. Confirmation would require a careful eigenvalue analysis of the Jacobian of the flow at dH_{23}.

- If $\delta \neq 0$ (with $|\delta|$ small) we have either $0 < \delta < 1/\theta$ or $\delta < 0 < \theta$, with dynamics corresponding to cases II and III (in the classification of Kuznetsov [38]) illustrated in Figs. C.1 and C.2, resp. The difference between the two situations is how the Hopf frequency ω_2 first appears, either as a pure frequency associated to L_3 (case II), or as part of the quasi-periodic mixed response M_{23} (case III).

- Should $\delta = 0$ hold, dH_{23} would be promoted to co-dimension 3 and a proper determination of the exact topological scenario of the dynamics around dH_{23} would then require variation of another parameter of the problem (e.g., Pr or the aspect ratio of the cavity) to resolve the sign of the $\mathcal{O}(\xi^2)$ term in (C.1b), as was done in Marques *et al.* [63].

A sweep at $Re = 2500$ with increasing Ri yields the following states (obtained from FFT data, see Figure 4.15):

Ri	0.2183	0.2208	0.2233	0.2259	$\cdots$	0.2564	0.2594
state	S	L_2	L_2	M_{23}	$\cdots$	M_{23}	L_3

These transitions are consistent with a nonlinear extension of the Hopf H_3 and Neimark–Sacker curves in Fig. C.3 to lower Re values. Using (C.2) the linear prediction would be $Ri = 0.2213, 0.2249, 0.2357$ for the transitions $S \to L_2$, $L_2 \to M_{23}$, $M_{23} \to L_3$, resp.

At dH_{35}:

- It is difficult to estimate the slope of the Hopf curves H_2 in relation to that of H_3 direct/ly from Fig. C.4, and in particular whether the curves intersect transversally. Figure C.4 suggests they do. Based on the estimation of the Hopf slopes from Fig. C.4 and those of the Neimark–Sacker from Fig. C.4 we obtain the normal form (C.1) with

$$\begin{bmatrix} 0 \\ 2 \end{bmatrix} \propto \begin{bmatrix} 0.1 & -0.1 \\ -2000 & 4000 \end{bmatrix} \begin{bmatrix} \theta \\ 1 \end{bmatrix}, \quad \begin{bmatrix} 0.002 \\ 2 \end{bmatrix} \propto \begin{bmatrix} 0.1 & -0.1 \\ -2000 & 4000 \end{bmatrix} \begin{bmatrix} 1 \\ \delta \end{bmatrix}.$$

  i.e., $\theta \approx 1$ and $\delta \approx 0.51$, which corresponds to the simple case II, Fig. C.1.

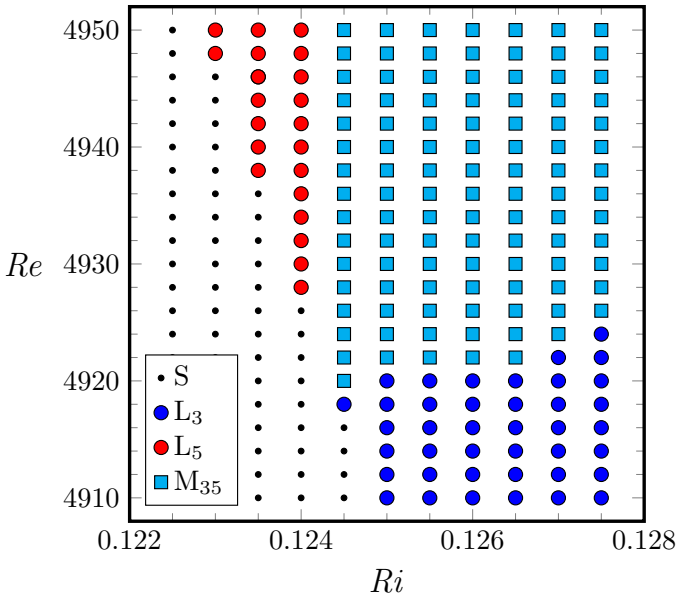

Figure C.4: Same as Fig. C.3 for the Double Hopf Bifurcation Corresponding to the Transition between L_3 and L_5 Around $(4920, 0.1245)$.

- The relation $3\omega_5 = 5\omega_3$ (to numerical accuracy, see Fig. 4.7(b)) does not constitute a degeneracy condition for the standard normal form (C.1) due to the relatively high mode numbers involved ($3+5>5$, see Kuznetsov [38, (HH.0) in Th.8.8]).

APPENDIX D

COMPUTATION OF $\mathcal{K}_Z \times \mathcal{R}_{\pi/2}$-SYMMETRIC INVISCID INERTIAL MODES

In order to keep the notation compact, in this Appendix we shall denote $\mathcal{R}_{\pi/2}$ as $\mathcal{R}$ and use $\dot{}$ for $\partial/\partial t$. The $\mathcal{K}_z$-symmetric inviscid inertial modes are solutions of (5.4) of the form

$$M_n(x,y,z,t) := \begin{bmatrix} u_n(x,y,t) \\ v_n(x,y,t) \\ 0 \\ p_n(x,y,t) \end{bmatrix} \cos(n\pi z) + \begin{bmatrix} 0 \\ 0 \\ w_n(x,y,t) \\ 0 \end{bmatrix} \sin(n\pi z), \tag{D.1}$$

with n even to enforce boundary conditions at $z = \pm 0.5$. Substitution into (5.4) yields

$$\begin{bmatrix} \dot{u}_n \\ \dot{v}_n \end{bmatrix} + 2 \begin{bmatrix} -v_n \\ u_n \end{bmatrix} = -\nabla p_n, \quad \dot{w}_n = n\pi p_n, \quad \nabla \cdot \begin{bmatrix} u_n \\ v_n \end{bmatrix} + n\pi w_n = 0, \tag{D.2}$$

for each value of n. Elimination of p_n and w_n leads to

$$\dot{\boldsymbol{u}}_n + 2\mathcal{R}\boldsymbol{u}_n = \frac{1}{(n\pi)^2} \nabla(\nabla \cdot \dot{\boldsymbol{u}}_n), \quad \boldsymbol{u}_n \cdot \boldsymbol{n}|_{\partial \mathcal{S}} = 0, \quad \boldsymbol{u}_n = \begin{bmatrix} u_n \\ v_n \end{bmatrix}, \tag{D.3}$$

where here $\boldsymbol{n}$ denotes the normal at the edges of the horizontal square cross-section $\mathcal{S}$. $\mathcal{R}_{\pi/2}$-symmetric solutions of (D.3), and thus of (5.4), are obtained as superpositions

$$\boldsymbol{u}_n(x,y,t) = \sum_k p_{k,n}(t) \boldsymbol{v}_k(x,y) + \sum_\ell q_{\ell,n}(t) \mathcal{R}\boldsymbol{v}_{\ell'}(x,y), \tag{D.4}$$

of $\mathcal{R}_{\pi/2}$-symmetric basis functions

$$\boldsymbol{v}_k(x,y) := \begin{bmatrix} \sin(k_1\pi x)\cos(k_2\pi y) \\ \cos(k_2\pi x)\sin(k_1\pi y) \end{bmatrix}, \quad \mathcal{R}\boldsymbol{v}_{\ell'}(x,y) := \begin{bmatrix} -\cos(\ell_1\pi x)\sin(\ell_2\pi y) \\ \sin(\ell_2\pi x)\cos(\ell_1\pi y) \end{bmatrix}, \tag{D.5}$$

where $k = (k_1, k_2)$, $\ell = (\ell_1, \ell_2)$, and $\ell' = (\ell_2, \ell_1)$ are integer pairs. The restrictions $k_1 \neq 0$ even and ℓ_1 odd guarantee that $\boldsymbol{u}_n$ satisfies the boundary condition in (D.3). The orthogonality property

$$(\boldsymbol{v}_k, \mathcal{R}\boldsymbol{v}_{\ell'}) := 2 \int_{-0.5}^{0.5} \int_{-0.5}^{0.5} \boldsymbol{v}_k(x,y) \cdot \mathcal{R}\boldsymbol{v}_{\ell'}(x,y) \, \mathrm{d}x\mathrm{d}y = 0, \tag{D.6}$$

for any k and ℓ, is a direct consequence of the symmetry about $x = y$ of the domain of integration. The functions

$$\begin{aligned} \phi_k &= \nabla \cdot \boldsymbol{v}_k = k_1\pi \left(\cos(k_1\pi x)\cos(k_2\pi y) + \cos(k_2\pi x)\cos(k_1\pi y)\right), \\ \psi_\ell &= \nabla \cdot \mathcal{R}\boldsymbol{v}_{\ell'} = \ell_1\pi \left(\sin(\ell_1\pi x)\sin(\ell_2\pi y) - \sin(\ell_2\pi x)\sin(\ell_1\pi y)\right), \end{aligned} \tag{D.7}$$

correspond to symmetrized versions of the potential and stream functions appearing in Maas [58], with gradients

$$\nabla\phi_k=\pi^2(-k_1^2\boldsymbol{v}_k-k_1k_2\boldsymbol{v}_{k'}),\quad \nabla\psi_\ell=\pi^2(-\ell_1^2\mathcal{R}\boldsymbol{v}_{\ell'}+\ell_1\ell_2\mathcal{R}\boldsymbol{v}_\ell). \tag{D.8}$$

Substitution of (D.4) into (D.3), and using (D.7) and (D.8), yields

$$\begin{aligned}
&\sum_k \dot p_{k,n}\boldsymbol{v}_k+\sum_\ell \dot q_{\ell,n}\mathcal{R}\boldsymbol{v}_{\ell'}+2\sum_k p_{k,n}\mathcal{R}\boldsymbol{v}_k-2\sum_\ell q_{\ell,n}\boldsymbol{v}_{\ell'}\\
&=\frac{1}{(n\pi)^2}\left(\sum_k \dot p_{k,n}\nabla\phi_k+\sum_\ell \dot q_{\ell,n}\nabla\psi_\ell\right)\\
&=-\sum_k \dot p_{k,n}\frac{k_1^2}{n^2}\boldsymbol{v}_k-\sum_k \dot p_{k,n}\frac{k_1k_2}{n^2}\boldsymbol{v}_{k'}-\sum_\ell \dot q_{\ell,n}\frac{\ell_1^2}{n^2}\mathcal{R}\boldsymbol{v}_{\ell'}+\sum_\ell \dot q_{\ell,n}\frac{\ell_1\ell_2}{n^2}\mathcal{R}\boldsymbol{v}_\ell.
\end{aligned}$$

Multiplying by $\boldsymbol{v}_i$ and $\mathcal{R}\boldsymbol{v}_{j'}$, respectively, integrating and using (D.6), implies

$$\begin{aligned}
&\sum_k \dot p_{k,n}(\boldsymbol{v}_i,\boldsymbol{v}_k)-2\sum_\ell q_{\ell,n}(\boldsymbol{v}_i,\boldsymbol{v}_{\ell'})=-\sum_k \dot p_{k,n}\frac{k_1^2}{n^2}(\boldsymbol{v}_i,\boldsymbol{v}_k)-\sum_k \dot p_{k,n}\frac{k_1k_2}{n^2}(\boldsymbol{v}_i,\boldsymbol{v}_{k'}),\\
&\sum_\ell \dot q_{\ell,n}(\boldsymbol{v}_{j'},\boldsymbol{v}_{\ell'})+2\sum_k p_{k,n}(\boldsymbol{v}_{j'},\boldsymbol{v}_k)=-\sum_\ell \dot q_{\ell,n}\frac{\ell_1^2}{n^2}(\boldsymbol{v}_{j'},\boldsymbol{v}_{\ell'})+\sum_\ell \dot q_{\ell,n}\frac{\ell_1\ell_2}{n^2}(\boldsymbol{v}_{j'},\boldsymbol{v}_\ell),
\end{aligned}$$

i.e.,

$$A_n[\dot p_{k,n}]=2B_n[q_{\ell,n}],\quad C_n[\dot q_{\ell,n}]=-2D_n[p_{k,n}],$$

with

$$\begin{aligned}
A_n&=[(A_n)_{i,k}]=\left[\left(1+\frac{k_1^2}{n^2}\right)(\boldsymbol{v}_i,\boldsymbol{v}_k)+\frac{k_1k_2}{n^2}(\boldsymbol{v}_i,\boldsymbol{v}_{k'})\right],\quad B_n=[(B_n)_{i,\ell}]=[(\boldsymbol{v}_i,\boldsymbol{v}_{\ell'})],\\
C_n&=[(C_n)_{j,\ell}]=\left[\left(1+\frac{\ell_1^2}{n^2}\right)(\boldsymbol{v}_{j'},\boldsymbol{v}_{\ell'})-\frac{\ell_1\ell_2}{n^2}(\boldsymbol{v}_{j'},\boldsymbol{v}_\ell)\right],\quad D_n=[(D_n)_{j,k}]=[(\boldsymbol{v}_{j'},\boldsymbol{v}_k)].
\end{aligned} \tag{D.9}$$

The coefficients of these (infinite) matrices can be evaluated from

$$(\boldsymbol{v}_i,\boldsymbol{v}_k)=\left(\operatorname{sinc}\frac{k_1-i_1}{2}-\operatorname{sinc}\frac{k_1+i_1}{2}\right)\left(\operatorname{sinc}\frac{k_2-i_2}{2}+\operatorname{sinc}\frac{k_2+i_2}{2}\right), \tag{D.10}$$

where $\operatorname{sinc}(x)=\sin(\pi x)/(\pi x)$ for $x\neq 0$ and $\operatorname{sinc}(0)=1$. The ansätze

$$[p_{k,n}]=\boldsymbol{p}_n\sin 2\sigma_n t,\quad [q_{\ell,n}]=\boldsymbol{q}_n\cos 2\sigma_n t,$$

yield the generalized eigenvalue problem

$$\sigma_n\begin{bmatrix}A_n & 0\\ 0 & C_n\end{bmatrix}\begin{bmatrix}\boldsymbol{p}_n\\ \boldsymbol{q}_n\end{bmatrix}=\begin{bmatrix}0 & B_n\\ D_n & 0\end{bmatrix}\begin{bmatrix}\boldsymbol{p}_n\\ \boldsymbol{q}_n\end{bmatrix}. \tag{D.11}$$

In the Galerkin approach, the sets of index pairs i and j are the same as the sets of pairs k and ℓ, respectively. For practical computation, these sets are truncated, for each n, to

$$0 \le k_1 + k_2,\, \ell_1 + \ell_2 \le 2N,$$

for some positive integer N chosen to be independent of n. With a consistent ordering of the pairs, the (finite) matrices A_n and C_n are symmetric positive definite, and $B_n^T = D_n$. The restrictions k_2 even and ℓ_2 odd further guarantee that the gradients (D.8) and all terms in (D.3) are $\mathcal{R}_{\pi/2}$-symmetric. The matrices A_n and C_n then have dimension $M = N(N+1)/2$. Upon reordering to keep k and k', and ℓ and ℓ', consecutive, these matrices become block diagonal, with 1×1 or 2×2 blocks. Specifically,

$$\begin{aligned}
&(A_n)_{\{k,k'\},\{k,k'\}} = I_2 + \boldsymbol{k}\boldsymbol{k}^T \quad \text{with} \quad \boldsymbol{k} := \frac{1}{n}\begin{bmatrix} k_1 \\ k_2 \end{bmatrix} \quad \text{if } k_2 \neq 0, k_1, \\
&(A_n)_{k,k} = c_k \left(1 + \boldsymbol{k}^T\boldsymbol{k}\right) \quad \text{with} \quad c_k := \begin{cases} 2 & \text{if } k_2 = 0, \\ 1 & \text{if } k_2 = k_1, \end{cases} \\
&(C_n)_{\{\ell,\ell'\},\{\ell,\ell'\}} = I_2 + \boldsymbol{\ell}\boldsymbol{\ell}^T \quad \text{with} \quad \boldsymbol{\ell} := \frac{1}{n}\begin{bmatrix} \ell_1 \\ -\ell_2 \end{bmatrix} \quad \text{if } \ell_2 \neq \ell_1, \\
&(C_n)_{\ell,\ell} = 1 \quad \text{if} \quad \ell_2 = \ell_1.
\end{aligned} \tag{D.12}$$

On the other hand, the matrices B_n and D_n are full,

$$(B_n)_{k,\ell} = (-1)^{[1+0.5(k_1+k_2+\ell_1+\ell_2)]} \left(\frac{4}{\pi}\right)^2 \frac{k_1\ell_1}{(k_1^2-\ell_2^2)(k_2^2-\ell_1^2)} = (D_n)_{\ell,k}. \tag{D.13}$$

The symmetric positive definite matrices A_n and C_n are trivially diagonalized, and their square roots $A_n^{1/2}$ and $C_n^{1/2}$ are easily computed. The truncated generalized eigenvalue problem (D.11) can then be recast as

$$\sigma_n \begin{bmatrix} A_n^{1/2}\boldsymbol{p}_n \\ C_n^{1/2}\boldsymbol{q}_n \end{bmatrix} = \begin{bmatrix} 0 & S_n \\ S_n^T & 0 \end{bmatrix} \begin{bmatrix} A_n^{1/2}\boldsymbol{p}_n \\ C_n^{1/2}\boldsymbol{q}_n \end{bmatrix} \quad \text{with} \quad S_n = A_n^{-1/2} B_n C_n^{-1/2}, \tag{D.14}$$

i.e., $A_n^{1/2}\boldsymbol{p}_n$ and $C_n^{1/2}\boldsymbol{q}_n$ are the left and right singular vectors of S_n, respectively, associated to each singular value σ_n. These singular values are naturally ordered by decreasing magnitude, and indexed by an integer $1 \le m \le M$. Table D.1 lists the eigenfrequencies (rounded off to 4 significant figures) of the low-order modes $M_{n.m}$ with even $n \le 12$ and $m \le 10$.

Each m determines a pair $(\boldsymbol{p}_n, \boldsymbol{q}_n)$, and a solution $\boldsymbol{u}_n$ of (D.3) using (D.4) and (D.5), with corresponding fields (w_n, p_n) obtained from (D.2), and result in an eigenmode $M_n = M_{n.m}$ in (D.1) indexed by n and m. Note that the meaning of m here differs from the one in the notation $[n, m, +]$ used in Boisson *et al.* [10], where both $\mathcal{R}_{\pi/2}$-symmetric and $\overline{\mathcal{R}}_{\pi/2}$-symmetric were computed, with interlacing frequencies σ_n. Table D.2 summarizes the connection between the two notations for lower values of m.

$M_{2.10}$: 0.2582	$M_{2.9}$: 0.2632	$M_{2.8}$: 0.2782	$M_{2.7}$: 0.2956	$M_{2.6}$: 0.3115
$M_{2.5}$: 0.3392	$M_{2.4}$: 0.3876	$M_{2.3}$: 0.4339	$M_{2.2}$: 0.4644	$M_{4.10}$: 0.4668
$M_{4.9}$: 0.4797	$M_{4.8}$: 0.5086	$M_{4.7}$: 0.5238	$M_{4.6}$: 0.5493	$M_{4.5}$: 0.5918
$M_{6.10}$: 0.6166	$M_{4.4}$: 0.6337	$M_{6.9}$: 0.6351	$M_{6.8}$: 0.6659	$M_{2.1}$: 0.6742
$M_{6.7}$: 0.6789	$M_{4.3}$: 0.6962	$M_{6.6}$: 0.7022	$M_{8.10}$: 0.7200	$M_{4.2}$: 0.7348
$M_{8.9}$: 0.7391	$M_{6.5}$: 0.7424	$M_{8.8}$: 0.7663	$M_{6.4}$: 0.7724	$M_{8.7}$: 0.7777
$M_{10.10}$: 0.7908	$M_{8.6}$: 0.7961	$M_{10.9}$: 0.8082	$M_{6.3}$: 0.8242	$M_{8.5}$: 0.8288
$M_{10.8}$: 0.8306	$M_{12.10}$: 0.8398	$M_{10.7}$: 0.8404	$M_{8.4}$: 0.8499	$M_{10.6}$: 0.8544
$M_{6.2}$: 0.8544	$M_{12.9}$: 0.8548	$M_{12.8}$: 0.8730	$M_{4.1}$: 0.8748	$M_{10.5}$: 0.8801
$M_{12.7}$: 0.8812	$M_{8.3}$: 0.8889	$M_{12.6}$: 0.8920	$M_{10.4}$: 0.8933	$M_{8.2}$: 0.9106
$M_{12.5}$: 0.9122	$M_{12.4}$: 0.9236	$M_{10.3}$: 0.9245	$M_{6.1}$: 0.9376	$M_{10.2}$: 0.9402
$M_{12.3}$: 0.9458	$M_{12.2}$: 0.9575	$M_{8.1}$: 0.9633	$M_{10.1}$: 0.9760	
$M_{12.1}$: 0.9831				

Table D.1: $\mathcal{K}_z \times \mathcal{R}_{\pi/2}$-symmetric inviscid inertial modes, $M_{n.m}$, with even $n \leq 12$, $m \leq 10$, together with their corresponding frequency.

Maas [58], Boisson *et al.* [10]	$[n,1,+]$	$[n,4,+]$	$[n,5,+]$	$[n,7,+]$	$[n,10,+]$	$[n,11,+]$
This work	$M_{n.1}$	$M_{n.2}$	$M_{n.3}$	$M_{n.4}$	$M_{n.5}$	$M_{n.6}$

Table D.2: Correspondence between inviscid inertial eigenmode notations (N large).

Quantities of interest may be computed from (D.1). For example, the vertical component of vorticity, ω_z, of $M_{n.m}$ in the plane $z=0$ can be evaluated as

$$\begin{aligned}\omega_z(x,y,0,t) &= \left(\frac{\partial v_n}{\partial x} - \frac{\partial u_n}{\partial y}\right)(x,y,0,t) \\ &= \left(\sum_k \frac{k_2}{k_1}(\boldsymbol{p}_n)_k \psi_k(x,y)\right)\sin 2\sigma_n t + \left(\sum_\ell \frac{\ell_2}{\ell_1}(\boldsymbol{q}_n)_\ell \phi_\ell(x,y)\right)\cos 2\sigma_n t, \end{aligned} \tag{D.15}$$

with $\boldsymbol{p}_n$ and $\boldsymbol{q}_n$ obtained from the m^{th} singular vectors $A_n^{1/2}\boldsymbol{p}_n$ and $C_n^{1/2}\boldsymbol{q}_n$ in the singular value decomposition (SVD) of S_n. The expression (D.15) can be converted to polar form

$$\omega_z(x,y,0,t) = a_n(x,y)\cos\left(2\sigma_n t - \theta_n(x,y)\right), \tag{D.16}$$

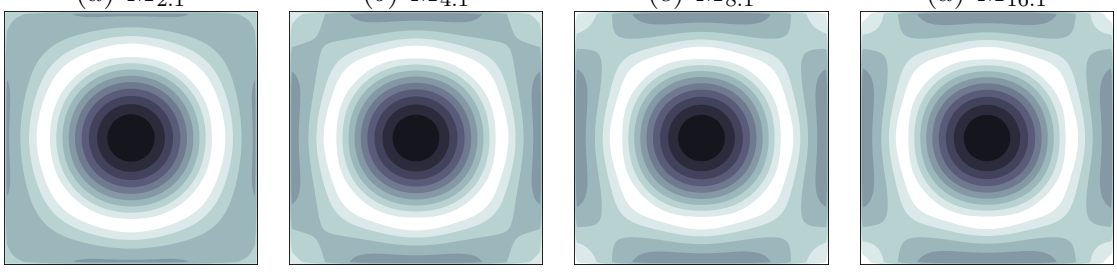

Figure D.1: Normalized amplitude $a_{n.1}(x,y)$ of ω_z of $M_{n.1}$ for n as indicated.

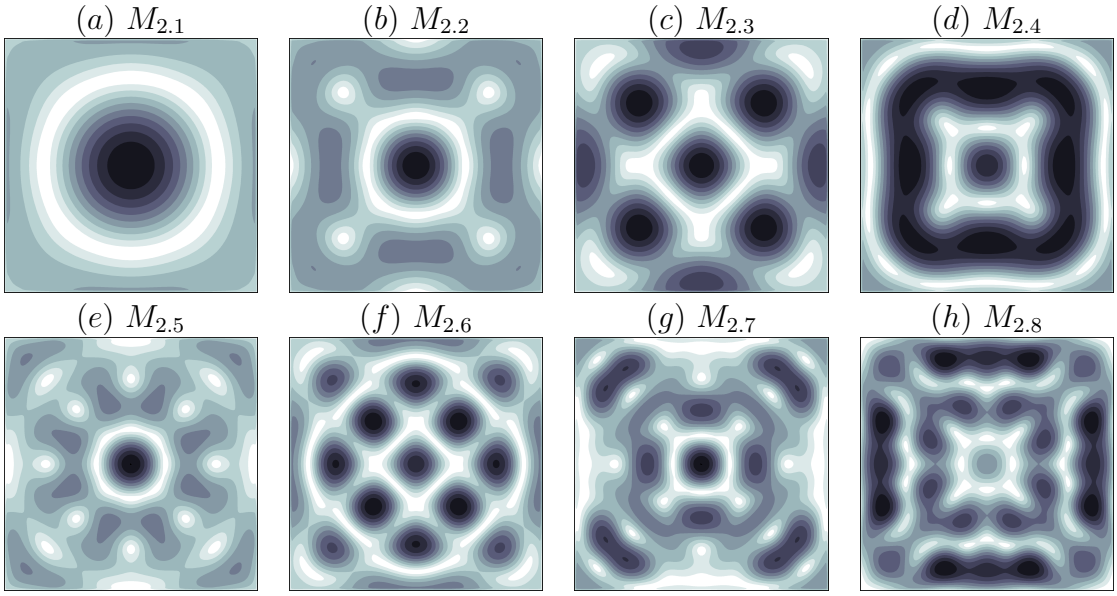

Figure D.2: Normalized amplitude $a_{2.m}(x, y)$ of ω_z of $M_{2.m}$ for m as indicated.

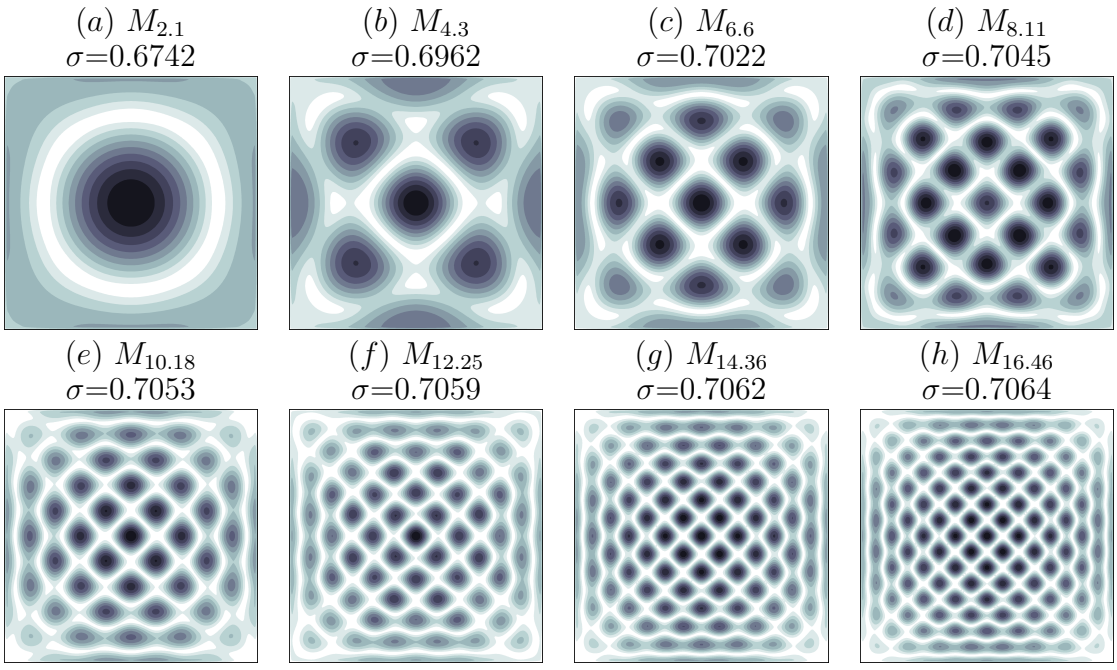

Figure D.3: Normalized amplitude $a_{n.m}(x, y)$ of ω_z of $M_{n.m}$ for m as indicated, with frequencies accumulating at frequency 0.7071 of the retracing ray $R_{1.1}$.

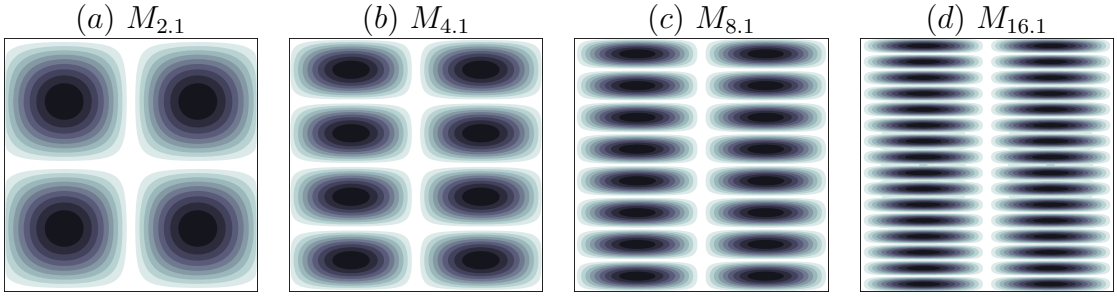

Figure D.4: Normalized amplitude $a_{n.1}(y,z)$ of ω_x of $M_{n.1}$ for n as indicated.

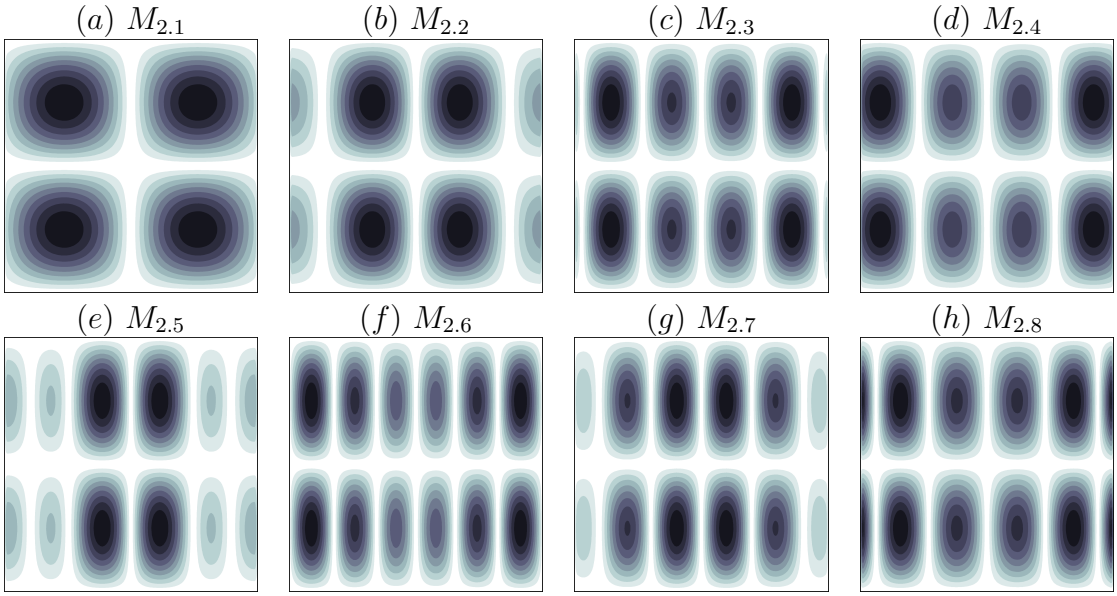

Figure D.5: Normalized amplitude $a_{2.m}(y,z)$ of ω_x of $M_{2.m}$ for m as indicated.

in order to extract the amplitude, $a_n(x,y)$, and phase, $\theta_n(x,y)$. Since

$$\omega_z(x,y,z,t) = \omega_z(x,y,0,t)\cos n\pi z, \tag{D.17}$$

the trace of ω_z in any horizontal plane (constant z) retains its shape as a function of x and y.

The parities of k and ℓ imply $\psi_k = \phi_\ell = 0$, and therefore $a_n = 0$, on the boundaries, for any n and mode m. Certain modes exhibit large amplitude a_n close to the boundary and numerical (Gibbs) oscillations may appear when evaluating a_n on finer grids. These difficulties led Maas [58] to abandon the spectral approach in favor of finite elements [72]. Instead, we evaluate a_n on a uniform $2N \times 2N$ grid, apply two passes

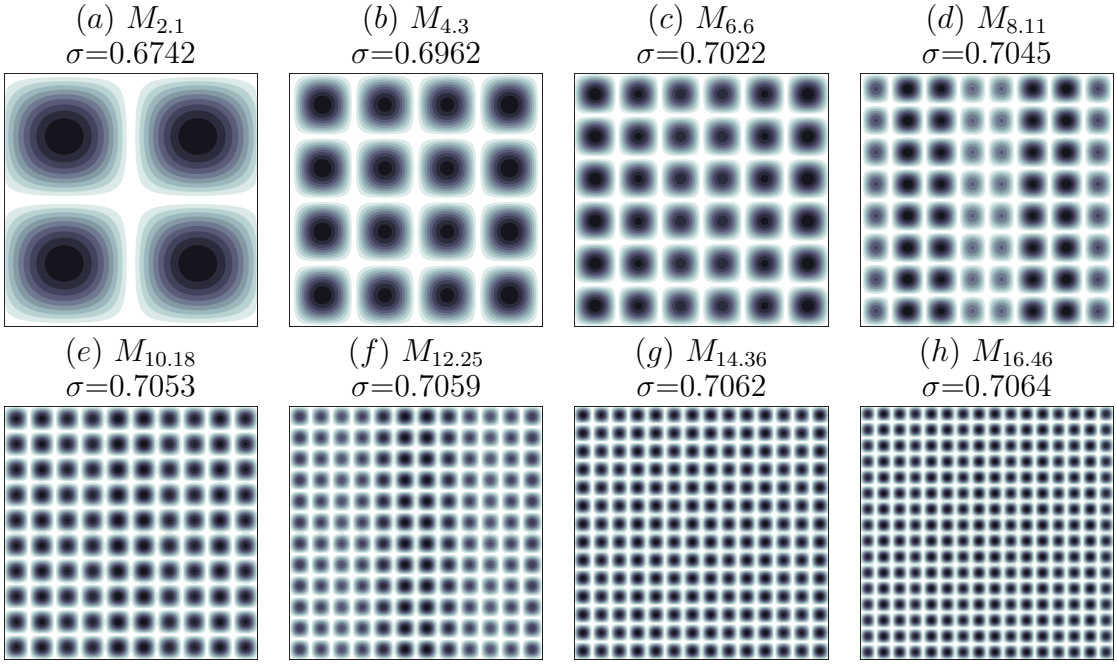

Figure D.6: Normalized amplitude $a_{[n,m]}(y,z)$ of ω_x of $M_{n.m}$ for n and m as indicated, with frequencies accumulating at the frequency 0.7071 of the retracing ray $R_{1.1}$.

of a local low-pass filter with 9-point stencil

$$\frac{1}{(1+2|x|)(1+2|y|)}\begin{bmatrix}|xy| & |y| & |xy|\\ |x| & 1 & |x|\\ |xy| & |y| & |xy|\end{bmatrix}, \tag{D.18}$$

(equivalent to a 25-point stencil in the domain interior), and use a local (spline) interpolation onto a grid mapped from a (possibly finer) uniform grid via the map $f(s)=\sin(\pi s)/2$ (with $s=x,y$) in order to better capture sharp variations of a_n along the edges. The filtering (D.18) is equivalent to standard linear smoothing close to the boundaries, but leaves the solution at the center unchanged.

Similarly, the x-component of the vorticity in the plane $x=0$,

$$\begin{aligned}\omega_x(0,y,z,t) &= \left(\frac{\partial w_n}{\partial y}-\frac{\partial v_n}{\partial z}\right)(0,y,z,t)\\ &= \left[n\pi\sin n\pi z\sum_k(\boldsymbol{p}_n)_k\left(\left[1+\frac{k_1^2}{n^2}\right]\sin k_1\pi y+\frac{k_1k_2}{n^2}\sin k_2\pi y\right)\right]\sin 2\sigma_n t,\end{aligned} \tag{D.19}$$

also vanishes on the domain boundary.

Increasing N increases the size M of S_n and the computational cost of the SVD. Note that to compute mode $m_{\max}$, one only requires the determination of modes $1\le m\le m_{\max}$, and a sparse version of the SVD (e.g. `svds` in MATLAB) provides an

efficient way to determine $\boldsymbol{p}_{n.m}$ and $\boldsymbol{q}_{n.m}$. In fact, the bulk of the computational cost lies in the reconstruction of a mode itself on fine grids.

Convergence to $M_{n.m}$ as N increases happens first for low m values, associated to singular vectors with low spatial variation. In our computations of the eigenmodes, we used $N=100$. The progression of $M_{n.m}$ as n increases with fixed m is illustrated in figure D.1 for $m=1$ (also compare modes $M_{2.6}$ in figure D.2 and $M_{6.6}$ in figure D.3).

Figures D.2 and D.5 illustrate the first 8 modes $M_{2.m}$ associated to $n=2$. Figures D.3 and D.6 show a sequence of similar modes $M_{n.m}$ with increasing n and $m=m(n)$ and frequency $\sigma_{n.m}$ converging to the frequency $1/\sqrt{2}$ of the retracing ray $R_{1.1}$.

The approach described here differs from the Rao–Proudman approach used in Rao [77] and Maas [58] in several ways: (i) the expansion (D.4) automatically enforces the $\mathcal{R}_{\pi/2}$-symmetry of the square horizontal cross-section on the velocity field, while Rao and Maas only enforced $\mathcal{R}_{\pi}$-symmetry in general rectangular cross-sections; (ii) the components (D.5) in the decomposition (D.4) are neither irrotational nor divergence-free, yet still satisfy an orthogonality relation (D.6), in contrast with Rao and Maas's approach based on the Helmholtz decomposition of $\boldsymbol{u}_n$ and subsequent projections onto subspaces of irrotational and divergence-free velocity fields; (iii) only positive frequencies σ_n are computed, via an SVD problem, rather than both positive and negative frequencies obtained directly via a generalized eigenvalue problem similar to (D.11). Failure to explicitly enforce symmetry in (D.11), e.g., using (D.9) with (D.10), was also found to give incorrect results (complex modes) when $N \gtrsim 20$.